Investigations into low pressure methanol synthesis

Sharafutdinov, Irek

Publication date:
2013

Document Version
Publisher's PDF, also known as Version of record

Center for Individual Nanoparticle Functionality

DTU

Investigations into low pressure methanol synthesis

Irek Sharafutdinov

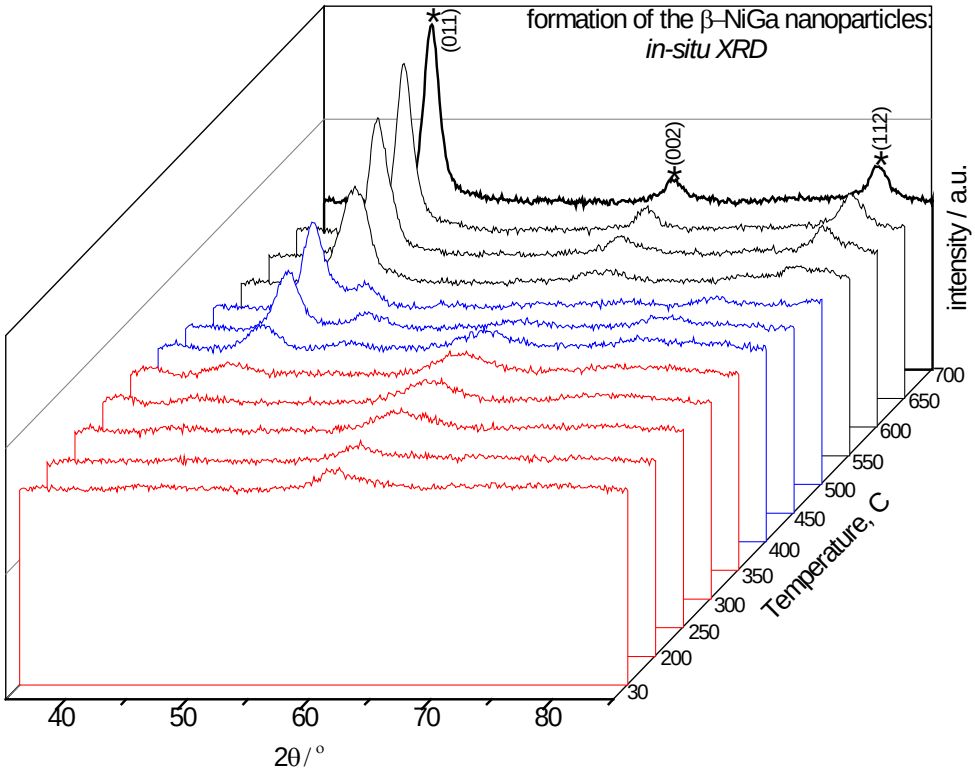

Center for Individual Nanoparticle Functionality

Technical University of Denmark

March 2013

Preface and acknowledgements

This work has been performed in the framework of the CASE (Catalysis for Sustainable Energy) project, at the department of Physics of the Technical University of Denmark, under the supervision of professor Ib Chorkendorff. Now, when my time as a PhD student is coming to an end, I would like to thank all the people who supported me during these years.

Although I find it impossible to express all my gratitude to my parents, I would like to thank them for everything they have been doing for me. You are the two people whom I will never be able to pay back. And of course, special and infinite thanks to my wonderful wife, Alsu: I really appreciate your continuous support and inspiration that you gave me!

Many thanks to my supervisor, Ib Chorkendorff, with whom I had the great pleasure to work with. Although you have not been my main supervisor from the beginning, your valuable advises played a huge role in progression of the work. Thank you for all your help and effort! And I am very grateful to my former supervisor, Søren Dahl, for giving me the opportunity to work at CINF. You were always very supportive and gave me good directions, especially in the beginning of my PhD.

Another two people who played a big role in this project are former Master students (currently PhD students), Christian Elkjær and Diego Gardini. I am extremely happy to have worked with such bright people like you! Your contribution has been very significant.

This project involves utilization of a number of experimental techniques, and it would be practically impossible to cope with all of them alone. I believe I have been extremely lucky being able to use the facilities available at the Center for Electron Microscopy, through collaboration with Christian Damsgård, Linus Duchstein and Jacob Wagner. The experiments at the synchrotrons, which are of the outmost importance for this project, would be impossible without the aid of Gian-Luca Chiarello, Hudson Wallace and Jan-Dierk Grunwaldt.

I would like to thank Helge Rasmussen for technical assistance with XRD apparatus, Dmitry Doronkin, Debasish Chakraborty, Sine Olesen and Anker Jensen for useful discussions at different stages of the project.

Last but not least, many thanks to all of my colleagues. Through communication with you I acquired a great deal of useful knowledge. It is after all you who create an environment which makes CINF such a marvelous place to work!

Irek Sharafutdinov

Kogens Lyngby

Abstract

The central topic of this work has been synthesis, characterization and optimization of novel Ni-Ga based catalysts for hydrogenation of CO_2 to methanol. The overall goal was to search for materials that could be used as a low temperature (and low pressure) methanol synthesis catalyst. This is required for small scale delocalized methanol production sites, where installation of energy demanding compression units should be avoided.

The work was triggered by DFT calculations, which showed that certain bimetallic systems are active towards methanol synthesis from CO_2 and H_2 at ambient pressure. Among them, Ni-Ga has been chosen, primarily due to low price of constituent metals. After the preliminary optimization work, an optimal catalyst composition and preparation method has been suggested. Indeed, for an optimal catalyst, which is a SiO_2 supported Ni-Ga prepared from a solution of nitrates containing 5:3 molar ratio of Ni:Ga, the intrinsic activity (methanol production rate per active surface area) is comparable to that of highly optimised $Cu/ZnO/Al_2O_3$.

Formation of the catalyst was investigated with the aid of in-situ XRD and in-situ XAS techniques. The mechanism of alloying was proposed. It was found that the Ni-Ga nanoparticle formation always proceeds through a more Ni-rich phase. These studies were backed up with the electron microscopy, x-ray fluorescence, thermogravimetric analysis and mass spectroscopy.

The catalyst was found to deactivate both at normal reaction conditions (presumably due to carbon formation) and under accelerated ageing conditions (due to dealloying). However, the initial activity could always be restored after treatment in hydrogen flow at elevated temperatures. The work in the direction of suppression of deactivation and by-product formation is still in progress.

Dansk resume

Det centrale emne i dette projekt har været syntesering, karakterisering og optimering af nye Ni-Ga legeringer katalysatorer til hydrogenering af CO_2 til metanol. Hovedmålet har været at søge efter materialer, der kan anvendes som metanolsyntesekatalysator ved lav temperatur og lavt tryk. Dette er nødvendigt for små lokale metanol produktionssteder, hvor installation af energikrævende kompression enheder er uønsket.

Arbejdet bygger på DFT beregninger, der viste, at nogle legeringer er aktive til metanolsyntese fra CO_2 og H_2 ved atmosfærisk tryk. Blandt disse er Ni-Ga valgt, primært på grund af den lave prise for metallerne. Efter det indledende optimerings arbejde, er en optimal katalysatorsammensætning og fremstillingsmetode blevet foreslået. Den bedste katalysator, som er en Ni-Ga legering på et SiO_2 substrat, har en sammenlignelig aktivitet til de bedste kendte katalysatorer $Cu/ZnO/Al_2O_3$.

Dannelsen af katalysatoren blev undersøgt ved hjælp af in-situ XRD og in-situ XAS teknikker. Mekanismen til formationen af legeringen blev foreslået. Det blev konstateret at dannelsen af Ni-Ga nanopartikel altid forløber igennem en mere Ni-rige fase. Disse undersøgelser blev støttet af afelektronmikroskopi, røntgenstrålefluorescens, termogravimetrisk analyse og massespektroskopi.

Det katalysatoren vidste sig at deaktiverer både under normale reaktionsbetingelser (formodentlig på grund af karbondannelse) og under accelererede ældningsbetingelser (som følge dealloying). Imidlertid kunne den oprindelige aktivitet altid genoprettes efter behandling i hydrogenstrøm ved forhøjede temperaturer. Arbejdet i retning af at undgå deaktivering og biproduktdannelse er stadig i gang.

Contents

1. Introduction

In this chapter I have made an attempt to set the stage for discussing the experimental results that are presented later in this manuscript. This includes a short literature review, brief summary of the preceding theoretical work and basic thermodynamic considerations.

1.1. Background and general overview.

The necessity to enhance the utilization of the so-called “alternative” energy resources is getting more and more obvious these days. One could list numerous reasons to support this statement, among which the next two seem to prevail:

1. The threat of global warming and its consequences. Although some scientists still argue if there is any direct correlation between the level of CO_2 in the atmosphere and climate change or not, many believe that immediate actions should be taken in order to reduce the amount of CO_2 emissions.

2. Predicted depletion of easily available oil and gas resources in the near future and continuously growing prices on fossils.

However, during next few decades the global energy market is predicted to rely on fossil-derived fuels mainly (which today provide nearly 85% of energy consumed worldwide (1). Hence, the more realistic objectives for the nearest future are: enhancing the efficiency of conventional energy sources, and resolving the problem of increasing concentration of carbon dioxide in the atmosphere (by means of for example carbon capture and sequestration).

Generation of methanol could potentially contribute to addressing both of the above mentioned problems. It is widely known that methanol is produced industrially from syngas (a mixture of CO and H_2) with addition of small amounts of CO_2. The syngas, in term, is derived from natural gas or hydrocarbons (2). Meanwhile, it has been estimated that in 1998, some 3,8 trillion cubic meters of the so-called “stranded” gas (which is in principle a very valuable mixture of light hydrocarbons) has been vented to the atmosphere or burned near the wellheads. If it was processed under appropriate conditions, about 78 million tons of methanol could be derived, which is twice as much as the amount of methanol produced in 2009 worldwide (3)**.** Further, methanol can be converted to dimethyl ether (DME) which is considered as a feasible fuel for diesel engines, or into higher hydrocarbons according to a well established methanol-to-olefins (MTO) process (4). Taking into account that methanol is a good fuel itself, and an important intermediate for chemical industry (its downstream products include coatings, adhesives, dyestuff, pharmaceuticals, etc), the efficient utilization of “stranded” gas would result in more sustainable industry. And this is only one example.

On the other hand, CO_2 itself can be used as a feedstock for methanol production, again helping to address both problems simultaneously (actually carbon dioxide has a potential to being utilized as a starting material for production of great variety of chemicals and fuels, which are summarized in (5). Catalytic hydrogenation of CO_2 is believed to be potentially one of the most promising countermeasures against global warming (6). In this line, it has been shown (7) that hydrogenation of carbon dioxide on copper surface leads to methanol production. Therefore, converting CO_2 to methanol could be in principle considered as a separate process, as proposed in (8). But before going into details, one should have a look at the history of industrial methanol and related catalysis.

The first synthetic methanol production technology has been developed and implemented in 1923 by BASF, a German company that earlier pioneered in launching an ammonia synthesis process from nitrogen. Synthesis gas derived from German coal, and hence heavily contaminated by chlorine and sulfur (9), was used as a feedstock. A catalyst, based on zinc oxide on chromia (ZnO/Cr_2O_3) was found to be relatively resistant to poisoning, but possessed low activity. To overcome poor activity while maintaining reasonable equilibrium conversion to methanol, the process had to be carried out at very high pressures (250-350 bar) and elevated temperatures (up to 450°C) (2), (9). Although the operating conditions suggest high investment costs, the technology remained dominant for several decades.

It should be mentioned that catalytic activity of Cu/ZnO towards methanol synthesis has been first reported in 1925 (10). But the process could not be commercialized due to poor lifetime of catalyst. Nevertheless, as syngas produced via steam reforming of natural gas and hydrocarbons started to prevail in the market, a new generation of processes were developed. In the 1960`s, Imperial Chemical Industries (ICI) finally succeeded to develop a “low pressure” process (35-55 bar, 200-300°C) based on copper/zinc oxide catalyst, which is the only industrial-scale process for methanol production nowadays. Since 1960`s, numerous research groups have been investing a great deal of effort to continuously improve the performance of the copper-based catalyst. The main areas for investigations have been: improving and fine tuning the preparation procedure, enhancing performance by incorporating promoters, prolonging catalysts lifetime, etc.

Unfortunately, the information on what has been done by chemical engineering companies is very scarce, obviously due to confidentiality reasons. Hence, it is quite difficult to make any comparison from the point of view of industrial catalyst preparation technology. According to (11), there are four catalyst suppliers and six companies offering complete proprietary processes for methanol synthesis, namely: Uhde, Lurgi, ICI, Haldor Topsoe, Mitsubishi and M.W. Kellogg.

As mentioned above, a lot has been done since mid 60`s to enhance the characteristics of low-pressure catalysts, and that the selectivity of modern industrial catalysts is usually higher than 99,9% (9). In order to comply with such high requirements, catalysts should possess:

1. Good hydrogen activation ability

2. Ability to activate C-O bond of CO/CO_2 molecule without breaking it (to avoid undesirable methanation process)
3. Less than 15 kcal/mol activation energy for the rate-limiting step to ensure reasonable reaction rate at 250°C
4. Stability against reduction and sintering under reaction conditions
5. Reasonably low stability of intermediate metal methoxide to avoid surface poisoning.
6. Absence of active alumina, iron, nickel and alkali metals all resulting in side reactions and/or decreased activity (12).

Although the activity and selectivity of commercial catalyst is reasonably high, a lot of effort is still being put to enhance its performance. Here (in table 1.1) I have made a humble attempt to classify the catalysts according to the type of support, active metal and promoter:

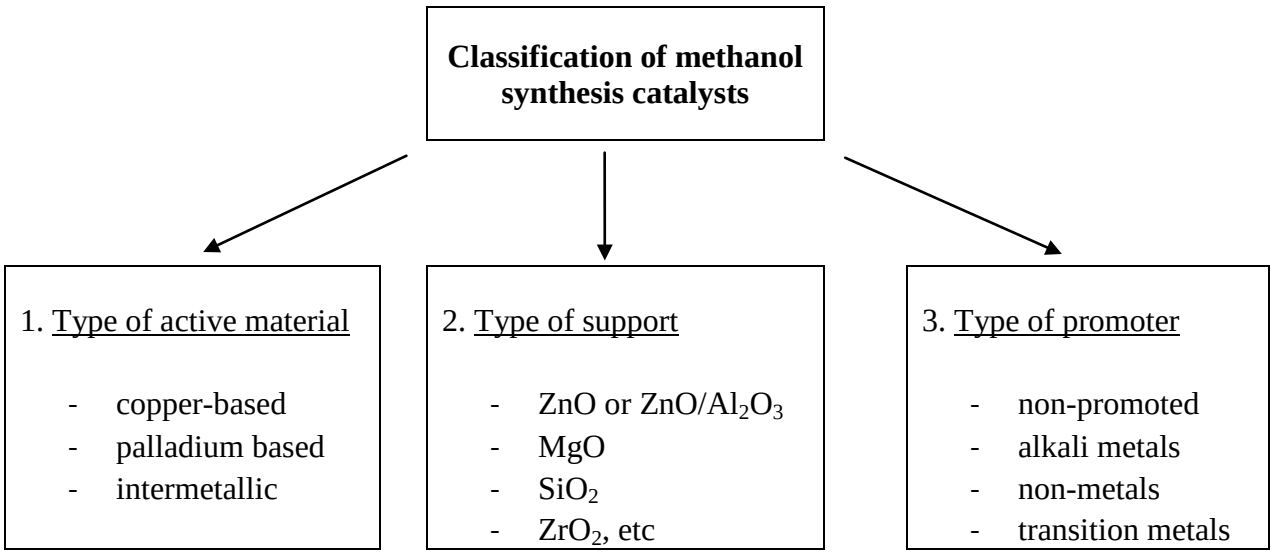

Table 1.1. (Arbitrary) classification of methanol synthesis catalysts.

1.2. Intermetallic compounds for methanol synthesis.

Since the main focus of my research has been on investigations into catalysts based on bimetallic compounds, further I will only discuss alloy/intermetallic catalysts for methanol synthesis. As it has been pointed out in (13), there is a difference between using intermetallics *in catalysis* and *as*

catalysts. In the former case, the intermetallic phase could serve as a catalyst precursor, without being directly involved into the catalytic process.

Remark. In the literature there seems to be no consensus on whether the term "alloy" or "intermetallic" should be used, when it concerns bimetallic catalysts. One can even encounter a term "*intermetallic alloy*" in the title of an article (see for example "Methanol synthesis catalysts derived from ternary rare earth, copper, zirconium and rare earth, copper, titanium intermetallic alloys" by Lambert R.M and Nix R.M. (14)). The definition of the two terms is given in (15): "*… we understand hereafter an intermetallic compound as a chemical compound of two or more metallic elements adopting an – at least partly – ordered crystal structure that differs from those of the constituent metals … on the other hand, an alloy is – usually multiphase – mixture of elements or their solid solutions and intermetallic compounds*". Since the Ni-Ga systems studied in this work fall into the definition of "intermetallic" compound, the latter terms will be used when discussing the Ni-Ga catalysts. However, in the literature review section, both terms – "alloy" and "intermetallic" – are utilized, depending on the preference of the authors of the original article.

The terms "alloying" and "dealloying" are used to describe the processes leading to formation and disintegration of the intermetallic phases, respectively.

1.2.1. Intermetallics *in catalysis*.

In late 70`s a group of researchers from New South Wales succeeded to perform methanol synthesis on a new type of copper-based catalyst, which was produced by leaching of Cu-Zn-Al alloy with sodium hydroxide solution. Since Al and Zn are soluble in NaOH, the resulting product was essentially a high surface area copper with small amounts of Zn and Al (16). Since then the different aspects of raney-type catalysts have been investigated: the influence of initial alloy composition, leaching conditions (basically temperature and pH), extent of leaching, etc. Again, some of the results suggest that under certain conditions raney copper derived catalysts exhibit better characteristics than commercially utilized ones.

The approximate composition of the most frequently used alloys corresponds to: Cu/Al/Zn = 2/2/1 (16), (17). In (17), a catalyst prepared from an alloy consisting of 43 wt.% copper, 39 wt.% aluminum and 18 wt.% zinc was compared to the commercial catalyst: the two showed almost the same activity per unit copper area.

Some studies suggest (2) that underleached alloys exhibit better characteristics than their fully leached counterparts. The composition range of such catalyst is quite wide: 75-90% of copper; 4-8% aluminum; 5.7-15% zinc.

Moreover, the later work (18) resulted in even higher activity of raney catalyst towards methanol, which was explained by improved pore structure. Alloy derived copper was found to possess a superior network of macro- and mesopores compared to conventional pelleted catalyst, thus having improved mass transfer characteristics. Nevertheless, water to methanol ratio

obtained for raney catalyst appeared to be greater, which is disadvantageous for industrial-scale processes since separation costs are increased

1.2.2. Intermetallics *as catalysts*.

Alloys of copper with some transition and rare earth metals, which do not require to be leached, are making an alternative class of catalytic systems that might be used for methanol synthesis. In literature, catalysts derived from Cu/Ce or Cu/Th alloys are most frequently mentioned. For intermetallic catalysts, proper activation conditions in terms of feed gas composition are apparently crucial for catalysts performance.

Thus in (19), a series of copper-lanthanide alloys have been studied, and the highest methanol yield was obtained for Cu_2Ce at the temperature as low as 100°C and 50 bar. Nevertheless, the presence of even small amount of CO_2 in the feed deactivated the catalyst irreversibly, which suggests that the mechanism for methanol synthesis is different compared to conventional catalysts. Moreover, even for CO_2-free syngas these compounds exhibit significant loss of activity over time. Attempts were made to overcome poor stability by means of incorporating a third component. Ternary alloys of copper, cerium and one of the following elements: Al, Cr, Mn, Pd, Zn, were tested for MS reaction using a mixture of CO and H_2 (20). The best performance was observed for aluminum containing alloys, which despite of being less active than binary systems, proved to be more stable. The proposed role of aluminum was stabilization of highly dispersed Cu/Ce phase.

The addition of third component, namely rare-earth metal, into the Cu/Zr and Cu/Ti alloys is discussed in (14). The performance of catalysts was studied over a wide range of temperatures and pressures: 12 to 50 bar and up to 250°C using CO/H_2 feed. The activity of Cu/Zr containing 2% of Yttrium at certain conditions enhanced the activity of initial alloy twice.

Quite interesting results are presented in (21), where certain Cu/Th alloys are claimed to possess the activity towards methanol which is 6-7 times higher than for industrial $Cu/ZnO/Al_2O_3$. In general, the results of research work in the field of intermetallic compounds suggest that potentially methanol could be produced at lower temperatures with higher yield. However, comparatively low selectivity, stability, and manufacturing issues need to be addressed before these systems are considered for industrial-scale processes.

1.3. Rational approach to catalyst design: utilization of computational tools.

The classification given in the table 1.1 is certainly not comprehensive, since the optimization of the $Cu/ZnO/Al_2O_3$ catalyst has been the center of attention of numerous research groups both in academia and industry for a few decades, which created a huge variety of catalytic systems. This, on the other hand, has set up very high standards in terms of performance and cost if alternative

catalysts should be utilized for this process. The only major drawback of the copper based catalysts is sintering, that is responsible for partial but irreversible deactivation (22).

Therefore, it would be inefficient to use a common "trial-and-error" approach in an attempt to find a better catalyst for this process. Instead, reliable computational tools need to be developed and employed if the number of time consuming and costly experimental screening procedures should be minimized. Catalyst development from first principles is playing an increasing role nowadays. In particular, density functional theory (DFT) calculations are widely utilized to pick out potential candidates. For example, with the aid of DFT it has been explained why nickel is a good catalyst for CO methanation; moreover, Ni-Fe alloy was predicted and experimentally confirmed to be a good candidate for catalyzing this reaction (23). Another example is in ammonia synthesis, where the use of iron and ruthenium based catalysts has been theoretically rationalized (24).

In order to assess the "goodness" of a potential catalyst candidate, one needs to estimate the kinetics of different reaction pathways leading to both desired and unwanted products. This provides insights into activity and selectivity. To achieve the goal, a complete reaction pathway that takes into account all intermediates and transition states should be calculated for every particular catalyst candidate. On top of this, the energy pathway depends on which surface sites are considered: flat surfaces, steps, kinks, various vacancies all have different interaction energies with reaction intermediates. However, this approach is very demanding in terms of computational power, as a realistic reaction pathway is described by tens to hundreds of elementary steps. Thus it is necessary to reduce the number of these "descriptors" in order to assess large numbers of various candidates in a reasonable time. For the carbon monoxide methanation reaction mentioned above, such descriptors are the adsorption energies of atomic carbon (ΔE^C) and atomic oxygen (ΔE^C) on metal (or alloy) surface. Apparently, for a variety of d-metals the values of ΔE^C and ΔE^O scale linearly with the adsorption energies of intermediate CH_x species and transition state energy for CO dissociation, respectively (25). Hence, the turnover numbers can be estimated based on the values of ΔE^C and ΔE^O and thus potential catalyst can be depicted. The concept of linear relations was shown to hold for a number of reactions, examples of which are summarized in (26) .

This concept has also been applied for pinpointing new catalysts for methanol synthesis prior to starting this work. However, computational work was performed within a different project, and therefore will not be addressed here in detail. Instead, only a simplified algorithm is given to show how the calculations were done. A more detailed description can be found in (27).

a) A reaction scheme for CO_2 hydrogenation, which consists of 8 steps, is proposed.

b) Activation energies are calculated for each of the reaction step, assuming that fcc(211) stepped sites are active, thus mapping out a reaction energy diagram.

c) Scaling relations between the oxygen absorption energy (ΔE_o) and the elementary reaction energies are established. This enables to calculate the reaction energies using only one parameter.

d) A microkinetic model for CO_2 hydrogenation is solved using only one parameter (ΔE_o) as an input. In this way, a large number of potentially active surfaces are screened in a short time

The resulting volcano plot where turnover frequency is calculated as a function of oxygen binding energy is shown in figure 1.1. One can notice that various surface geometries possess different activities for CO_2 hydrogenation to methanol: for instance the step site with Ni atom on top is 2-3 orders of magnitude more active than the step sites with gallium on top. However, it is an experiment that would examine the validity of the calculations.

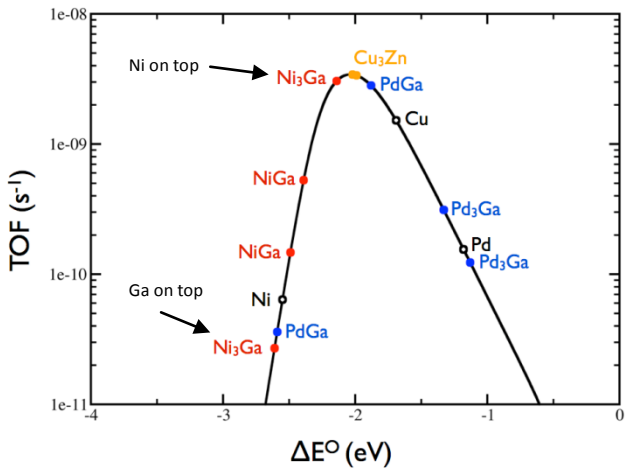

Figure 1.1. Turnover frequency values for CO_2 hydrogenation to methanol calculated as a function of oxygen binding energy. Reaction conditions are 500 K, 1 bar, CO_2:H_2 ratio 1:3 (27)

1.4. Why “low temperature - low pressure”?

An overwhelming majority of studies in the field of methanol synthesis are dedicated to optimizing processes that require relatively high pressures (50-100 bars). This pressure interval is relevant for industrial applications, but such processes involve large scale production units, high operational and investment costs.

The ultimate goal of the CASE (Catalysis for Sustainable Energy) project is to develop small scale CO_2 neutral fuel production processes, in particular involving the conversion of hydrogen to more easily transportable fuels, such as alcohols. Hydrogen, in turn, should be generated by electrolytic splitting of water using the electricity from solar cells or wind mills, i.e. a process involving renewable energy resources. Wind mills are particularly interesting for Denmark, as

this would offer an attractive way to store wind energy. If methanol has to be produced in decentralized units, a feasible "low temperature – low pressure" process needs to be developed to avoid large scale units operations.

The low T process is also beneficial from thermodynamic point of view: methanol production is an exothermal reaction, both in case of CO_2 and CO hydrogenation (equations 1.1 and 1.2). This implies that low temperatures should in principle favour formation of the alcohol. On the other hand, high pressure shifts the equilibrium to the right due to entropy considerations. Using HSC-6 program, software for performing thermodynamic calculations, the equilibrium CO and CO_2 conversions at 4 different pressures for a wide range of temperatures were calculated (figure 1.2). Reactions enthalpies given below were calculated using standard thermodynamic data (28)

$$CO_2 + 3H_2 \leftrightarrow CH_3OH + H_2O, \quad \text{dH = -57.3 kJ/mol} \quad (1.1)$$

$$CO + 2H_2 \leftrightarrow CH_3OH, \quad \text{dH = -96.7 kJ/mol} \quad (1.2)$$

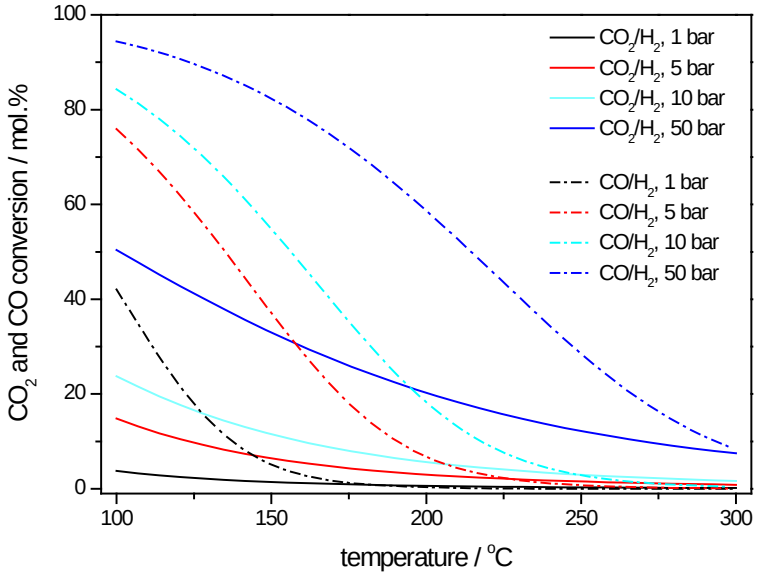

Figure 1.2. Calculated values of equilibrium CO and CO_2 conversion from CO/H_2 and CO_2/H_2 mixtures during methanol synthesis.

It is clear from the figure that low temperatures and elevated pressures should favor formation of the desired product. For a constant temperature, the equilibrium methanol production is improved: however, it is also apparent that hydrogenation of CO should be preferred as this gives better results. But CO_2, on the other hand, is a cheaper and safer option especially when it comes to small scale facilities. It would be very much desirable to have a methanol synthesis catalyst working below 200°C in order to make it feasible at lower pressures. But due to kinetic limitations, the optimal temperature window for the $Cu/ZnO/Al_2O_3$ catalyst is 250-300°C. Development of a catalyst active at lower temperatures is the primary subject of this work.

2. Before experiments were started: setting the stage

Catalytic experiments are often quite lengthy and require that process parameters such as temperature, pressure, feed composition, etc are changed during the test. Moreover, the data from various sources needs to be synchronized and stored in a way easy to treat. In the present case, the following steps had to be taken before experiments were started: buildup and testing of equipment, automation of the process with the aid of Labview software, establishing a data collection routine, setting up a standard method for the gas chromatography measurements, performing benchmarking experiments using $Cu/ZnO/Al_2O_3$ catalyst. Finally, the validity of preliminary data was verified using thermodynamic calculations. In the following sections, I will describe these steps in more detail.

2.1. Catalyst testing setup and data processing methodology

The schematic diagram of the setup are presented in figure 2.1. The heart of the setup is a reactor made of quartz glass with a catalyst bed placed in the isothermal part of the oven, where T_{max}-$T_{min} \leq 1.5$C. Two thermocouples are located on both ends of the bed to ensure that the temperature gradient across reaction zone is minimized. The gas flows are controlled by means of digital mass flow controllers, calibrated with a manual bubble flow meter. Five MFCs are integrated into the setup: H_2, CO, CO_2, CO_2 low flow, and Ar. The later one is also used to feed 1% O_2/Ar or 0.4 % H_2/Ar mixture whenever required. The pressure is measured at the upstream side of the system, and controlled by a manual back pressure regulator mounted at the outlet of the reactor. The reaction mixture, normally 100Nml/min of CO_2/H_2, is separated into two streams by means of needle valves, ensuring a constant flow of 25Nml/min of gas through the GC. This is needed to maintain a constant pressure in the GC sampling loop, to be consistent with the amount of gas injected with each sample.

The analog readout data from MFCs, thermocouples and pressure transducer are continuously displayed, processed, and collected by a home-made Labview program. A graphical representation of the interface is shown in figure 2.2. The program is also responsible for reading a pre-made text file that contains temperature and mass flow setpoints as a function of time.

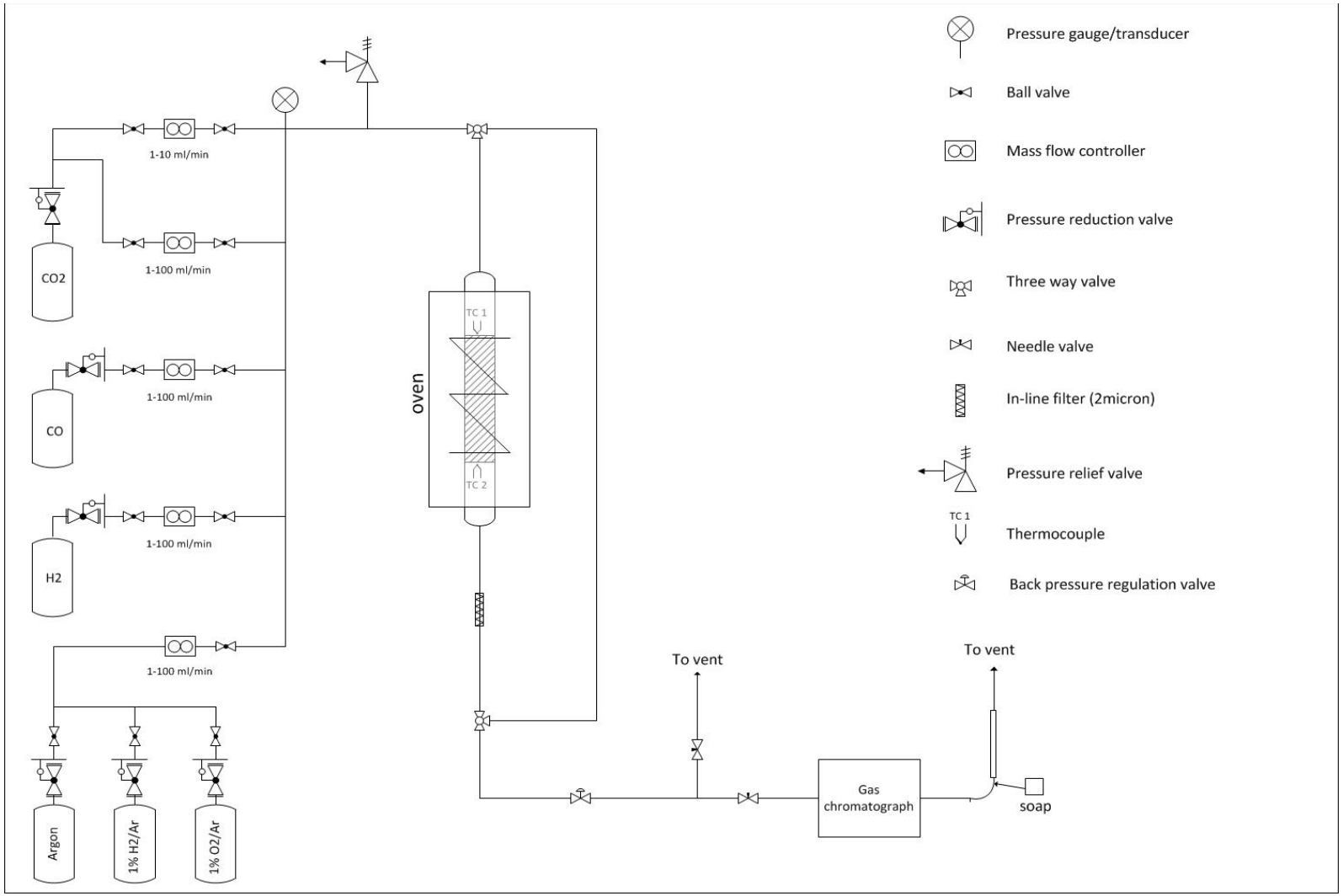

Figure 2.1. Schematic diagram of the methanol synthesis setup.

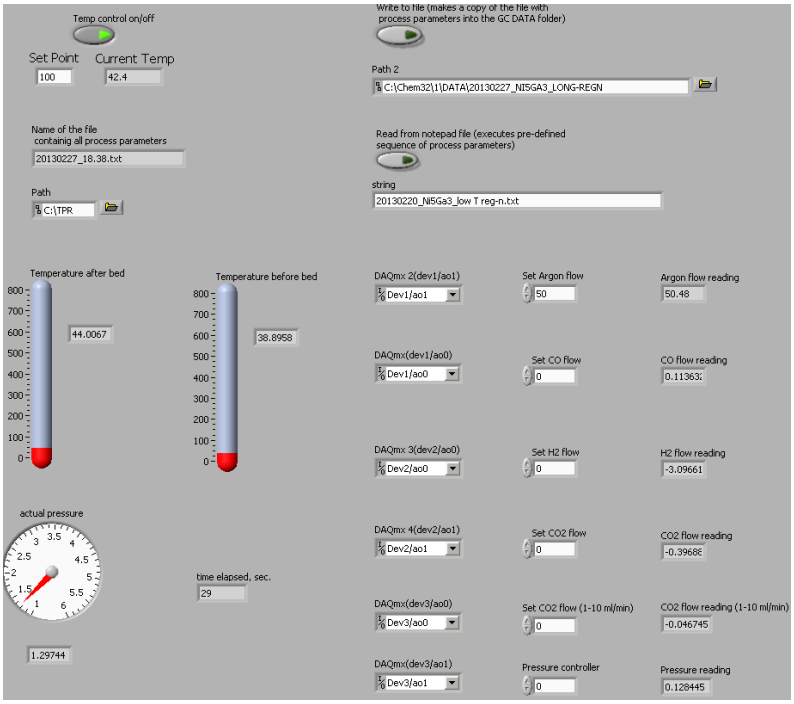

Figure 2.2. A front page of the labview-based process control program

2.2. Gas chromatography: basic principles and operation

The main analytical tool utilized throughout the entire duration of my project has been a Gas Chromatograph (GC). This instrument is very convenient in the sense that both qualitative and quantitative analysis of complex mixtures can be continuously performed in a relatively fast and easy way. The heart of the GC is a separation column (usually packed or capillary, depending on applications), which is placed in an oven to ensure fine temperature control. The inner diameter of the capillary column is coated with a microscopic layer of a so-called stationary phase. The sample of interest that is initially injected into the sample loop is flushed by a gas (helium or nitrogen), and carried into the column. As the sample enters the column, its components interact with the stationary phase by means of multiple adsorption/desorption cycles, determined by the physical properties of each individual compound. Consequently, the rate of these cycles will be unique for every compound at a given temperature, pressure and flowrate, as will be the time required for a particular component to be eluted. This value is called a retention time; it enables qualitative analysis.

The effluent of the column is further analyzed by a detector, typically a TCD (thermal conductivity detector) or FID (flame ionization detector). The former one relies on measuring the

thermal conductivity of a substance by a filament, usually made of tungsten or ruthenium, and comparing this value with that of the reference gas. The area of the observed chromatographic peak is proportional to the difference in thermal conductivities and the concentration of the component in the analyzed mixture. This is a universal method that is in principle applicable to all compounds, but the use of TCD is often limited due to low sensitivity. In contrast, FID is much more sensitive, but its applications are confined to combustible substances. FID relies on burning the analyzed component in a hydrogen/air mixture, which results in formation of CHO^+ ions detected as a current (29). This ensures very high sensitivity and accuracy of measurements. In practice, a combination of the two detectors is often necessary, which is also the case in the present work.

The main advantages of the GC before other online analytical tools are versatility and a high quality of quantification. For example, a mass spectrometer has a much better time resolution but is hardly applicable when a mixture of hydrocarbons or other homologous compounds are present. Moreover, quantification is more cumbersome as the ion current corresponding to a particular molecular fragment might be dependent on the composition of reaction mixture. Fourier transform infrared spectrometer (FTIR) captures some of the advantages of both GC and MS: reliable quantification and excellent time resolution, respectively, but the method is only applicable for the analysis of polar compounds. GC and MS would be a very nice combination for this work, as this would draw a better picture of dynamical changes in the system during the process. However, a separate setup connected to a mass spectrometer was used to carry out certain experiments when required.

The configuration of the GC (Agilent 7890A) was designed based on feed and expected reaction mixture compositions, namely: H_2, CO_2, CO, Ar, CH_3OH, $(CH_3)_2O$, CH_4 and higher hydrocarbons. Three columns in series are used in the TCD line: *80/100 HATESEP Q* packed column is responsible for moisture removal, *19095P-QO4* capillary column for separation of CO_2, and *19095P-MS6* molecular sieve column is dedicated to separation of H_2, argon and CO. Organic products are separated with the aid of *19091J-413* capillary column in the FID line. A gas sample is withdrawn every 15 minutes and 5-7 measurements are taken at each temperature and for every gas composition to ensure stable reading. The schematics of the GC layout is presented in figure 2.3.

The calibration of gaseous components, H_2, CO_2, CO, Ar and C_1-C_3 hydrocarbons, was straightforward, since their mass flows were finely controlled. Methanol was calibrated by bubbling a constant flow of argon through a vessel containing the alcohol. The vessel was kept in a melting ice bath at 0^oC, implying that the vapor pressure of methanol was constant. The argon-methanol flow was gradually diluted by a known amount CO_2, which resulted in a calibration line. DME was not subjected to direct calibrations: effective carbon number concept was used instead (30) . This approach enables to calculate the response of an FID detector to various organic compounds, when they are not available.

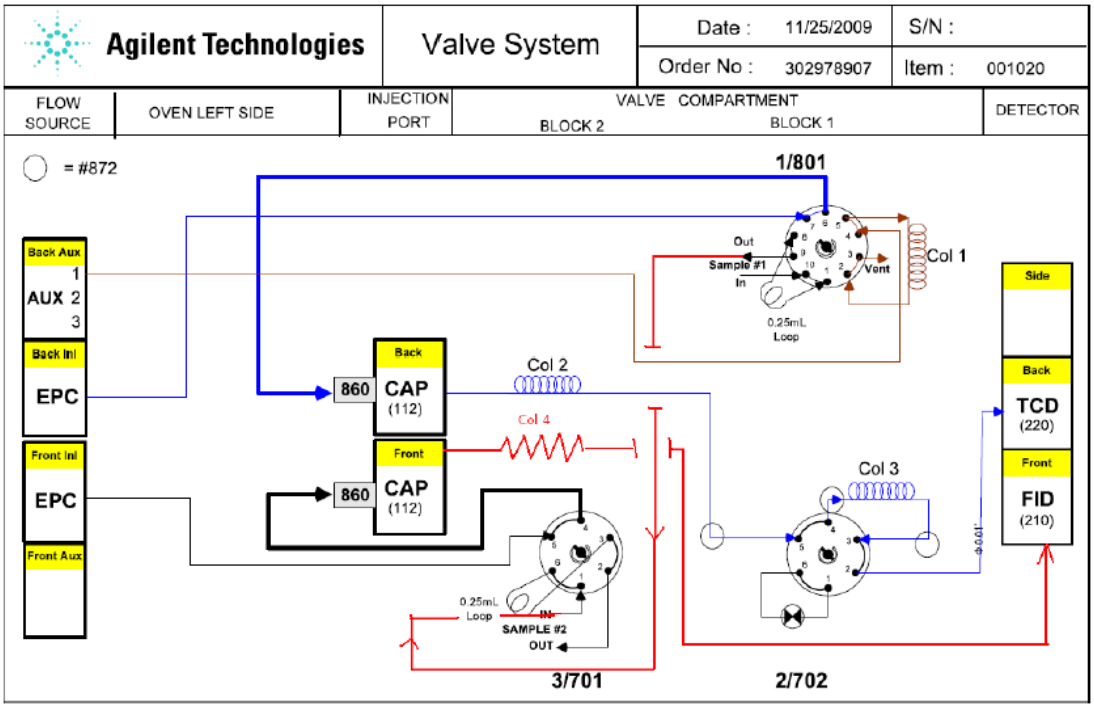

Figure 2.3. Schematics of the GC flow system design.

The frequency of sampling, which determines the time resolution of the experiment, is limited by the retention time of the slowest component in the analyte. In order to minimize the sampling time, the temperature of the GC oven can be increased. However, this might compromise the quality of separation, which is usually inversely proportional to the temperature. In the present case, the problem was partially circumvented by changing the temperature during the separation process, but still only one sample per 15 minutes could be withdrawn due to very slow rate of carbon monoxide elution. This method has been used throughout the project.

When a labview program capable of handling the flow system was made and a GC method optimized for running the methanol synthesis experiments was established, a Matlab script taking care of synchronizing in time the process parameters with the GC data was written. The script is responsible for compiling all the data into a separate EXCEL sheet in an easily processible format. The concentrations of product gas components are calculated according to the following equation:

$$Ci = \frac{Ai/Fi}{\sum_i Ai/Fi} \qquad (2.1)$$

Here A_i is the peak area, and F_i is the calibration factor for the i^{th} component. For quantification, it is important to always check the mass balance, i.e. $\sum A_i/F_i = 1$. The product selectivity is defined as:

$$\varphi = \frac{Ni \times Ci}{\sum_i Ni \times Ci} \times 100\% \qquad (2.2)$$

where N_i is the number of carbon atoms in the molecular structure of i^{th} component. This way of expressing the selectivity is convenient as it shows how efficiently a carbon source is converted into a desired carbon containing molecule. With this, everything was ready to start an experiment.

2.3. Cu/ZnO/Al_2O_3: benchmarking experiment and thermodynamic analysis

Since Cu/ZnO/Al_2O_3 is widely accepted to be the best methanol synthesis catalysts and known to produce methanol in sufficient amount at atmospheric pressure, it was prepared and tested to see if the equipment was working properly and the data processing routine was giving adequate results. The details of the testing and preparation procedures are given in chapters 4.1 and 5.1.1; here only some of the data is presented in the light of thermodynamic analysis.

Methanol and carbon monoxide production during CO_2 hydrogenation is presented in figure 2.4: the yield of CH_3OH at atmospheric pressure is increased for T < 205C, and diminishes at higher temperatures. This suggests that methanol production is limited by the approach to equilibrium at T > 205C. To verify this, calculations have been performed, according to the procedure described below.

CO_2 is hydrogenated to methanol according to the following reaction:

$$CO_2 + 3H_2 \leftrightarrow CH_3OH + H_2O \qquad (2.3)$$

Carbon monoxide is the only detectable by-product, formed in a reverse water gas shift reaction:

$$CO_2 + H_2 \leftrightarrow CO + H_2O \qquad (2.4)$$

However, other reactions leading to formation of water should be also considered, for instance methanation or DME formation:

$$CO_2 + 4H_2 \leftrightarrow CH_4 + 2H_2O \qquad (2.5)$$

$$2CH_3OH \leftrightarrow (CH_3)O(CH_3) + H_2O \qquad (2.6)$$

The equilibrium constant for the reaction 2.3 can be written as:

$$Kp = \frac{P(CH3OH) \times P(H2O)}{P(CO2) \times (P(H2))^3} \qquad (2.7)$$

Where p_i is the partial pressure of the i-th component. The GC columns utilized in this work are not capable of detecting water. However, equations 2.3 - 2.6 imply that *P(H2O) = (P(CH3OH) + P(CO) + 2P(CH4) + P(DME))*. With this, eq. 2.7 can be re-written as:

$$Kp = \frac{P(CH3OH) \times (P(CH3OH + P(CO) + 2 \times P(CH4) + P(DME))}{P(CO2) \times (P(H2))^3} \quad (2.8)$$

On the other hand, the equilibrium constant can be calculated using Van`t Hoff equation:

$$\Delta G = -RT \times ln(Kp) \quad (2.9)$$

Gibbs free energy change for the reaction as a function of temperature is calculated using the values collected on table 2.1 (28).

Compound	ΔH_f^{298K} [kJ/mol]	S_f^{298K} [J/mol*mol]
CO_2 (g)	-393.6	239.9
CO (g)	-110.0	212.8
H_2 (g)	0	145.7
H_2O (g)	-243.8	206.5
$(CH_3)_2O$ (g) Dimethyl ether	-184.1	266.4
CH_3OH (g)	-207.8	266.3
CH_4 (g)	-80.5	207.2

Table 2.1. Standard thermodynamic data on the typical components of the product gas

Here an assumption was made that the enthalpy and entropy values are constant in the temperature range of interest. Combining equations 2.8 and 2.9, replacing $P(CH3OH + P(CO) + 2 \times P(CH4) + P(DME)$ = $\boldsymbol{b}$ and $P(CO2) \times (P(H2))^3$ = $\boldsymbol{c}$, and solving the equation for methanol partial pressure, the following analytical expression is derived (full mathematical derivation is skipped):

$$P(CH3OH) = \frac{-b + \sqrt{b^2 + 4c \times e^{-\frac{\Delta H - T \times \Delta S}{RT}}}}{2} \quad (2.10)$$

which allows to estimate the equilibrium methanol yield as a function of temperature at a given rate of reverse water gas shift reaction. It should be noted that the changes in the concentrations of the reactants, CO_2 and H_2, are neglected, since the overall conversion is very little. Also, it is assumed that fugacity coefficient is unity, i.e. the fugacities of all components equal to their partial pressures. The equilibrium partial pressure of methanol is thus calculated using the read-out values of temperature, pressure and reaction mixture composition. Finally, equilibrium partial pressures are converted to concentrations and plotted together with experimental data, as shown in figure 2.4.

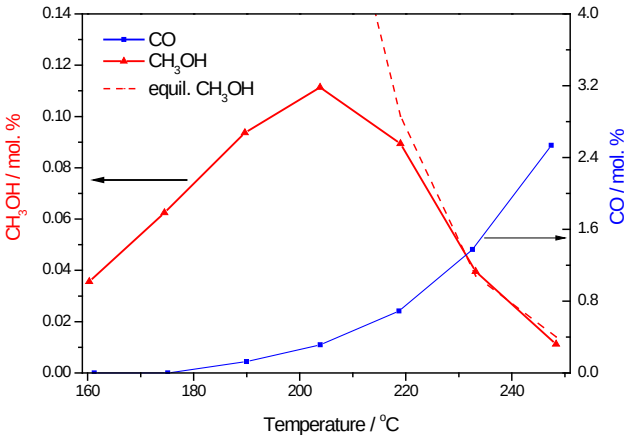

Figure 2.4. A typical methanol synthesis experiment on $Cu/ZnO/Al_2O_3$ catalyst at atmospheric pressure. Gas composition: 25 % CO_2 and 75% H_2, flowrate = 100 ml/min.

At T > 220°C, the observed and equilibrium methanol production curves converge, meaning that the method gives adequate experimental results, i.e both GC and temperature calibrations are correct. The maximum production rate being 15-20°C below the equilibrium is a well known phenomenon; when reaction approaches equilibrium, the rate decreases exponentially. If several experiments with different conversion levels were performed and the data points corresponding to maximum production were connected, a so-called “optimal operation line” would be obtained. It would run in parallel to the equilibrium line, and look very similar for example to that of NH_3 synthesis (31). With this it was concluded that a newly built setup could be used to produce new exciting results.

3. Theoretical background

In the present research project, various in-situ and ex-situ characterization techniques were used. This chapter is aimed to highlight the basics of these methods, as well as to rationalize why they were utilized.

3.1. X-Ray Diffraction.

The overview of the XRD and XRF methods is mainly based on the contents of the book by Leif Gerward, a professor at DTU Physics (32), chapters 5-8. XRD has been the main characterization method in this work, as it offers a fast and reliable "first check" of the catalyst. Both in-situ and ex-situ XRD measurement have proven to be a powerful tool in revealing catalysts properties, such as average crystalline size, crystallographic phase, dynamical changes of the catalysts structure during preparation, and to some extent in quantifying the phase composition. In the following, the principles behind such analysis will be briefly discussed.

The fundamental phenomenon behind X-ray diffraction analysis is Rayleigh scattering, a process of interaction between the incoming electromagnetic radiation and the valence electrons of an atom. In this process the x-rays are elastically scattered by these electrons, implying that if there exists a long range periodicity in the atomic arrangement (crystallinity), a regular array of the scattered x-ray waves will be produced. In some directions, these waves interfere and reinforce each other; the later phenomenon can be detected as a diffraction peak. The simplified illustration of such interaction is shown in figure 3.1:

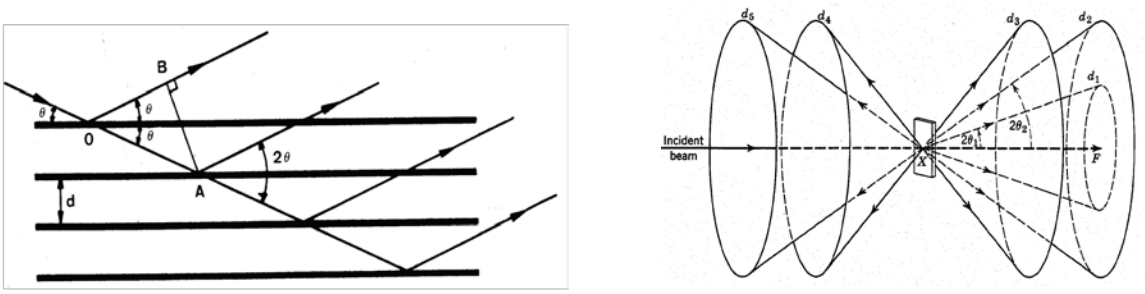

Figure 3.1. A simplified illustration of the phenomena behind Bragg-Brentano (left) and Debye-Schearer (right) type diffractomers. (32).

Conditions for constructive interference of the outgoing electromagnetic waves are given by Braggs law:

$$n\,\lambda = 2d \times sin\theta \qquad (3.1)$$

which is derived using simple geometrical considerations. Here, d is the distance between certain crystallographic planes, θ and λ are the angle of incidence and the wavelength of the incoming x-ray radiation. For a single crystal, the *d* value is constant; this means that only at certain (and unique) incident angle the Bragg diffraction conditions are fulfilled, unless the sample is rotated to expose all possible crystal planes. In the case of powder diffraction, it is assumed that very large number of randomly oriented crystallites is present in a sample. Thus, for every possible [*hkl*] orientation, there will always be a fraction of crystallites whose [*hkl*] planes are exposed in a way that will result in constructive interference of the x-rays at a certain angle θ.

The choice of the geometry of the detection system is usually made between Bragg-Brentano and Debye-Scherrer camera. The laboratory scale diffractometer was equipped with the former one, while the later was encountered at the synchrotron facilities (SNBL, Grenoble, France). The idea behind Bragg-Brentano geometry (figure 3.1, left) is to place the sample in the middle of an imaginary circle on a horizontal plane, while moving the x-ray tube and detector simultaneously over a range of angles. In contrast, the geometry of Debye-Scherrer camera enables to capture all scattered x-rays forming diffraction spots or diffraction rings (figure 3.1, right). When a polycrystalline sample is illuminated by the x-rays, they will be reflected by all sets of [*hkl*] planes and reinforce each other in angels defined by Bragg conditions. As a result, diffraction rings are formed on a photographic film or a CCD camera. In both cases, the resulting intensity can be plotted as a function 2θ. The width of the diffraction peak is used to estimate the average size of the crystals in the direction perpendicular to the reflecting plane: according to Scherrer law (equation 3.2), the peak broadening is inversely proportional to the crystallite size. Diffraction from linear grating is known to produce peak broadening which is proportional to λ/N, where N is the number of grating elements. Similarly, if a crystal is viewed as a grating, then it is obvious why smaller crystallites produce broader peaks. This is particularly useful in catalysis because the size of catalytically active crystallites is usually in the range of several nanometers.

$$\tau = \frac{K \times \lambda}{\beta \times sin\theta} \qquad (3.2)$$

λ is the wavelength, θ is the Bragg angle, τ – nanoparticle size and β – full width at half maximum (FWHM) of the analyzed diffraction peak .

Together with the more conventional ex-situ measurements, in-situ XRD facilities were heavily employed in this work. The corresponding equipment can in principle be viewed as a normal fixed-bed setup, where a flat surface of a catalyst bed is illuminated by X-rays. The gases are pre-mixed and forced through the catalyst, while the product stream is analyzed by a mass spectroscopy. However, in this design the normally preferred plug-flow conditions are compromised (the possible consequences of this difference will be discussed later).

When the quality of diffraction data is high enough (this is achieved either at the synchrotron light source facilities or by large exposure times, i.e. good counting statistics), Rietveld method can be employed to both qualitatively and quantitatively determine which crystallite phases are present in the sample. This is particularly relevant for analysis of intermetallics, to estimate the "phase purity" of targeted compound or relative abundance of coexisting phases. Rietveld method, however, is not a structure solution method, since it requires that a reasonable "first guess" is made on what crystallographic phases are present in a sample. The refinement parameters such as: background coefficients, structural parameters, profile parameters (peak shapes) are varied in a least-squares procedure until a good agreement between calculated and observed diffractograms is obtained.

3.2. X-Ray Fluorescence

However, apart from elastic scattering other processes might take place when x-rays interact with atoms: the energy of the incoming radiation could be used to excite an electron from atomic core levels. Upon relaxation of the excited atoms, photons with characteristic energy are produced in a process called fluorescence. In practice, the XRD machines are often equipped with a filter to remove these photons from the diffracted beam side. But this phenomenon can also be utilized for qualitative and quantitative analysis at dedicated x-ray fluorescence (XRF) machines, which has proven to be an easy and very efficient way to check the composition of the Ni-Ga compounds in the present work.

3.3. X-Ray Absorption

Another method based on interaction of an analyzed material with x-ray radiation, which has provided extremely useful insights into the structure of the studied catalysts, is X-Ray Absorption. This method relies on the ability of an atom to strongly absorb the incoming electromagnetic radiation, provided that the energy of the later is close to the so called *absorption edge* – an energy required to excite core level electrons of an atom under bombardment. In other words, the absorption coefficient of an atom is deviating strongly from Beer–Lambert law (equation 3.3.) close to the absorption edge (here $\underline{\alpha}$ is absorption coefficient, $\underline{l}$ is the thickness of material that photons have to travel through, I and I_0 are the intensities of transmitted and irradiated light). Depending on the energetic level of an excited electrons (1s, 2s/2p, 3s/3p/3d, etc.), the edge is called *K, L, M*, etc. Since the binding energy of these electrons is unique for every element, the position of the absorption edge can be in principle used to identify the chemical composition of a material. In practice, the elemental composition is usually known *a priori*, and the method is mainly used to extract the information about the local

environment in the close vicinity of the absorber atom, its coordination number, oxidation state, etc, as will be discussed below. Analysis of the absorption around K-edge is the most popular choice, because it provides the most pronounced “edge jump”.

$$log\frac{I_0}{I} = \alpha \times l \qquad (3.3)$$

In simple terms, a typical XAS experiment can be described as follows: a sample is irradiated with a flux of photons with a very narrow energy distribution. The starting energy of the electromagnetic flux is typically a few hundreds eV below the absorption edge of an atom under investigation; the energy is then gradually increased (by changing the position of the monochromator) to a value which is roughly 1000 eV above the edge. The intensity of transmitted photons is measured by a detector. In this way, variations of the value of absorption coefficient as a function of energy is tracked, as presented in figure 3.2a (a XAS spectrum obtained at the Ni K-edge of an as-prepared Ni_5Ga_3/SiO_2 catalyst). The absorption spectrum can be divided into 3 main regions: pre-edge, where the absorption coefficient is linearly decreasing with energy; Near Edge X-ray Absorption Fine Structure (NEXAFS), which captures the “edge jump”, and the Extended X-ray Absorption Fine Structure (EXAFS), which reflects the variations in the absorption coefficient above the edge. The later oscillations are of particular interest as they contain information about the local chemical environment around the absorber. This, after proper mathematical treatment (the details of which are beyond the scope of the present work) enables to derive values of interatomic distances, coordination number, types of neighboring atoms, etc. The nature of these oscillations stems from multiple scattering of the electrons, emitted as a result of absorption of the photons (figure 3.2b) (33). These electros can be treated as waves, which reinforce or destroy each other, thus creating an EXAFS footprint. The magnitude of the edge jump can be used to assess the oxidation state of an element: the more oxidized is an atom - the more intense is the jump.

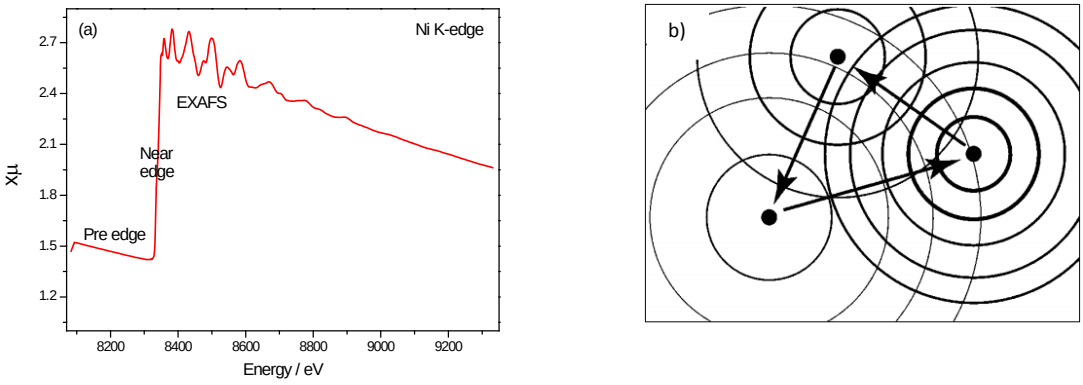

Figure 3.2. (a) A XAS spectrum of an as-prepared Ni_5Ga_3/SiO_2 catalyst and (b) simplified illustration of a multiple scattering event (33).

The utilization of XAS method provides very useful complimentary information to XRD data. The later technique gives information on the long-range order of the crystalline phases, while the former method provides insight into the local surrounding of the absorber. Combining the two techniques is particularly advantageous when both crystalline and amorphous phases are present in a sample. This has been shown by (34), where dynamical structural changes of supported Pd catalysts have been studied. In this work, however, the XRD and XAS data were obtained separately. The exception is the accelerated ageing experiment conducted in SNBL beamline, Grenoble, as discussed in chapter 6.1.2.

3.4. Transmission Electron Microscopy (TEM)

The final method that will be discussed in this section, TEM, unlike X-ray methods, enables direct visualization of the catalysts in a nanometer (and even in sub-nanometer) scale. Various properties of supported nanoparticles, such as average particle size, dispersion and shape are convenient to investigate with the aid of TEM. Moreover, most of the modern commercial electron microscopes, including the one used in this work, are equipped with additional tools such as EDS (energy dispersive spectroscopy) and EELS (electron energy loss spectroscopy). In TEM, recording diffraction patterns is also possible, and hence the crystal structure can be revealed thanks to electron diffraction. This means that a modern electron microscope has absorbed some of the advantages of dedicated X-ray methods.

This overview of the TEM method is based on the book by D. B. Williams and C. B. Carters (35). The basic principle of the method, as can be judged from the title, relies on transmission of highly accelerated electrons (usually 120-400 KeV) through an analyzed material. Due to wave-like properties, electrons behave similar to light and thus some analogies with conventional visual light microscopes (VLM) can be pointed out. In the VLM, light is focused by means of an optical lens system, and a magnified image is projected on the ocular. In an electron microscope, electrons are used instead of photons, electromagnetic instead of optical lens system is employed in order to guide the electron beam down the microscopes optical axis, and a magnified image is formed on the fluorescent screen (or a CCD camera) instead of the ocular. Although VLMs are more simple and cheap, they utilize photons of the visible light spectra (300-700nm) as a probe and thus have a limited resolution, given by a Rayleigh criterion:

$$\delta = \frac{0.61 \times \lambda}{\mu \times sin\beta} \qquad (3.4)$$

Here λ is wavelength, μ is a refractive index of the medium and β is semi-angle of collection of a magnifying lens. When $\mu \times sin\beta$ is unity, then 500nm photons give approx. 300nm resolution, which is close to the fundamental limit to all VLMs. Since electrons can be accelerated to very

high energies and thus very short wavelengths, their resolving power is much better (down to sub-angstrom dimensions).

The investigated material is usually supported on a sample holder, and the analyzed area is preferably below 100nm thick to ensure that a good portion of electrons is transmitted. This limitation is dictated by a *mean free path* consideration, which is in the order of a nanometer for medium energy electrons (such as those used for example in X-ray photoelectron spectroscopy) but increases to a few tens of nm for highly accelerated electrons.

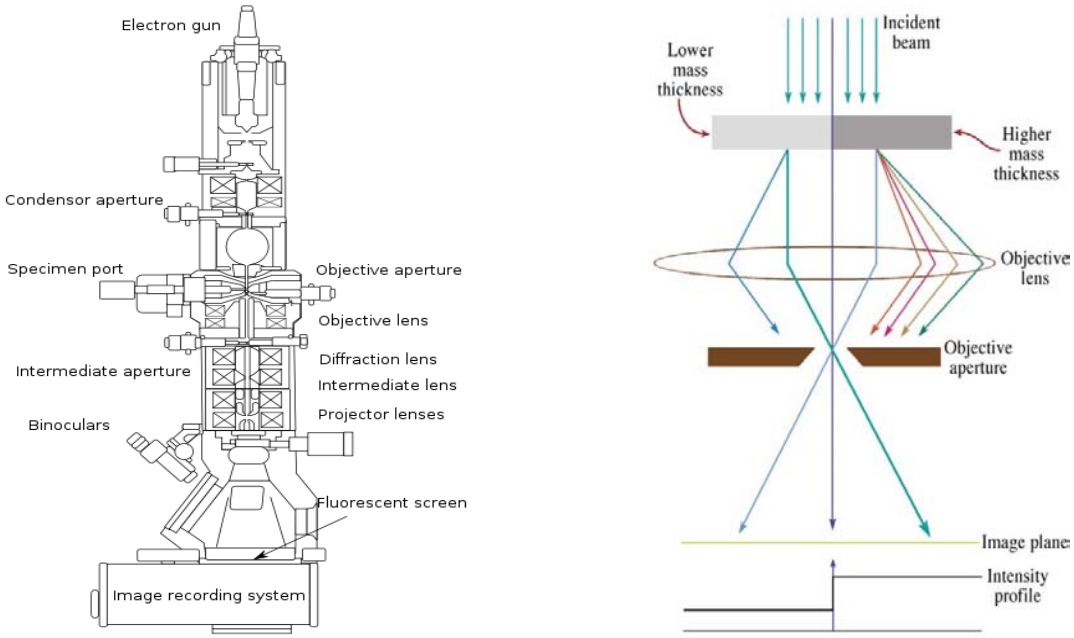

Figure 3.3. (a) Schematic drawing of a TEM apparatus and (b) image formation scheme due to mass thickness difference (35).

A schematic sketch of a TEM is shown in figure 3.3a. Electrons are emitted by a filament when high potential is applied to it, and further accelerated towards the condenser lens system. The lens is physically an electromagnetic field, which increases or decreases the spread of an electron beam. By changing the strength of the EM field, it is possible to control the size of the beam and thus choose the size of illuminated area. An image formed by interaction of electrons with the specimen is projected on the image plane of the objective lens. A set of lenses down the column are responsible for magnifying and projecting an image onto the fluorescent screen or a CCD camera.

The contrast in the EM, which is defined as intensity difference between adjacent areas, is formed thanks to the difference in mass thicknesses and phase contrast when the microscope is operated in bright field mode. The mass thickness is defined by atomic number and actual thickness of the sample. Since heavier elements scatter electrons more efficiently, the area under

these will appear darker. Figure 3.3b schematically shows how intensity profile is affected by mass thickness. In addition to this, phase contrast can contribute to the image formation in the following way: upon interaction of an atom with the electron wave, the phase of the wave can be shifted.

4. Optimization of Ni-Ga catalysts.

4.1. Introduction and first experimental results

This work has been initiated on the grounds of theoretical calculations, and the potential candidates were chosen among the bimetallic systems close to the top of the volcano presented in figure 1.1. From the volcano plot, one can immediately see that copper and Cu-Zn are good catalyst for CO_2 hydrogenation to methanol. Moreover, Ni-Ga looks very attractive since it lies even closer to the top of the volcano plot, and unlike for instance Pd-Ga comprises of relatively cheap metals. Therefore, this was chosen as a first candidate to begin with.

By the time the project was started, no recipe in the open literature (to the best of our knowledge) was available on the preparation of well dispersed supported Ni-Ga nanoparticles. The fastest and easiest method would be to try incipient wetness impregnation, which might or might not work. Several high surface area support materials conventionally used in heterogeneous catalysis were chosen: Al_2O_3, ZrO_2 (both Sigma Aldrich) and SiO_2 (Saint Gobain). The later one is preferred when it concerns scientific investigation: it is X-ray amorphous (i.e. does not produce diffraction peaks in XRD), and it gives a good contrast with Ni and Ga when TEM imaging is required. However, in terms of industrial applications the high surface area silica might not be an optimal solution due to low density, since very often activity per volume of catalyst is one of the most important parameters to optimize.

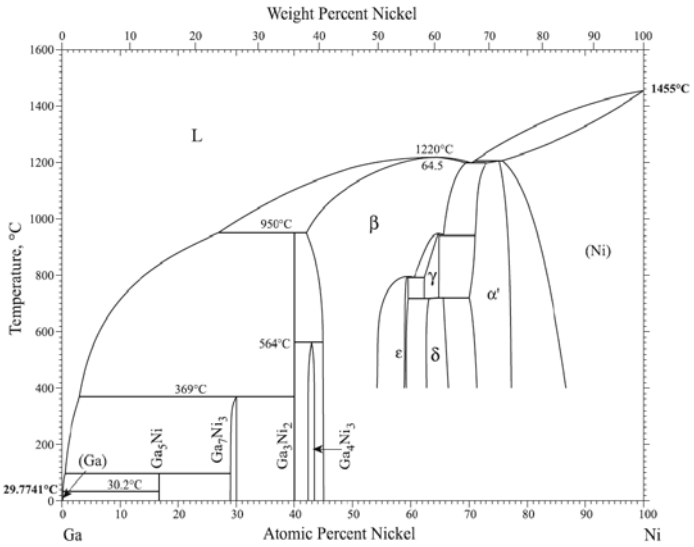

Figure 4.1. Ni-Ga phase diagram (36).

The phase diagram (36) presented in figure 4.1 shows that a variety of Ni-Ga phases can be formed depending on composition and temperature. The DFT calculations were made for certain surface sites rather than bulk composition, therefore it was not obvious from the beginning which

Ni-Ga should be chosen. A 50/50 composition, which corresponds to β-NiGa phase, seemed to be an obvious first candidate. This phase has a relatively wide homogeneity range, and a simple cubic (bcc) crystal structure.

The catalyst was prepared as follows: a mixed aqueous solution of nickel and gallium nitrates was impregnated on SiO_2 bought from Saint Gobain Norpro (area = 241m^2/g), then dried in air at 100^oC, calcined in air at 400^oC and reduced in the flow of pure hydrogen. The mesh size of silica particles was chosen to roughly fit the criteria of $d_{(reactor)}/d_{(mesh)} \approx 10$. This number is very practical because it ensures that the gas flow is equally distributed across the diameter of the reactor tube. On the other hand, the particles are not too small and the risk of upstream pressure build-up is minimized (31).

During the first experiments, many of the above mentioned parameters (reduction/calcination temperature and time, gas composition, metal loading etc) were not optimal and a few unsuccessful attempts were made before methanol peak finally appeared on a chromatogram. No other peaks corresponding to organic compounds were detected; this meant that the choice of Ni-Ga system was quite reasonable. Thus, two catalysts were prepared in a similar way for comparison purposes: Cu/SiO_2 and Ni/SiO_2.

For direct comparison of the catalysts, one needs to define the normalization criteria, which is arbitrary and could be for example activity per mass/volume/active surface area of a catalyst, etc. Here, the starting point for choosing the amount of catalyst was based on the maximum mass of the SiO_2 (mesh size 0.211 to 0.354 mm) that would fit into the isothermal zone of the oven, after being placed into a reactor tube with d_i = 6mm. Since the length of the isothermal zone, here defined as T_{min}-T_{max} < 1.5, was determined to be 5cm, it was decided that the length of the catalyst bed should not exceed 4cm. Hence, it was found that 0.4 grams of SiO_2 should be used to fulfil this criterion. The total loading of Ni and Ga metals is this first successful experiment was 8.5 wt%, and the decision was to maintain the molar amount of metals per gram of support constant for the Cu/SiO_2 and Ni/SiO_2. The same normalization criterion was used throughout the project, although the mass loading was in the most cases different, as it will be mentioned further.

Figure 4.2 shows the results of the first experiment, which already sheds some light into the peculiarities of the NiGa catalysts. In this experiment, three gas compositions were subsequently employed in a similar temperature program. It is immediately obvious that pure CO_2/H_2 feed gives the best results, while pure CO/H_2 does not yield any methanol. Also at each temperature step, the activity is decreasing with time; the effect is most severe when CO and CO_2 are supplied together. No other organic compounds were formed except some dimethyl ether (DME) at the highest temperatures from a $CO/CO_2/H_2$ mixture.

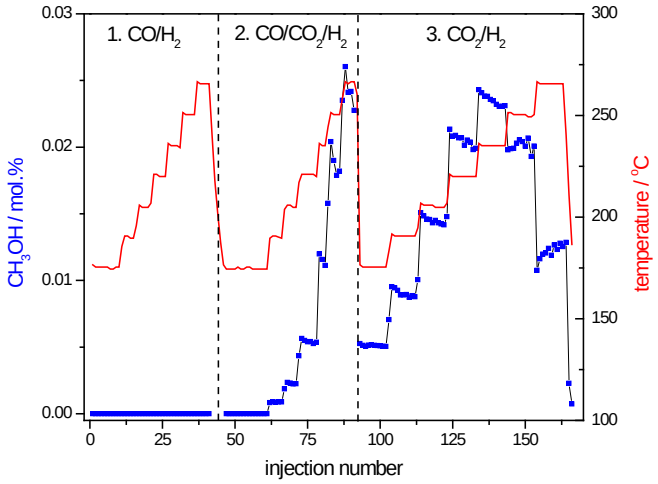

Figure 4.2. The influence of feed gas composition on methanol production. Catalyst: $NiGa/SiO_2$; reaction conditions: P = 1bar, flowrate = 100ml/min. Every injection is equivalent to 15 minutes.

In contrast, the behaviour of Ni/SiO_2 catalyst was proven to be, as expected from the literature (37), very different. In this experiment, all three gas mixtures were employed as well, but in a slightly different fashion: at each temperature step, the gas composition was changed in the following order: $CO_2/H_2/Ar$ (20%/75%/5%), $CO/CO_2/H_2/Ar$ (10%/10%/75%/5%) and $CO/H_2/Ar$ (20%/75%/5%). Only methane production is highlighted in the figure 4.3, although an entire range of C_1-C_3 hydrocarbons was formed. Apparently, methane is formed more readily from the CO-free gas.

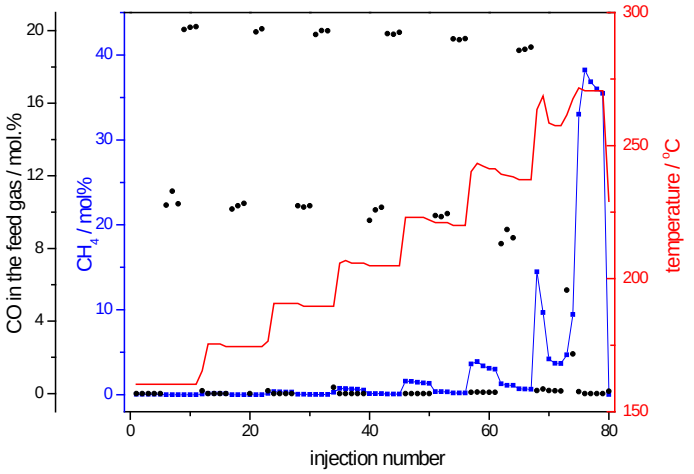

Figure 4.3. Methane production on Ni/SiO_2 over a range of temperatures and feed gas compositions. P = 1bar. Black dots: CO concentration on the feed gas. Every injection is equivalent to 15 minutes.

The other reference catalyst, Cu/SiO_2, turned out to be almost completely inactive, irrespective of the gas composition, and therefore the data is not presented here. Only ppm levels of methanol were detected at highest reaction temperatures (above 220°C).

The difference in the behaviour between $NiGa/SiO_2$ and Ni/SiO_2 is a very good indication that upon alloying with gallium, the more "usual" methanation properties of nickel are significantly diminished. This is most likely due to the fact that nickel is no longer able to break the C-O bond which is the first step in hydrocarbon formation (38), (39).

The catalyst was further characterized by means of TEM and XRD. During TEM session, EDS (energy dispersive spectroscopy) analysis was employed to check the Ni/Ga ratio. Only a few TEM images with rather low magnification were taken at that time, therefore size distribution analysis was not done for this sample. A typical image is shown in figure 4.4a, where both very small and large particles are seen (TEM was done in a dark-field mode). Whether these contain both metals or not was checked using the EDS detector: analysis was performed on 4 different areas, and the results are summarized in table 4.1. In all areas, the Ni/Ga ratio is as expected close to unity. The results of TEM and EDS suggest that both dispersion and distribution of metals in the volume of the support are far from being optimal: some areas barely contain any Ni or Ga (although one should have better statistics in order to claim this confidently). But nanoparticles with the desired composition seemed to be there. To finally confirm this, an ex-situ XRD measurement was done (figure 4.4b). The positions of the observed diffraction peaks do not perfectly match with any of the Ni-Ga reference patterns found in the ISCD (international crystal structure database (40) database. However, reference β-NiGa (50/50 composition) provides the closest fit, although the experimental peaks are shifted to the left with respect to the reference β-NiGa phase. From the broadening of the main peak at $2\theta = 43$ ([011] reflection), the average crystals size is estimated to be 12 nm. It is remarkable though that neither metallic nickel, nickel oxide or gallium oxide are detected with the XRD. This is a good evidence that a mixed Ni-Ga phase/phases were formed.

Now, that a novel interesting catalytic system was found, an optimization work could be started. Optimization was performed in terms of catalyst preparation conditions (calcination/ reduction temperature and time), metal loading, Ni/Ga ratio and type of support. Further in the text, each step is described separately.

But before proceeding further, it should be noted that optimization of Ni-Ga catalysts has been ongoing from the date of the first successful experiment, and it is still far from being completed. For this reason, the order of the chapters in the thesis does not necessarily reflect the chronological order: much of the work has been done in parallel, or, to be more precise, in an iterative fashion. One will notice that in-depth characterisation and deactivation studies were carried out on the samples that later turned out to be close to, but not on top of the "optimization hierarchy" in its present state. Such examples are for instance Ni/Ga ratio and alloying temperature, as will be described later.

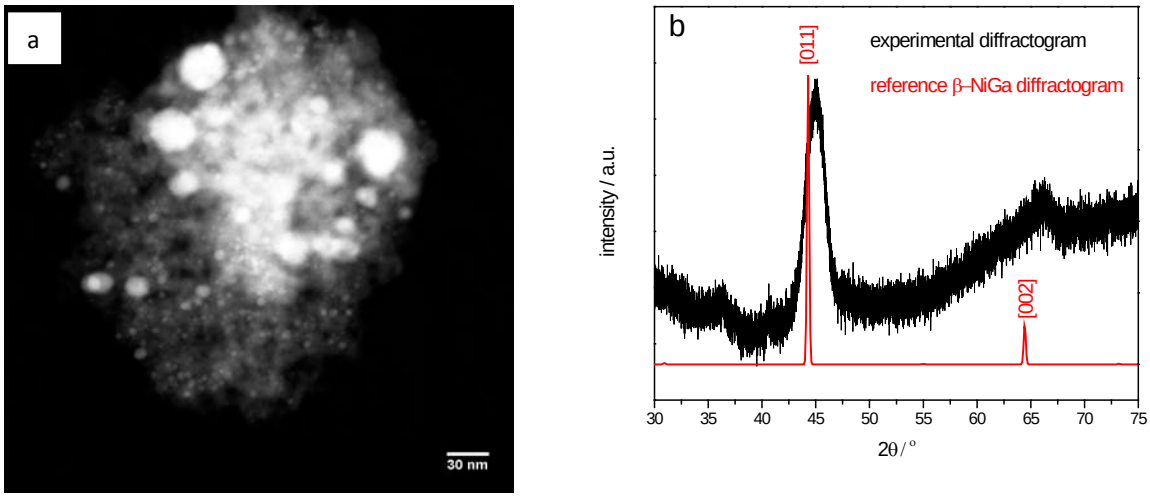

Figure 4.4. (a) – Dark field TEM image of a collection of NiGa nanoparticles on high surface area SiO_2 and (b) – ex-situ XRD pattern of the same catalyst.

No	Atomic% O	Atomic% Si	Atomic% Ni	Atomic% Ga
Spectrum 1	63.4	31.9	2.5	2.2
Spectrum 3	59.5	34.8	3.5	2.2
Spectrum 4	53.4	29.6	7.9	9.1
Spectrum 5	56.0	25.6	9.8	8.6

Table 4.1. Summary of EDS analysis on $NiGa/SiO_2$.

To sum it up, the first methanol-active Ni-Ga catalyst was prepared in the following steps:

- incipient wetness impregnation of metal nitrates

- drying of the precursor (100°C, 24 hours),

- calcination in stagnant air (4 hours, 400°C)

- reduction in pure H_2 flow (20 hours, 700°C)

- testing in stoichiometric CO_2/H_2 mixture (total flow 100ml/min, 25% CO_2 in H_2) at atmospheric pressure in the temperature range of 160-240°C

4.2. First steps in optimization

In this subchapter, several experiments will be described that led to development of a "standard" catalyst preparation procedure, that was further used through the entire duration of the project. One could view these tests as "trial-and error" first optimization steps, which set the stage for further and deeper investigations.

4.2.1. Ni-Ga ratio and alloying time

Figure 4.2 shows the variety of Ni-Ga phases that could potentially be tried for this reaction. To begin with, three compositions were prepared and tested according to the protocol described above, namely, NiGa, Ni_5Ga_3 and Ni_3Ga. These compositions were chosen because they correspond to the β, δ and α` phases, respectively, for which the crystallographic data is available. The results presented in the figure 4.6 give a first overview of the influence of Ni/Ga ratio on methanol production rate.

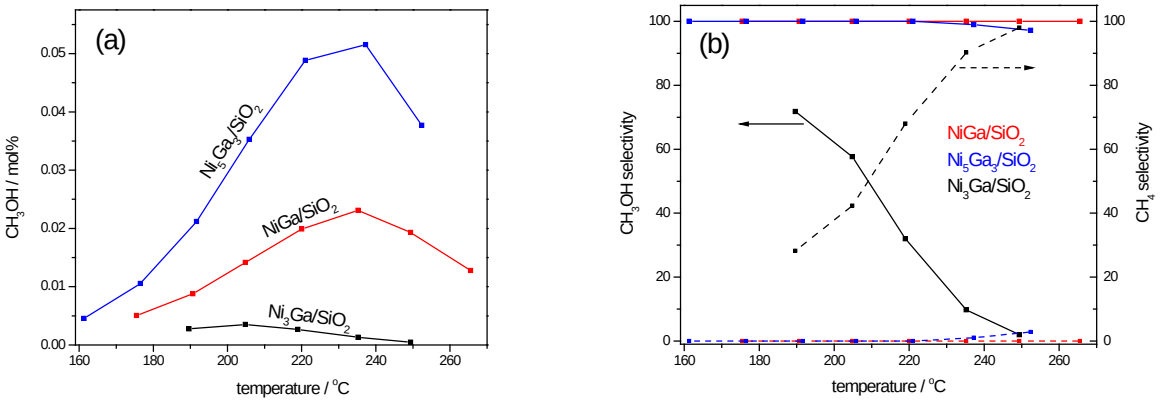

Figure 4.5. Influence of Ni/Ga ratio on (a) activity and (b) selectivity of the SiO_2 supported Ni-Ga catalysts

It is now clear that the Ni/Ga ratio has a major influence on activity: these results suggest that CH_3OH production could be the highest for a certain composition in between 50/50 and 75/25, if one makes a screening for the various Ni/Ga ratios. Whether the maximum will end up at the 5/3 composition is another question, which has also been investigated later (chapter 5.3.1). At this point, the focus has been turned to further optimization of the Ni_5Ga_3 catalyst.

The CH_3OH production rate remained unchanged when the alloying time was reduced from 20 hours ($NiGa/SiO_2$ catalyst, figure 4.2) to only 2 hours ($NiGa/SiO_2$ catalyst, figure 4.5). Therefore, the other two catalysts were prepared in the shorter time frame.

4.2.2. Effect of calcination and metal loading

Calcination is often a required step in catalyst preparation: it is necessary to decompose some of the components of the precursor, to allow solid state reaction between components, redistribute the active species or to enhance porous structure (41). In general, it is well known that the preparation history has a large influence on the catalytic activity (42). For example calcination of the methanol synthesis catalyst precursor, according to (42), is essential due to formation of the metastable amorphous hydrocarbonates and aurichalcite, that finally lead to formation of a very active catalyst.

However, in certain cases the treatment of the precursor in air at elevated temperatures might promote undesired effects such as sintering. Previous studies on preparation of silica supported nickel nanoparticles starting from $Ni(NO_3)_2$ revealed that, if air calcination step is skipped and the nitrate is directly reduced in H_2 flow after ageing in air at 90°C, the resulting dispersion of nickel is significantly improved (43). The detrimental effect of air calcination is assigned to high mobility of NiO at these conditions. Inspired by these results, a direct reduction of a mixture of Ni and Ga nitrates impregnated on SiO_2 was performed.

Optimization of the metal loading is required, as activity per unit volume is an important parameter when it comes to heterogeneous catalysts, especially for high pressure processes where reactor volume should be as small as possible due to high compression costs. In the incipient wetness impregnation method, the volume of the catalyst does not change notably when the metal loading in increased, because the metal salts occupy the internal pore volume of SiO_2. Moreover, nickel and gallium are reasonably cheap metals, so one should in principle try to maximize their content as long as methanol production per amount of metal scales up considerably.

Figure 4.6 represents an overview of the calcination effect and metal loading. First, it should be emphasized how significant the improvement is when the catalyst precursor is directly reduced: the amount of methanol is increased approximately 4-fold (compare the black and dark blue lines at T = 170-180°C). Further, an increase of metal content from 8.5wt% to 17wt% accounts for doubling of the activity, while 29wt% Ni_5Ga_3/SiO_2 shows only slight improvement. Therefore, further experiments were carried out on the directly reduced Ni_5Ga_3/SiO_2 catalysts with 17% metal loading.

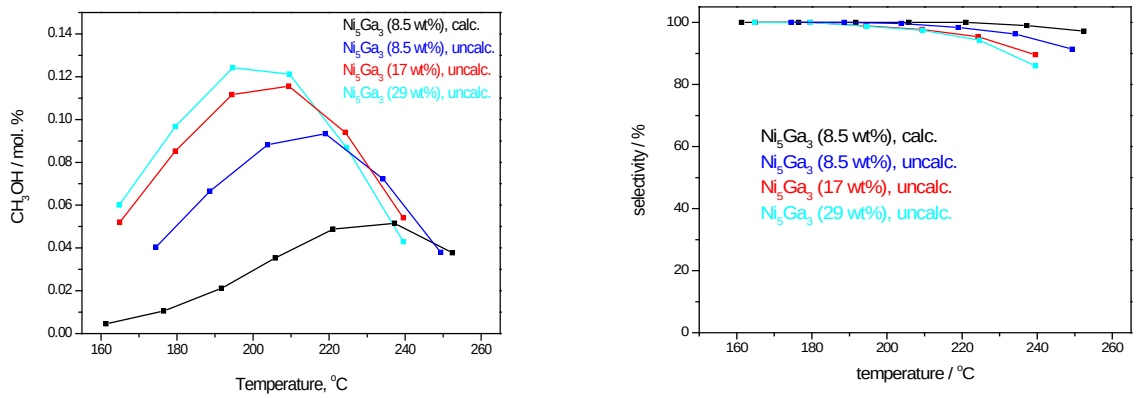

Figure 4.6. Influence of the catalyst preparation conditions and metal loading on (a) activity and (b) selectivity of Ni_5Ga_3/SiO_2 catalysts.

4.2.3. Type of support

Here a few conventional high surface area materials were tried as a support for Ni_5Ga_3 catalyst: γ-Al_2O_3, TiO_2, and ZrO_2. The catalysts were prepared in exactly the same way as those supported on SiO_2. These tests were done before looking into the effect of metal loading, therefore the total amount of Ni and Ga was still 8.5 wt%. The activity results are presented in figure 4.7 which can be compared to the figure 4.6. The rate of methanol production in the later case is higher by an order of magnitude. Moreover, the methanol selectivity is diminished dramatically when metal oxide supports are used: this could be an indication that the alloying of Ni and Ga was not completed within 2 hours in H_2 flow at 700°C, the resulting dispersion was poor, etc. However, no further attempts to optimize these catalytic systems were undertaken.

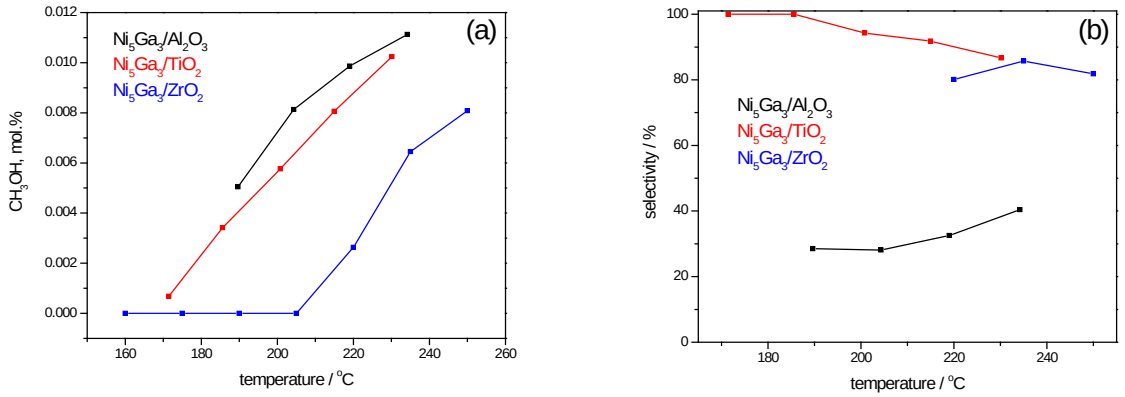

Figure 4.7. Influence of the support on (a) catalytic activity and (b) selectivity of Ni_5Ga_3/SiO_2

Therefore, it was decided that high surface area SiO_2 should be used as a support material for further studies. As mentioned earlier, the advantage of SiO_2 is in its convenience for characterization using x-ray techniques and electron microscopy.

At this point, the dynamic (or one might say, chaotic) part of the optimization was ended. Definitely many other things could be tried: preparation of Ni-Ga catalysts by co-precipitation through a hydrotalcite-like precursor as suggested in (44), calcination of the precursor in dilute NO flow which could improve the dispersion (45), optimization of the Ni-Ga catalysts impregnated on different supports. The idea was however to invest more time into investigation of Ni-Ga nanoparticles formation, and factors governing the activity, selectivity and stability of this novel catalytic system.

5. Further investigations into SiO_2 supported Ni-Ga catalysts.

Admittedly, the ability to synthesize supported Ni-Ga nanoparticles in such a straightforward way is an exceptionally fortunate situation. In many cases, this is not a trivial task. There are several systems where supported intermetallic nanoparticles with controlled size and morphology were synthesized following conventional chemical procedures. For example, Pd_2Ga nanocrystallites were prepared by impregnation of the acidic solution of metal nitrates into carbon nanotubes and shown to be well dispersed (46). Another example is Pt-Bi, which is interesting as anode-side catalysts in formic acid fuel cells. The authors claim that nicely dispersed 3nm PtBi particles can be formed on mesoporous carbon support (47). But in general, despite the existence of a huge variety of intermetallic phases, preparation of well-defined supported nanoparticles in a sustainable and reproducible way is a major challenge (48). But why intermetallic and alloys are so interesting for catalysis?

The analysis of the literature shows that attention drawn towards the utilization of alloys and intermetallic compounds for catalytic purposes is increasing: in a number of applications, they could represent attractive alternatives to conventional catalysts in terms of cost, activity, stability and selectivity. A good example is in fuel cells where platinum is commercially used as a catalyst for cathodic reduction of oxygen; however, the kinetics of this reaction is far from optimal (49). In this line, a Pt-Y intermetallic catalyst has been reported to possess 6-10 times higher activity than pure platinum. This is explained by modification of the bonding energies of the key reaction intermediates due to alteration of the electronic structure of platinum (50). Long-term stability of the alloy under reaction conditions has to be improved though. Alumina supported Pd-Ag alloy catalysts are widely used in industry for selective hydrogenation of trace amounts of acetylene to ethylene (51). It is believed that diluting palladium surface by silver atoms, i.e. breaking down the surface into smaller Pd islands, leads to partial suppression of coke formation, and hence, improved selectivity (52), (53). Recently, a novel Pd-Ga intermetallic catalyst (IMC) has been shown to have superior properties in terms of activity and selectivity for semi-hydrogenation of acetylene when compared to commercially used Pd-Ag alloy, as well as being more resistant to coking (13) (54). The reason for improvement is believed to stem from the chemical nature of the Pd-Ga intermetallic compounds. In PdGa, for example, no direct Pd-Pd bonds are present in the structure and segregation is reduced due to strong covalent bonding between the two metals (55). In other words, both geometric and electronic structure of Pd-Ga IMC is much more defined then that of Pd-Ag alloy. Another interesting alternative material for C_2H_2 semi-hydrogenation is a recently proposed $Al_{13}Fe_4$ intermetallic phase, which is catalytically similar to PdGa but more attractive in terms of price (56). An enhancement of catalytic properties by using intermetallic compounds instead of metals is observed in the anode side of the formic acid fuel cells. When metallic platinum is used as a catalyst, the presence of large Pt ensembles leads to dehydration of the acid to CO, which acts as a catalyst poison (57). By using Pt-Bi catalysts, the undesired dehydration reaction is almost completely suppressed,

while the selectivity towards dehydrogenation (to form CO_2 and H_2) is greatly enhanced (47). Attempts have been made to utilize intermetallic compounds for methanol steam reforming (MSR) reaction, by utilizing PdZn-based catalysts. The currently used $Cu/ZnO/Al_2O_3$ is known to suffer from sintering under MSR conditions, and produce more than 1000 ppm CO as a by-product (58).

In general, utilization of intermetallic compounds offers a number of benefits for catalytic applications: they are structurally stable due to covalent nature of metal-metal interactions (59) and the electronic structure of the active metal can be modified depending on the nature of neighboring atoms. They are an excellent example of the concept of site isolation, which is believed to be required in a number of heterogeneous catalysis applications (60).

In the end, it is the electronic structure of the active site that largely determines the reaction pathway in a catalytic process. In this line, it has been demonstrated that this structure can be fine tuned by means of alloying (61). The concept of tailoring the reactivity in this fashion is very attractive, as in principle there is an incredible variety of binary and ternary (and even higher order) alloys and intermetallics. But the question major challenges are:

- How to pick out appropriate candidates for a particular reaction? Theoretical screening tools such as DFT are used for this but they need further improvement

- How to prepare well-characterized supported intermetallic phases?

There are obviously other considerations general for all heterogeneous catalysts: stability, selectivity, cost est., which should be taken into account as well.

5.1. Synthesis and characterization of Ni-Ga nanoparticles.

5.1.1. Catalytic data.

After a preliminary work described in chapter 4, a more detailed look into the structure and catalytic properties of Ni-Ga catalysts was required. Moreover, a conventionally used catalyst for methanol synthesis ($Cu/ZnO/Al_2O_3$) had to be prepared and tested in order to see how good or bad these Ni-Ga phases were. A good recepi for preparation of a good benchmarking catalyst was found in (62), where it is claimed that the activity of resulting $Cu/ZnO/Al_2O_3$ is comparable with that of commercial catalytic system.

The catalyst was prepared according to a co-precipitation method as follows: an aqueous solution of copper, zinc and aluminum nitrates and a precipitating agent, Na_2CO_3, were added simultaneously into a millipore water, so that the pH level was maintained at 7±0.2. The

temperature during co-precipitation was 65°C and the entire suspension was constantly stirred. Co-feeding was stopped after 2 hours and aging process was started. During the aging, which lasted one hour, pH was still kept at 7 which required addition of more nitrate solution. The resulting gel was afterwards filtered, washed a few times with millipore water, dried overnight at room temperature, then at 80°C for 4 hours, and finally calcined in air at 300°C for 2 hours. The calcined precursor was pressed, crushed and sieved to obtain 0,212-0,354 mm grains.

As described in section 4.1, the Ni-Ga catalysts were prepared by impregnation of the solution of nitrates into 0.4g of SiO_2 mesh, to obtain 17 wt% loading of metals. Since the $Cu/ZnO/Al_2O_3$ catalyst contained 48 wt% of copper after reduction, the total amount of the catalyst precursor used was 0,166g to match the molar amount of Ni+Ga and Cu in the two catalysts. Therefore, the $Cu/ZnO/Al_2O_3$ had to be diluted with silicon carbide in order to match the volume of silica supported Ni-Ga catalysts. Since reduction of copper oxide is an exothermal reaction (ΔH_f^0 = -84.5 kJ/mol) and local temperature gradients due to heat release could promote sintering of copper nanoparticles, the catalyst activation was performed under mild conditions: 200°C in 1% H_2/Ar flow for 20 hours.

As a quick benchmarking test, BET surface area of freshly prepared catalysts was determined. The measured value was somewhat lower than that reported in the literature (62) (92 m^2/g instead of 110 m^2/g for the). This could be attributed to the very high sensitivity of the structure of the resulting catalysts to process parameters (temperature, pH, ageing time variations could play a big role). But in general, the catalyst seemed to be suitable for comparison purposes.

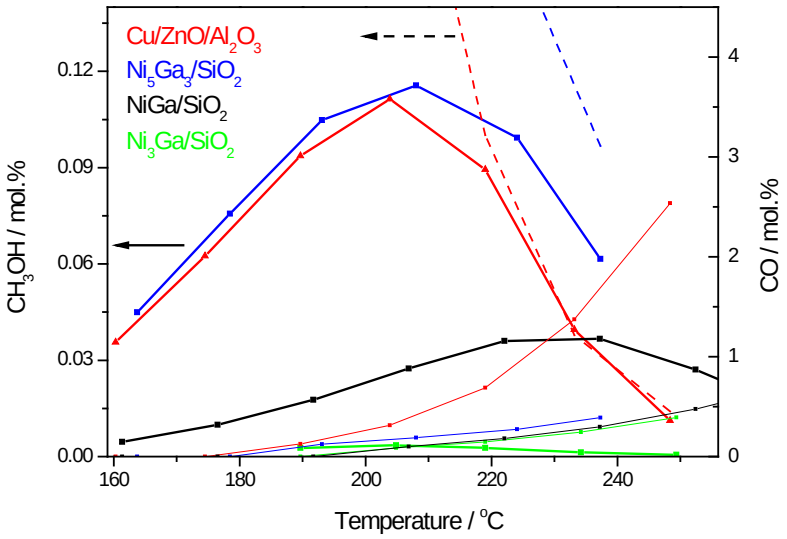

Figure 5.1. Methanol (thick solid lines) and rWGS (thin solid lines) activity of Ni-Ga and $Cu/ZnO/Al_2O_3$ catalysts. Equilibrium methanol conversion presented in dotted lines.

In total, four catalysts were prepared for comparison: $NiGa/SiO_2$, Ni_5Ga_3/SiO_2, Ni_3Ga/SiO_2 and $Cu/ZnO/Al_2O_3$. These were tested under exactly similar conditions: 25% CO_2 in H_2, atmospheric pressure, GHSV = 6000. The activity and selectivity data is presented in figure 5.1 and 5.2.

Although $Cu/ZnO/Al_2O_3$ catalyst is prepared following an optimal procedure, the Ni_5Ga_3/SiO_2 is very similar in term of activity. This is remarkable considering that copper based catalyst tested here is reported to possess even higher activity than the commercial catalyst (62). Comparison between $Cu/ZnO/Al_2O_3$ and Ni_5Ga_3/SiO_2 also reveals that in the later case, the equilibrium methanol conversion is shifted to the right in the temperature axis, as the rate of reverse water gas shift reaction is lowered. Apparently, copper catalyst produces CO much more readily than Ni-Ga catalysts at these conditions. This is reflected in the equilibrium methanol production curves, presented together with the activity data. Equilibrium calculations were made according to the equations 2.7 – 2.10.

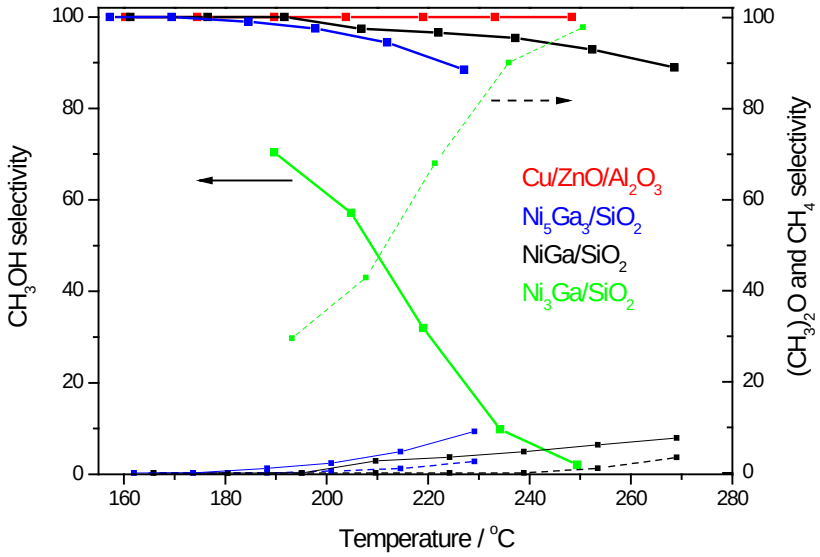

Figure 5.2. Selectivity of Ni-Ga and $Cu/ZnO/Al_2O_3$ catalysts. Thick solid lines – selectivity to methanol; thin solid lines: selectivity to DME+CH_4; dashed lines: selectivity to CH_4. Neither CH_4 nor DME is observed on $Cu/ZnO/Al_2O_3$ catalyst.

Selectivity-wise, $Cu/ZnO/Al_2O_3$ catalyst is very difficult system to compete with, since it produces exclusively methanol (at least within the detection limit of the GC, no other organic compounds are observed). The selectivity has been calculated taking into account only organic substances, i.e. CO-free selectivity. The main organic by-products in the outlet gas are methane and dimethyl ether: while the first one is very undesirable, DME is actually not that bad. If methanol is considered as a fuel, then the presence of the ether should only add up to the calorific value of the fuel. For this reason, methanol selectivity has been plotted together with that of methane to show how much is actually lost due to production the truly undesired product.

When it comes to Ni_3Ga/SiO_2, the picture is completely different to both NiGa and Ni_5Ga_3: this catalyst bears a lot of similarities with metallic nickel: it produces mainly methane, especially as the temperatures goes up, although still generating some methanol at lower temperatures.

To sum it up, it would be fair to assume that our attempt to synthesize a Ni-Ga catalyst for methanol production was successful. The activity and selectivity are quite close to those of the highly optimized Zn promoted Cu-based catalyst, which requires a very complex synthesis procedure.

5.1.2. Characterization: XRD and TEM

The three Ni-Ga catalysts discussed above were also prepared using a lab-scale in-situ XRD setup. The idea was to expose the catalyst precursor to reduction/alloying program similar to that employed in the fixed-bed reactor: the impregnated SiO_2 is reduced at 700C in pure H_2, then cooled down and finally a diffractogram is collected at room temperature. The convenience of utilizing in-situ facilities is that the samples are not exposed to air between synthesis and characterization, which prevents possible re-oxidation or de-alloying.

The diffraction patterns are represented in the figure 5.3, together with the reference patterns from ISCD database (40). The experimental diffractograms match pretty nicely with the ones reported in the literature, meaning that in all three cases the targeted Ni-Ga phase was formed. One could be tempted to immediately conclude that phase pure intermetallic compounds were synthesised upon reduction; however, it is known that XRD is usually “blind” towards very small crystals (less than 1 nm) and amorphous phases. It is also not possible to unambiguously state that all Ni and Ga were combined to form the right phase. But in general, the nature of the formed phase seems to be dictated by the Ni/Ga ratio in the impregnation mixture.

The broadening of the diffraction peak can be used to estimate the average crystalline size of the nanoparticles. From the FWHM of the main peaks, the corresponding values were determined and summarized in table 5.1.

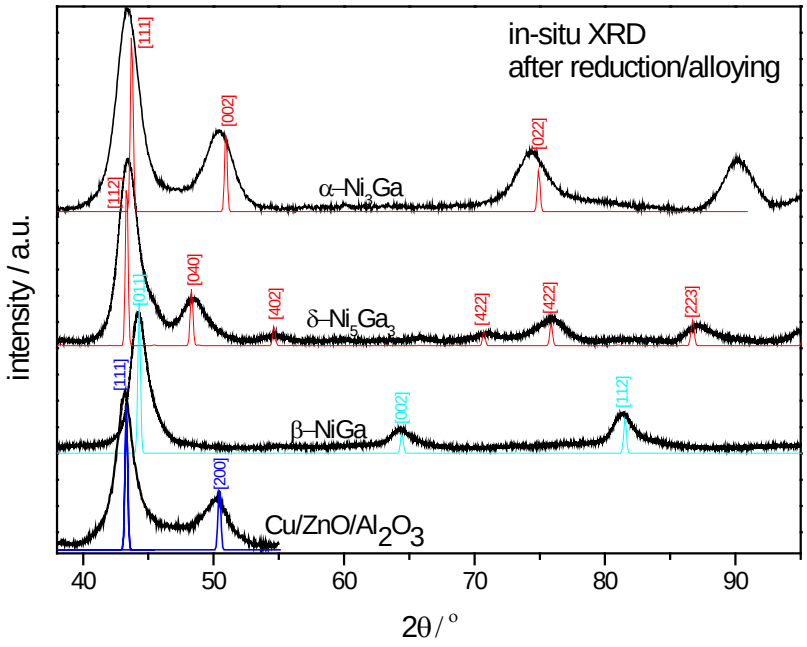

Figure 5.3. In-situ XRD patterns of the as-prepared Ni-Ga and $Cu/ZnO/Al_2O_3$ catalysts.

As a next characterization step, the two catalysts: $NiGa/SiO_2$ and Ni_5Ga_3/SiO_2 were investigated by means of TEM. Since Ni_3Ga/SiO_2 hardly presented any interest from catalytic point of view (for methanol synthesis), it has not been analyzed by electron microscopy. The data on average size and size distribution was obtained after statistical treatment of the images: 219 and 120 particles were analysed in case of Ni_5Ga_3/SiO_2 and $NiGa/SiO_2$, respectively. Slight differences are apparent: for Ni_5Ga_3/SiO_2, average diameter is smaller and particles are more uniform in size ($d = 5.1 \pm 1.4$ nm), while $NiGa/SiO_2$ exhibits broader size distribution: $d = 6.2 \pm 1.3$ nm (figure 5.4). Energy Dispersive X-ray Spectroscopy has been used to confirm that the composition of particles corresponded to 1:1 and 5:3 ratios between Ni and Ga. Resulting TEM data is collected together with the XRD results in table 5.1. For TEM analysis, the values of surface- and volume weighted average diameters were calculated as well according to equations 5.1 and 5.2, respectively. The volume weighted diameters should be used to get an adequate comparison with the XRD data (63).

$$d_s = \frac{\sum n_i d_i^3}{\sum n_i d_i^2} \qquad (5.1)$$

$$d_v = \frac{\sum n_i d_i^4}{\sum n_i d_i^3} \qquad (5.2)$$

The size increment (binning size) ofΔd = 0.5nm was used, and nanoparticles are counted in the intervals of $i \times \Delta d, (i + 1) \times \Delta d$. The data from the two complimentary techniques is in reasonable agreement, meaning that a first picture of how these catalysts look like was drawn at the point.

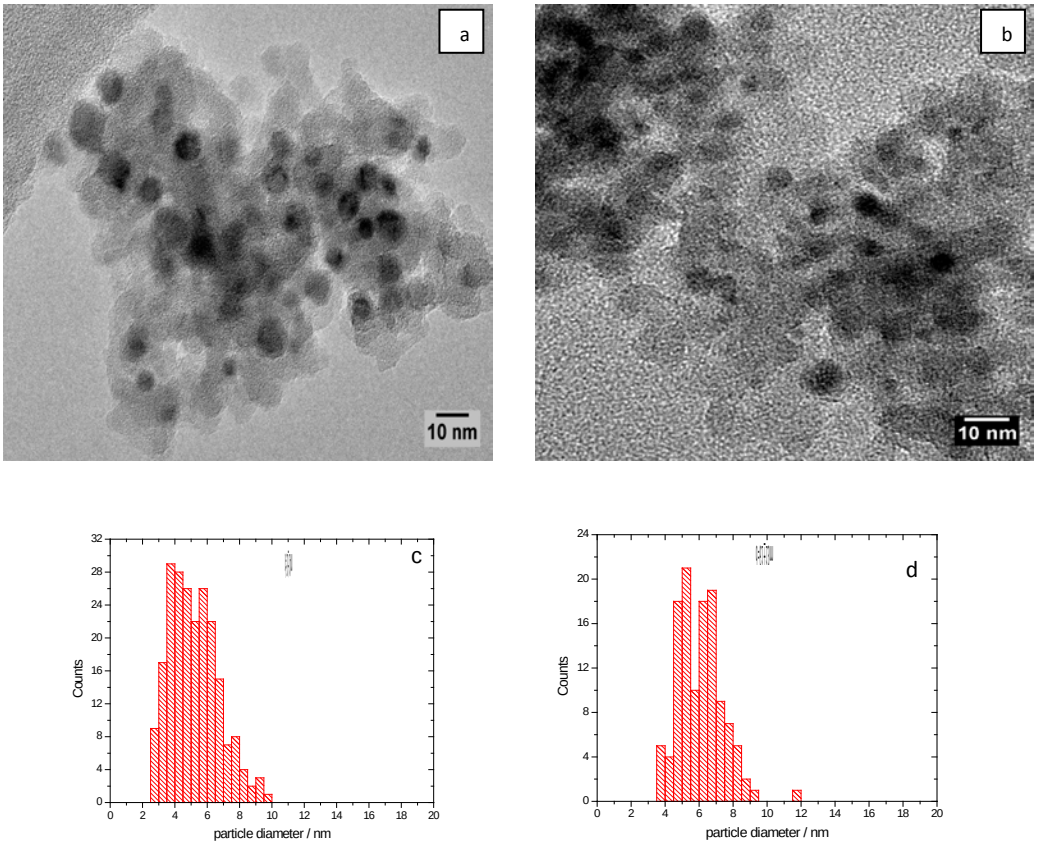

Figure 5.4. Representative TEM images of (a) Ni_5Ga_3/SiO_2 (b) and $NiGa/SiO_2$ catalysts, and corresponding size distribution histograms (c, d).

Catalyst	particle diameter, nm			
	TEM (size distribution)	TEM (surface weighted)	TEM (volume weighted)	XRD (FWHM)
$NiGa/SiO_2$	6.1 ± 1.3	7.2	7.7	7.1
Ni_5Ga_3/SiO_2	5.1 ± 1.4	5.5	6.0	5.9
Ni_3Ga/SiO_2	-	-	-	4.8
$Cu/ZnO/Al_2O_3$	-	-	-	5.7

Table 5.1. Average particle sizes determined by TEM and XRD methods.

Another interesting observation is that the average size of copper crystallites is very similar to those of Ni_5Ga_3/SiO_2 and $NiGa/SiO_2$. Moreover, the molar loading all the catalysts is the same. Consequently, the turnover frequency values (TOF, i.e. activity per surface area) for the Ni_5Ga_3/SiO_2 and $Cu/ZnO/Al_2O_3$ catalysts are very similar. This is very remarkable since the TOF represents the intrinsic activity, which is an inherent property of a material. However, the fraction of the surface that is actually active is difficult to estimate. Even for the $Cu/ZnO/Al_2O_3$ catalyst, which has now been studied for many decades, there are still controversies regarding the nature of active sites. However, DFT calculations do predict the rates of methanol synthesis per active site (which was modelled as a 211step site with Ni on top). Now assuming that these calculations represent what happens on a real catalyst surface, it is possible to estimate what fraction of the surface should be covered by active sites in order to match the DFT-based TOF values.

The experimental TOF calculations (amount of methanol produced per nm^2 of metallic surface per second) are based on the assumption that:

- all particles are spherical and uniform in size

- the average particle size is adequately represented by the average volume weighted diameter

Knowing the rate of CH_3OH production, TOF values for all catalysts under investigation can be now calculated as a function of temperature. For instance, the most active Ni_5Ga_3/SiO_2 catalyst makes $3.5*10^{-5}$ moles of methanol per nm^2 per second. Comparing this value with the one presented in the figure 1.1 (approx. $5*10^{-9}$) implies that the density of active sites should be around 10^4 per nm^2. This is definitely unrealistic since the atomic radii of Ni and Ga are 0.124 and 0.135 nm, respectively (64), meaning that at maximum approx. 10^2 atoms can occupy $1nm^2$. Consequently, the calculated numbers are to a large extent underestimate of the real ones. A work is currently in progress in the direction of screening other possible surface configurations of the Ni-Ga. However, what DFT calculations do provide are the trends in reactivity, thus helping to choose the optimal candidate.

5.2. Formation of Ni-Ga nanoparticles investigated by in-situ techniques.

Here the focus will be on two in-situ characterization methods: in-situ XRD and in-situ XAS. These techniques complement each other nicely because the former one gives information on the long-range order of the crystalline materials, while the later one is convenient to study the local structures, including those of the amorphous materials. In-situ TEM investigations during the formation of Ni_5Ga_3 model system have been performed within the framework of a separate PhD project at DTU CEN (Centre of Electron Nanoscopy), and the reader is referred to a thesis written by Linus Duchstein (65) for further details.

5.2.1. In-situ XRD

5.2.1.1. Brief introduction and practical notes

The main idea behind in-situ XRD experiments was to follow the dynamics of Ni-Ga nanoparticles formation as a function of temperature. The aim was to be able to answer the following questions:

- what are the intermediates during reduction/alloying?
- what is the minimum temperature at which the desired phase is formed?
- is it possible to optimize the preparation procedure further to get a better catalyst?

The experiments were conducted using PAN Analytical X`PERT PRO diffractometer available at DTU Physics. Cu-K_α radiation was employed as X-ray source. In order to get a monochromatic beam, the incoming photon flux was monochromated by a nickel filter. For in-situ XRD measurements, an Anton Paar XRK-900 cell was used and the catalyst precursor was reduced in pure H_2 (total flow: 40ml/min) on the heated sample holder. The sample was heated up to 700^{o}C in steps of 50^{o}C or 100^{o}C and the temperature was kept constant for 2 hours at each step. Short 15 min diffractograms (not presented here) were acquired before and after long 90 min diffractograms, to check for possible phase transformations at isothermal conditions.

The outlet from the in-situ XRD cell was analysed by a Quadrupole Mass Spectrometer (QMA 125, Pfeiffer Vacuum). The ion currents corresponding to the components of the reaction mixture were not subjected to absolute calibration, and were only used for relative quantification.

5.2.1.2. Experimental procedure and results

As mentioned earlier, 2 out of 3 supported intermetallic Ni-Ga phases turned out to be interesting from catalytic point of view, namely, NiGa/SiO_2 and Ni_5Ga_3/SiO_2. Therefore, a series of in-situ XRD investigation during temperature programmed reduction (TPR) of the corresponding precursors were carried out. The evolution of phases is represented on figures 5.5. To assess the crystal structures that develop during TPR, the XRD data was compared to reference structures. Crystal data for these is collected in Table 5.2.

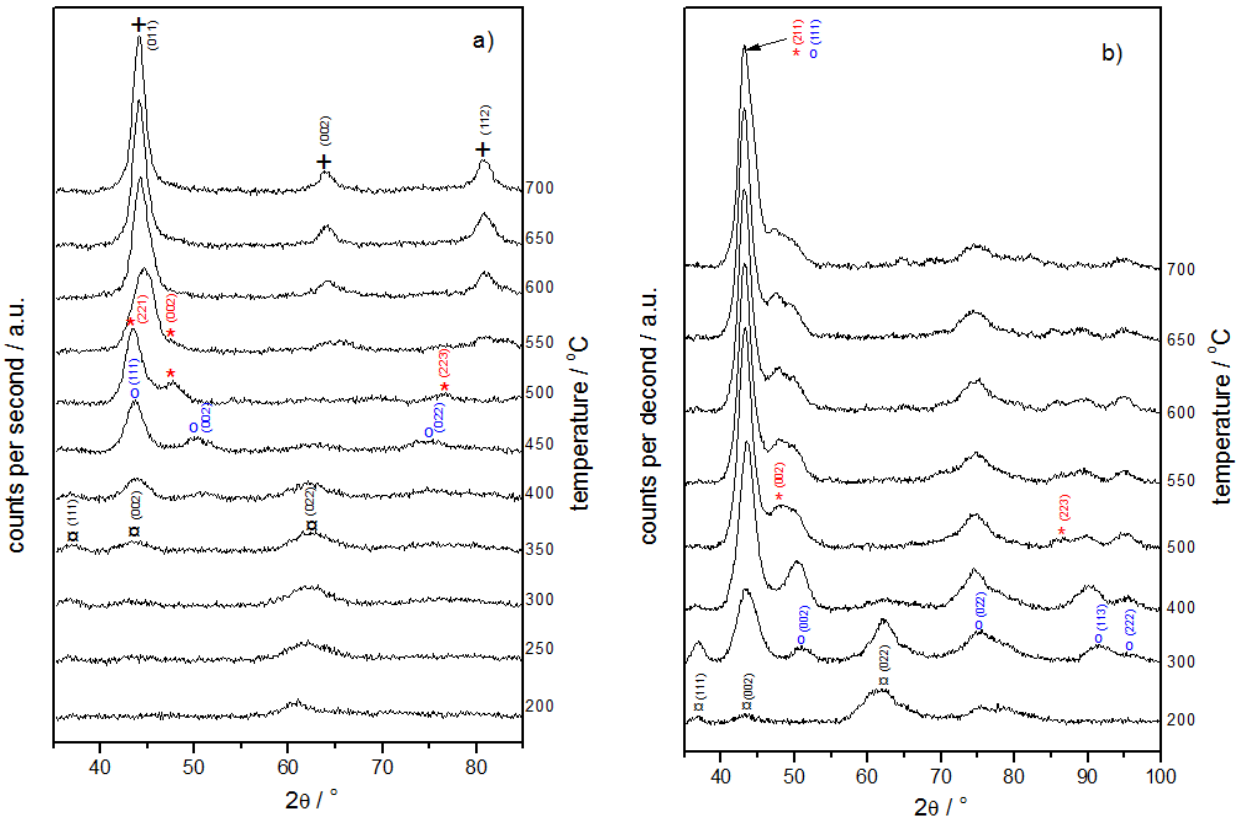

Figure 5.5. Evolution of crystallographic phases during temperature programmed reduction (TPR) to form (a) NiGa/SiO_2 catalyst Ni:Ga ratio 1:1 in the catalyst precursor and (b) Ni_5Ga_3/SiO_2 catalyst Ni:Ga ratio 5:3 in the catalyst precursor. Reflections are marked as follows: *(δ-Ni_5Ga_3), ¤(NiO), o(α`-Ni_3Ga). Gas composition: 90% H_2 in Helium. Total flow rate: 40 ml/min.

A mixture of nitrates containing 1:1 molar ratio of metals impregnated on SiO_2, finally forms a β-NiGa phase. There are several distinct temperature intervals to point out during the TPR experiment, as shown by the in situ XRD data in figure 5.5a: at T > 200°C, formation of NiO crystallites starts. Decomposition of nitrates was also confirmed by mass spectrometry in a separate experiment: at 300°C, a complete transformation to oxides must be assumed, as judged from mass 30 in the figure 5.6. Between 300°C and 350°C, the intensities of the reflections due to NiO are further enhanced which is indicative of sintering during this step. At the same time, water is evolved due to reduction of the oxides. Increasing the temperature further leads to alloying of Ni and Ga, i.e. formation of α`-Ni_3Ga, δ-Ni_5Ga_3, and finally β-NiGa phase, which corresponds to the Ni/Ga ratio in the initial impregnation mixture. The apparent evolution of water at the temperatures higher than 500°C is most probably an indication of water desorption from the internal surface of the in-situ XRD cell. Formation of Ga_2O_3 was not observed during in-situ XRD; this point towards the amorphous nature of the oxide. However, further XAS analysis revealed the presence of this intermediate (see chapter 5.2.2).

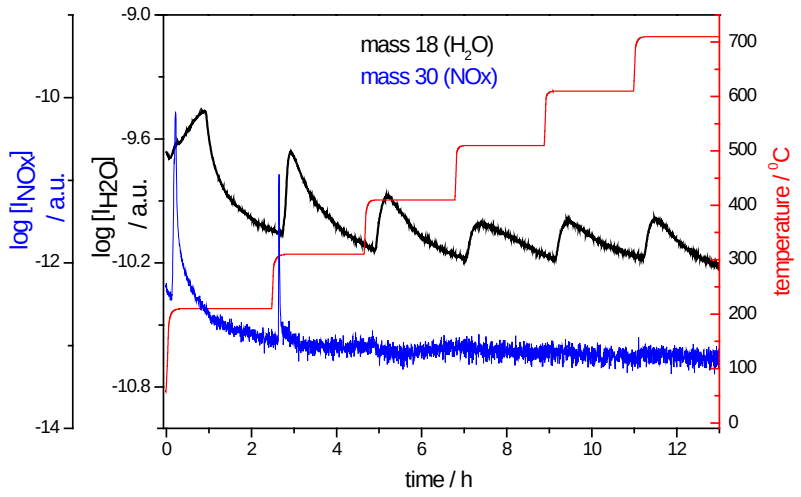

Figure 5.6. Evolution of water (mass 18) and NOx (mass 30) during formation of the $NiGa/SiO_2$ catalyst.

In general, the onset of formation of intermetallic phases in the case of δ-Ni_5Ga_3 synthesis is observed at lower temperature than for $NiGa/SiO_2$: NiO is formed at 250°C, and already at 300°C further changes are seen. At this point the catalyst is a mixture of Ni_3Ga and NiO phases, with nickel oxide as dominant (70%). At 400°C, a mixture of intermetallic α`-Ni_3Ga and δ-Ni_5Ga_3 phases is seen, with further temperature increases leading to an increased fraction of the latter. It appears that, while the transformation of NiO and Ga_2O_3 into a nickel-rich intermetallic state is a relatively easy process, formation of the δ-Ni_5Ga_3 phase is much slower. The final diffraction pattern recorded after reduction at 700°C still does not represent a clear pattern of a phase-pure Ni_5Ga_3/SiO_2 catalyst.

phase diagram			ICSD reference (40)					
phase	Ni, at.%	space group	ICSD code	chemical structure	crystal structure	a [Å]	b [Å]	c [Å]
β	42-69.4	Pm-3m (221)	103853	NiGa	cubic (bcc)	2.886	2.886	2.886
δ	62-67.5	Cmmm (65)	103861	Ni_5Ga_3	orthorhombic	7.53	6.72	3.77
α`	70-77	Pm-3m (221)	103857	Ni_3Ga	cubic (fcc)	3.583	3.583	3.583
Ni	77-100	Fm-3m (225)	-	Ni	cubic (fcc)	3.45	3.45	3.45
NiO	-	Fm-3m (225)	9866	NiO	cubic (fcc)	4.178	4.178	4.178

Table 5.2. Reference data for the relevant Ni containing phases

This is however in contrast to the catalyst prepared under the same conditions in a fixed-bed reactor, which shows a much more pronounced δ-Ni_5Ga_3 pattern with no traces other Ni-Ga phases (see ex-situ XRD spectra, figure 5.3). The reason could be the different nature of the flow through the catalyst bed in the two cases: reduction in a fixed-bed reactor occurs under plug-flow conditions (height to diameter (h/d) ratio of 7-8). Flow conditions during in-situ XRD experiments are remarkably different: the catalyst precursor is placed on a sample plate, where

the h/d value is close to 0.3, which could result in preferential flow path formation and hence longer time to reduce the entire volume of the sample. Apparently, this is not an issue in case of β-NiGa formation, whereas synthesis of a more complex δ-Ni_5Ga_3 requires longer time under in-situ XRD conditions.

On the other hand, the Ni_5Ga_3 diffractogram presented in figure 5.3 is also obtained in the in-situ XRD cell, but it matches much better with the reference pattern. Moreover, the diffraction pattern of another catalyst, $NiGa/SiO_2$, only shows reflections of the pure β-NiGa phase. This phenomenon was very puzzling, and at this stage it is left for the conclusions section, where it is discussed in the light of certain experiments performed later.

5.2.1.3. Rietveld refinement.

After the experiments were done and the observed peaks could be qualitatively assigned to certain phases, quantitative phase analysis was preformed. For this, Rietveld refinement was performed using X-Pert High Score Plus software, which uses the refinement program based on the source code of the program LHPM (66). The procedure was done assuming Pseudo Voigt peak function for all peaks. Refinement was done by fitting various combinations of Ni-Ga phases, until a satisfactory agreement between the experimental and fitted patterns was achieved.

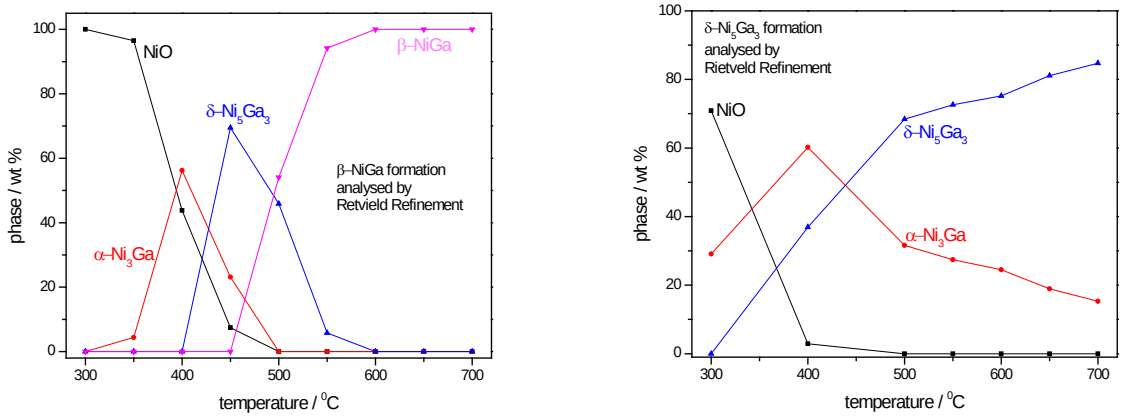

Figure 5.7. Rietveld refinement analysis of the phases formed during temperature programmed reduction of metal nitrates to from (a) $NiGa/SiO_2$ and (b) Ni_5Ga_3/SiO_2.

Rietveld refinement of the intermediate phases during preparation of $NiGa/SiO_2$ catalyst is presented in figure 5.7a. It should be noticed that formation of the final β-NiGa phase goes through more nickel rich intermediate phases, and co-existence of two or more phases is possible at intermediate temperatures. The results of the refinement should not be used for absolute

quantification of the phase composition, since the diffraction patterns were not acquired at room temperature. However, the analysis allows following the dynamics of phase transformations.

For the catalyst impregnated with a mixture of nitrates corresponding to Ni_5Ga_3/SiO_2, the Rietveld refinement (figure 5.7) was more difficult to apply due to combination of several phenomena: more complex structure of the Ni_5Ga_3 phase, co-existence of phases with closely lying reflections at higher temperatures, and the absence (or amorphous nature) of reflections from certain crystallographic planes

To sum it up: in the case of β-NiGa, the composition of the final phase corresponds to the Ni/Ga ratio in the mixture of metal nitrates. For δ-Ni_5Ga_3, some 15% α`-Ni_3Ga is present together with a targeted phase. This means that given high enough temperature, a desired phase is formed in a relatively short time scale compared to the preparation of bulk Ni-Ga intermetallic compounds which requires much longer time due to slow diffusion rate (67). However, the presence of the α`-Ni_3Ga implies that some gallium is present in an unalloyed state (approximately 4% of the total gallium loading).

Metallic nickel has not been observed in either case meaning that reduction of the NiO crystallites must be immediately followed by incorporation of gallium into the crystal structure of nickel. Table 5.3 summarises the changes in average particle size during TPR, estimated from Rietveld Refinement analysis. For both systems under investigation, particle size increases during reduction, which should be expected due to incorporation of gallium to form an intermetallic phase. The average number of nickel atoms per particle at a given temperature was calculated, taking into account the phase composition derived from Rietveld analysis according to the equation given below:

$$N_T = \left[\frac{\left(\sum_i \frac{\omega_i \cdot V_i}{n_i} \right)}{\frac{4}{3} \cdot \pi \cdot r^3} \right]_T \qquad (5.3)$$

where N_T is a number of nickel atoms per average nanoparticle at the temperature *T*; ω_i – weight fraction of phase *i*, found by Rietveld refinement; V_i – volume of the unit cell of the phase *i*; n_i – number of nickel atoms in the unit cell of phase *i*; r – diameter of an average nanoparticle.

When β-NiGa is synthesised, the number of nickel atoms per particle does not change significantly between 300°C and 500°C, meaning that at this temperature interval particle growth occurs primarily due to alloying. When the temperature is further increased, the N_T value grows, implying that sintering occurs at T > 500°C. In the case of δ-Ni_5Ga_3 formation, the average number of nickel atoms per nanoparticle increases in the entire temperature range, suggesting that both sintering and alloying are contributing to the increase in particle size during TPR. As

discussed above, the results of Rietveld analysis should not be used for absolute quantification; however, it allows distinguishing between different particle growth mechanisms during TPR.

Temperature, °C	β-NiGa		δ-Ni_5Ga_3	
	average diameter, nm	number of Ni atoms in the particle	average diameter, nm	number of Ni atoms in the particle
300	4.4	2450	4.1	2100
400	4.4	2700	4.9	3800
500	4.7	2700	5.3	4900
600	5.2	3200	5.9	6800
700	6.1	4900	6.0	7100

Table 5.3. Particle size as s function of temperature during TPR experiment.

To explain the mechanism of the formation of intermetallic Ni-Ga nanoparticles, analysis of thermodynamic and crystal structure data is needed. Formation of Ni_3Ga as a first intermediate compound at the lowest temperature can be explained taking into account the following considerations: both Ni and α`-Ni_3Ga have the same crystal structure, namely face centre cubic (fcc). Hence, incorporation of gallium metal to form the Ni_3Ga occurs without changing the crystal structure of nickel, and should be relatively easy process. According to both theoretical (68) and experimental (69) studies, the formation of nickel-rich Ni-Ga phases is an exothermal process: approximately -30 to -50 kJ/mol with increasing heat effect towards equimolar Ni/Ga ratio. However, there is apparently a significantly higher kinetic barrier for the formation of the δ-Ni_5Ga_3 and β-NiGa phases. This could be due to re-arrangement of the crystal structure to orthorhombic (δ-Ni_5Ga_3) and body centre cubic (β-NiGa), which requires a rather high activation energy.

Although the interpretation of the experimental results does not seem to be straightforward, it is clear that the intermetallic phases are formed in a reasonable timeframe. In-situ XAS measurements were employed to get a deeper look into the alloying process.

5.2.2. In-situ XAS

5.2.2.1. Brief introduction and practical notes

In order to get a better understanding of the formation of supported Ni-Ga nanoparticles, a series of in-situ X-ray adsorption experiments during temperature programmed reduction of the nitrates impregnated on the high surface area SiO_2 support were carried out. The Ni_5Ga_3/SiO_2 system was chosen, as it was shown to possess the highest activity among Ni-Ga catalysts tested so far.

The XAS measurements were carried out in transmission mode at the X1 beamline, in the DORIS III Synchrotron facility, Germany, using Si (111) double crystal monochromator. The XAS spectra were recorded at both Ni and Ga K-edges. The catalyst precursor was subjected to temperature programmed reduction in 90% H_2/He mixture: the sample was heated in 5^{o}C/min, while the temperature was measured by a thermocouple placed directly below the capillary. The sample was heated by a hot air blower.

EXAFS data treatment was carried out using Athena and Arthemis software of IFEFFIT package (70). The spectra were energy calibrated from a reference metal foil, the background was extracted and then normalized.

5.2.2.2. Analysis of normalized and Fourier transformed data

The normalized spectra at the Ni and Ga K-edges during catalyst formation are presented in figures 5.8. As expected, the edge jump in both cases corresponds to the expected values of 7478.2eV for nickel and 9251.6eV for gallium (71). Groups of absorption spectra corresponding to different temperature intervals can be pointed out; they are depicted here in different colours. These changes are invoked by the variations of the local environment around both absorbers: nickel and gallium.

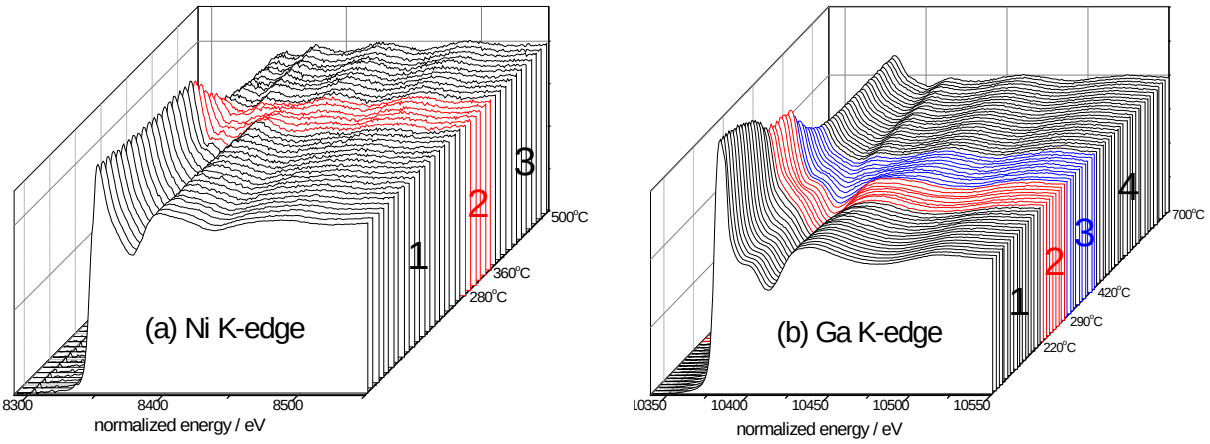

Figure 5.8. Normalized absorption spectra recorded at the a) Ni K-edge and b) Ga K-edge during temperature programmed reduction of metal nitrates to form Ni_5Ga_3/SiO_2.

Analysing Ni absorption edge, 3 groups of spectra are clearly seen: between room temperature and 280°C, neither near-edge, nor oscillatory part of the XAS spectra is affected significantly. Between 280°C and 360°C, the intensity of the Ni edge is rapidly decreasing. Above 360°C, no further variations in the normalized absorption spectra are seen. At the Ga K-edge, four intervals can be distinguished: below 220°C, the initially present $Ga(NO_3)_3$ is converted to an intermediate substance that is apparently stable at 220C-280°C. Further transformations lead to formation of

gallium species in their final state. The first guess on the nature of the intermediate and final states can be made based on the already available in-situ XRD and mass-spectroscopy data. The reduction of Ni and Ga nitrates to oxides occurs roughly between 200°C and 300°C. Therefore, intermediate species seen at the Ni K-edge at 280°C and Ga K-edge at 220-280°C are most probably metal oxides (NiO and Ga_2O_3). After the reduction is completed, both metals are mainly present in an alloyed state according to Rietveld refinement data. Consequently, the steep decline of the edge height depicted in red and blue for Ni and Ga, respectively, can be attributed to reduction of oxides into metallic/intermetallic states.

In order to appreciate how the local environment around the absorber atom is changing, R-space Fourier Transformed (FT) EXAFS spectra recorded at the Ni and Ga K-edges during TPR are represented in the figures 5.9. The temperature step between two consecutive spectra is approximately 10°C. The FT spectra allow distinguishing certain changes which are not directly apparent from the normalized spectra. In fact, the R-space spectra are changing continuously during the TPR experiment, at least due to the temperature effect (Debye-Waller factor).

At the Ni K-edge, main variations of the local environment around nickel are becoming apparent already at 230°C (highlighted in red): the intensity of the main peak at 1.55Å vanishes and a new series of peaks at 2.1Å and 2.5Å emerge. The system is very dynamic between 230°C and 360°C, implying that main structural changes occur at this temperature range. At T > 420°C, the structure is stabilized, and only strong backscattering contribution at 2.1Å is seen. At the Ga K-edge, a similar picture is observed: there are three distinct temperature intervals corresponding to different states of the system. Below 250°C, the local environment of the gallium is very similar to the initial mixture of nitrates. Between 250°C and 420°C, similar to that of nickel, local environment of gallium is changing drastically. At higher temperatures, only one strong peak at around 2.1Å is observed.

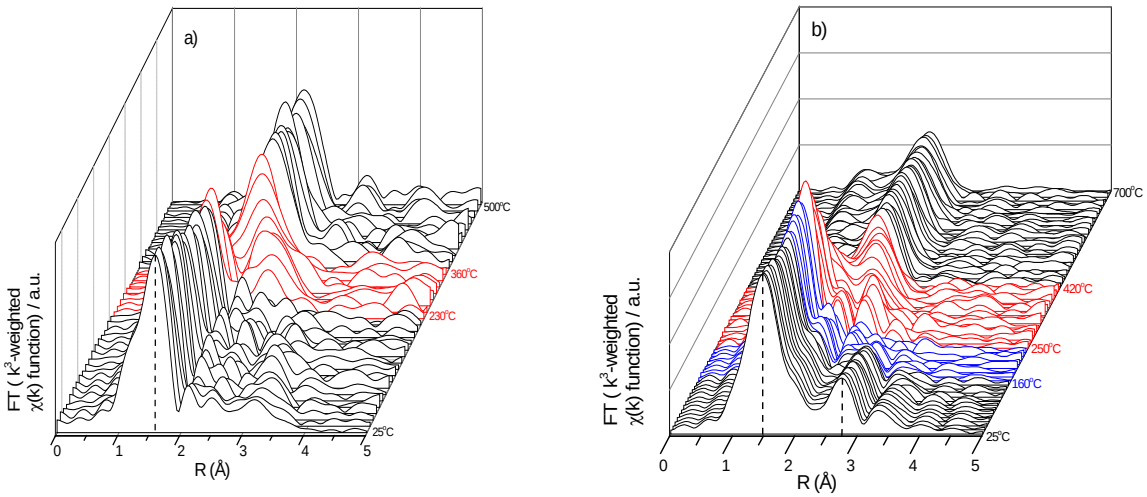

Figure 5.9. Fourier Transformed EXAFS profiles at the a) Ni K-edge and b) Ga K-edge during temperature programmed reduction of metal nitrates to form Ni_5Ga_3/SiO_2

It is important to note that the main backscattering contribution to the final spectrum is observed at 2.1Å in the R-space representation of both Ni and Ga edges. This suggests that the average Ni-Ga distance corresponds to the average Ga-Ni distance, which indicates that the two metals are intimately alloyed. Figure 5.10 shows the FT EXAFS spectra of metallic Ni, metallic Ga, as well as Ni and Ga in the Ni_5Ga_3/SiO_2 catalyst after reduction. Nickel and gallium foils were used to obtain the corresponding reference spectra. All spectra are acquired at room temperature.

From the figure it is clear that the spectra at nickel and gallium K-edges of the as-prepared Ni_5Ga_3/SiO_2 catalyst are quite different from those of metallic references: the position of the main peak in the case of gallium is shifted to lower values, which supports the idea that the state of Ga in the Ni_5Ga_3 is not metallic, but rather intermetallic. In the case of pure Ni, a lack of long range order is seen at the Ni K-edge of the Ni_5Ga_3. This cannot be explained by small particles size (a typical radius of the Ni_5Ga_3 nanoparticle is $\approx$ 2 5Å), but could be due to a complicated crystal structure of the ed compound. If a large number of various interatomic distances are present in the 2nd, 3rd, etc coordination shells, then relatively weak backscattered signals are expected. It is remarkable though that the position of the main peak, which represents the first coordination shell, is similar in the case of both Ni and Ni_5Ga_3. This implies that the *average* "Ni - Nearest Neighbour" distance is somewhat similar in the two cases. The result could provoke one to conclude that a footprint of metallic nickel is seen in both instances; however, crystal structure fitting analysis is required before drawing any conclusions. The later analysis will be presented in a publication that is currently under preparation (72); it shows that the fit between the reference (Ni_5Ga_3) and experimental structure is reasonably good.

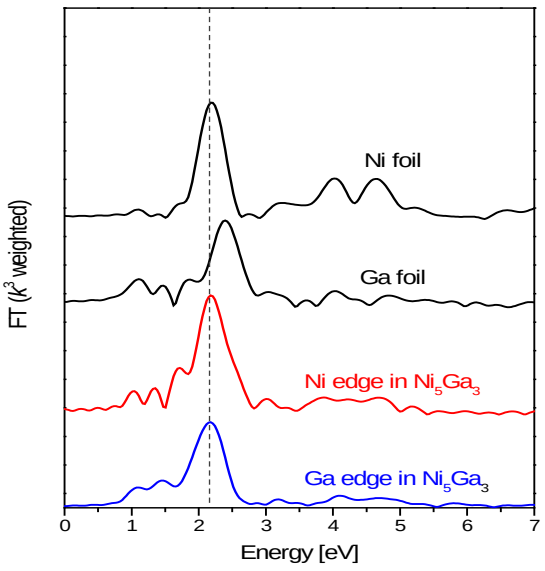

Figure 5.10. FT EXAFS spectra of the pure metals and a Ni_5Ga_3 phase.

The problem is that another Ni-Ga phase, Ni_3Ga, could also be nicely fitted to the experimental structure, meaning that *EXAFS does not give an unambiguous answer on the nature of the final Ni-Ga phase*. However, it does provide a strong evidence that *both metals are reduced and alloyed* after a TPR experiment.

Now let`s turn attention back to the analysis of the normalized spectra. An onset of the reduction of gallium oxide (280^oC) is slightly higher than that of nickel oxide (250^oC), which could indicate that reduction of nickel oxide triggers further reduction of gallium oxide. The rather low reduction temperature of Ga_2O_3 is not directly intuitive; however, the XAS investigations of reduction of this oxide under similar conditions were unfortunately not carried out, as this would provide insights into the role of nickel. Armbruster et al (73) investigated the formation of Pd-Ga nanoparticles in a strongly reducing liquid media and suggested that the reduction of Ga takes place on the surface of already reduced palladium nanoclusters by atomically dissolved hydrogen therein. In other words, gallium oxide only starts to reduce after a certain amount of metallic palladium is formed. A similar scenario, where a freshly reduced platinum nanoclusters induce the reduction of copper to form Pt-Cu nanoparticles is proposed in (74). The mechanism might take place in the case of Ni-Ga nanoparticle formation, since metallic nickel readily chemisorbs hydrogen at these temperatures (75). The results of in-situ XRD experiments discussed earlier also shows that gallium is immediately incorporated into the structure of nickel as soon as the later specie is formed from nickel oxide, since no metallic nickel has been detected during TPR.

5.2.3. Complementary TGA data

Thermogravimetric data, i.e. the data on dynamics of mass loss during the temperature programmed reduction of Ni and Ga nitrates is relatively simple but informative technique to back up the in-situ XRD and in-situ XAS data. In an ideal case, when the exact composition of the catalyst precursor is known, it is possible to calculate the expected mass loss at different temperatures. For this, a mixture of nitrates supported on SiO_2 would be subjected to a TPR experiment similar to that employed in one of the two in-situ techniques mentioned above. Then it should be straightforward to check if the phase composition of the Ni_5Ga_3 precursor found by means of Rietveld refinement, for instance at 300°C (figure 5.7), makes sense. Moreover, TGA could reveal if (and at which temperature) the metals are completely reduced to a metallic state. But in practice there are a few complications that limit such a detailed analysis.

First of all, a catalyst precursor is prepared by means of incipient wetness impregnation of high surface area silica, which implies that the water content of the material is poorly defined. Secondly, the maximum H_2 concentration in the reducing mixture could be as low as 4 vol.% due to technical limitations of the TGA apparatus. Moreover, previous studies on thermal decomposition of pure Ni and Ga nitrates have shown that these processes do not follow a simple

"nitrate-oxide-metal" route. $Ni(NO_3)_2*6H_2O$ goes through several intermediate hydrated states, followed by the formation of hydroxynitrates and oxides (76). The gallium nitrate case is even more complicated: the decomposition is accomplished by continuous mass loss starting already at 30°C (77). In the present case, the analysis is complicated by the simultaneous presence of the two salts, together with unknown amount of absorbed water which is expected to show a continuous desorption profile at low temperatures.

However, certain information can be extracted from a TGA profile corresponding to formation of Ni_5Ga_3/SiO_2 presented in the figure 5.11. In this experiment, a sample dried at room temperature was placed on a flat ceramic crucible and heated in 4% H_2/N_2 flow at 5°C/min. First, there is a significant mass loss curve at T < 130°C, indicating desorption of water and partial dehydration of the nitrates. Further, nitrates are decomposed to oxides (until 280°C), and oxides are reduced to metallic/intermetallic states at higher temperatures. The very distinct change in the mass loss kinetics at 280°C correlates very nicely with the changes observed at the normalized absorption spectra presented in the figure 5.8. At T > 280°C, reduction of oxides accomplished by the formation of intermetallic phases has been previously suggested (Rietveld refinement, figure 5.7). At 650°C, mass loss reaches a constant value of 41.2%. Surprisingly, this is even lower than it would be expected for complete thermal decomposition of anhydrous metal nitrates (42.7%). This suggests that complete reduction of the oxides to metallic states was not achieved in this experiment, probably due to mild reduction conditions. Otherwise, a significant portion of the nitrates should be decomposed before the experiment, which is very unlikely as the precursor was dried at room temperature (76), (77).

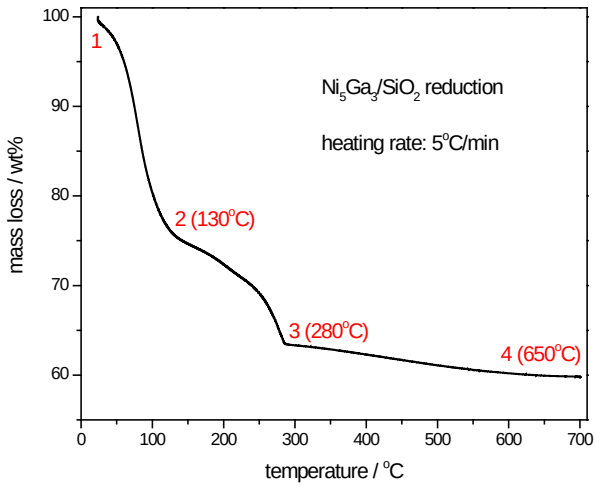

Figure 5.11. Thermogravimetric analysis of the formation of Ni_5Ga_3/SiO_2. Gas composition: 4% H_2 in N_2, flowrate: 120 ml/min.

A combination of in-situ XRD and in-situ XAS experiments provide a strong evidence that a desired Ni-Ga phase can be achieved given that the reduction temperature is high enough.

Comparative analysis of the results obtained from both techniques allows proposing the formation mechanism of the intermetallic Ni-Ga phases during reduction from nitrates. At the low temperature range (below 300°C), NiO nucleation sites are being formed, while at higher temperatures Ga is alloyed with Ni as it is reduced from Ga_2O_3. Alloying always proceeds through more Ni rich phase until stoichiometric composition is achieved, given long enough reduction time and high enough temperature. The proposed mechanism of the δ-Ni_5Ga_3 phase formation is summarized in figure 5.12.

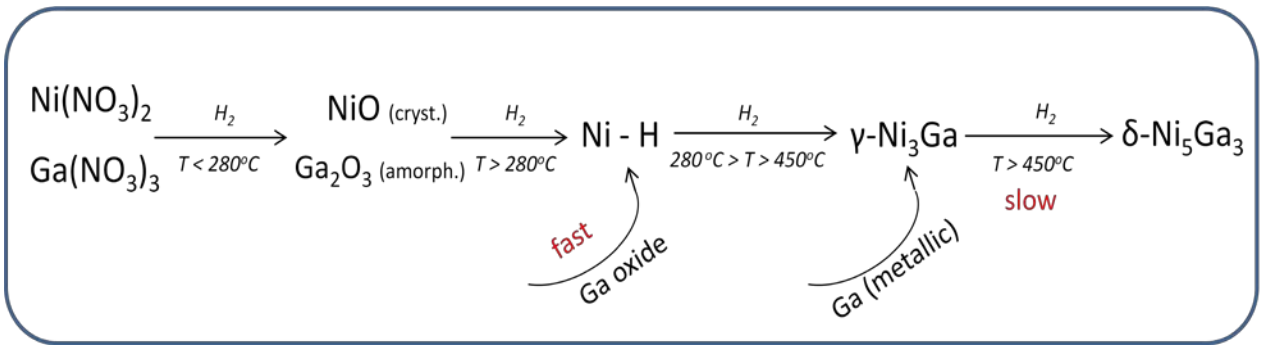

Figure 5.12. Proposed mechanism of Ni_5Ga_3/SiO_2 formation during temperature programmed reduction form metal nitrates.

5.3. Further optimization of the Ni-Ga catalysts

5.3.1. Optimization of the Ni/Ga ratio

In the previous chapters, the Ni_5Ga_3 composition (62.5% nickel and 37.5% gallium) corresponding to the δ-phase was assumed to be the most active among Ni-Ga intermetallic phases for methanol production from CO_2 and H_2. In order to check if this is really the case, a series of Ni_aGa_b/SiO_2 catalysts with varying Ni/Ga atomic ratio were prepared and tested. Figure 5.13 shows methanol production and selectivity as a function of nickel content for two different temperatures. Here only the selectivity towards organic compounds is considered, i.e. not taking into account CO formation in the reverse water gas shift reaction. The specific activity values are based on ex-situ XRD data that was collected after catalytic tests and further used to calculate the average particle diameter according to the Scherrer equation. The reason for presenting methanol production rate in two different ways is to compare both overall and intrinsic activity. In both cases, there is a clear maximum in methanol production at around 65-67% Ni, which falls into the δ-phase region and is very close to the Ni_5Ga_3 composition. Selectivity is 100% at 165°C except for Ni_3Ga, whereas at 205°C in decreases with increasing Ni content. Interestingly, there is a selectivity plateau (approx. 98.5%) between 62,5% and 67,5% nickel, which are the boundary concentrations for the δ-phase (see table 5.2).

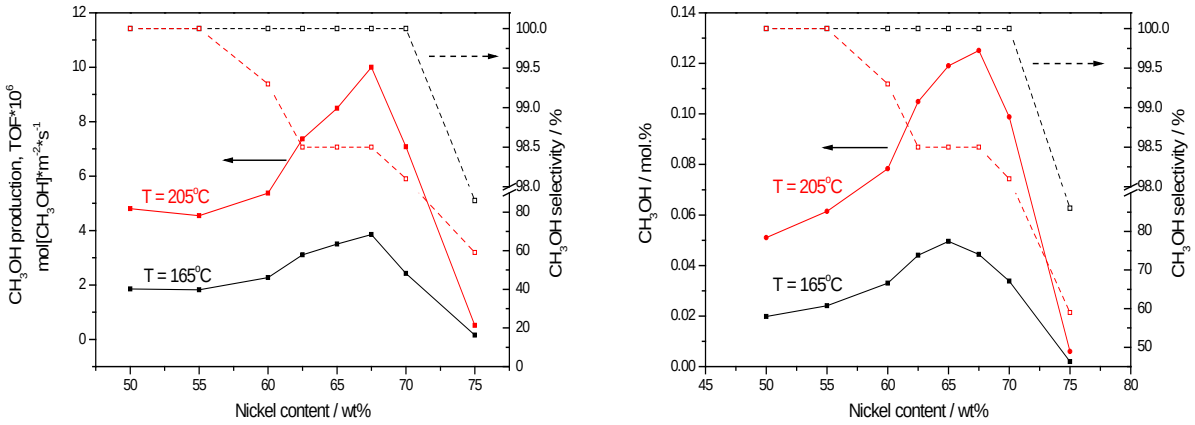

Figure 5.13. Activity of the Ni_aGa_b/SiO_2 catalysts normalized to (a) surface area of active metals and (b) molar amount of active metals.

It is well know that metallic nickel is a good methanation catalyst (37) (38). Our results could suggest that with increasing concentration of Ni in the bulk, an increasing amount of free metallic nickel (or, alternatively, other sites capable of methane production) is present on the surface of nanoparticles. On the other hand, methanol production trend suggests a correlation between the bulk composition and the number of active Ni-Ga sites on the surface, which are apparently maximized for Ni/Ga ratio of approx. 5:3.

DTF calculations have shown that the rate of methanol synthesis is dependent on oxygen binding energy (ΔE_C and ΔE_O) on the surface of the active material. In this line, step sites comprised of both Ni and Ga atoms were found to be close to optimum in terms of binding energies (27). For the Ni-Ga compositions investigated, the nature of active sites is probably not influenced by the Ni/Ga ratio; however, the relative abundance of active sites for both methanol synthesis and methane formation seems to be a function of bulk Ni-Ga composition. In other words, there **is** actually a correlation between the bulk composition and surface structure, which is reflected on selectivity in a more pronounce way than on the activity.

All the catalysts were analysed using XRF after the catalytic test. The idea was obviously to confirm that the composition of the catalyst did not change upon reduction&alloying procedure (i.e. no metal was lost during preparation). Initially, Ni and Ga standard solutions containing 1 mg/ml of metals in a 5% HNO_3 solution were bought from Sigma Aldrich. Different volumes of these solutions were mixed to obtain various Ni/Ga ratios, ranging from 40 at% to 80 at% of nickel relative to gallium. The solutions were then impregnated into the high surface area SiO_2, dried, and used for the calibration of the XRF apparatus. This procedure resulted in a straight calibration line, but all of the experimental points were significantly off. Apparently, not only relative Ni/Ga ratios but also the total loading of the metals should be in the same order of magnitude for the samples under investigation and “standard” samples, if an adequate XRF calibration should be done. This was realized later and standard custom-made Ni and Ga

solutions containing 100mg/ml of Ni and were purchased from SPECs LTD. A new calibration line was constructed, which proved that the Ni-Ga ratio in the tested catalysts actually corresponded to the targeted values. The results are summarized in figure 5.14 and table 5.4.

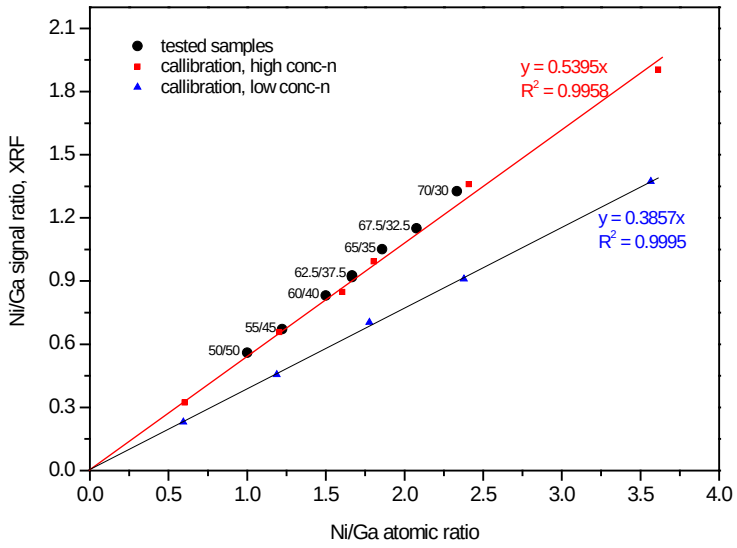

Figure 5.14. Quantification of the Ni/Ga ratio in the Ni_aGa_b/SiO_2 catalysts using X-Ray Fluorescence.

	$Ni_{50}Ga_{50}$	$Ni_{55}Ga_{45}$	$Ni_{60}Ga_{40}$	$Ni_{62.5}Ga_{32.5}$	$Ni_{65}Ga_{35}$	$Ni_{67.5}Ga_{32.5}$	$Ni_{70}Ga_{30}$	$Ni_{75}Ga_{25}$
nominal Ni content, mol%	50	55	60	62,5	65	67,5	70	75
observed Ni content, mol %	50,31	55,46	60,65	63,14	66,08	68,12	71,08	76,04

Table 5.4. Comparison of the nominal and actual compositions of the Ni_aGa_b/SiO_2 catalysts determined by XRF.

The concentration dependence of the XRF signal can be explained by the nature of fluorescence: the energy of the Ga-Kα (9.2 keV) photons emitted by the primary x-ray beam is higher than Ni-Kα (7.47keV). This implies that the fluorescent Ga-Kα photons can be used to excite some of the core Ni electrons. As the concentration of the metals in a sample increases, the probability of such an excitation goes up. Consequently, the intensity of Ni-Kα radiation will be enhanced on the expense of Ga-Kα radiation, resulting in higher Ni/Ga signal ratio observed when the total metal loading in increased (even if the Ni/Ga atomic ratio is conserved). This effect, which is briefly explained in (32) for various Fe-Ni alloys, seems to hold for the Ni-Ga system as well.

The slightly higher nickel content with respect to the nominal could be due to inaccuracy during determination of water content of the metal nitrates. The actual composition of the synthesised nanoparticles deviated at most 1,1% from the expected value.

5.3.2. Investigations into calcination effect

Earlier in chapter 5.1.1 it was suggested that the best results from catalytic point of view are obtained when a dried catalyst precursor (metal nitrates impregnated onto SiO_2) is reduced directly, skipping the calcinations step. It was concluded that the key reason was the dispersion.

In an attempt to establish a correlation between particle size and reactivity, further investigations into the influence of calcination conditions on dispersion of nanoparticles, resulting phase and catalytic activity were done. For this, the catalysts prepared in three different ways were tested and characterized:

a) calcined in stagnant air during 4 hours at 400^{o}C prior reduction

b) calcined in stagnant air during 4 hours at 700^{o}C prior reduction

c) prepared directly by reduction of nitrates.

Although the directly reduced catalyst was prepared and characterized earlier, it was decided to perform the earlier measurements again due to the following reasons:

- The XRD pattern in the figure 5.3 and a TEM picture in the figure 5.4 were obtained using SiO_2 batch that was very soon exhausted. A second SiO_2 batch, according to documentation, had similar properties (total surface area, pore size distribution, etc). However, it never allowed obtaining a clear δ-Ni_5Ga_3 diffractogram, as pointed out in the discussion of the in-situ XRD results (chapter 5.2.1). Note that the Ni_5Ga_3 samples discussed below are prepared in the fixed-bed reactor, subsequently passivated and characterized by ex-situ XRD.
- The average crystal size of the Ni-Ga nanoparticles was slightly smaller when the second batch of SiO_2 was used. Although the decrease (as concluded from the in-situ XRD experiments) was not dramatic, the idea was to exclude the effects that were possibly coming from SiO_2.

Figures 5.15 and 5.16 summarize the results of activity tests and post-reaction XRD profiles of the three catalysts prepared in a different way. XRD data was acquired after the catalysts were passivated in 1% O_2/Argon flow at room temperature; hence, partial oxidation of the Ni_5Ga_3 nanoparticles can be expected. In this line, slight oxidation is evident from a very broad peak at $2\theta = 63^o$ and $2\theta = 37^o$, which is a footprint of small nickel oxide crystallites.

Very distinct Ni_5Ga_3 profiles are observed for the calcined samples, whereas for the directly reduced catalyst some of the reflections (at $2\theta = 55^o$ and $2\theta = 71^o$) corresponding to [040] and [402] planes are not seen. This could be due to combination of at least two effects: very small particle size (below 5 nm), and a relatively weak overall signal from these crystallographic planes, as expected from reference pattern (78). For such small crystals, a lack of long range

order in certain dimensions of the crystal could be expected, which might lead to very weak (or no) signal in the diffraction pattern. However, a preferred orientation phenomenon or strong metal-support interactions could also play a role.

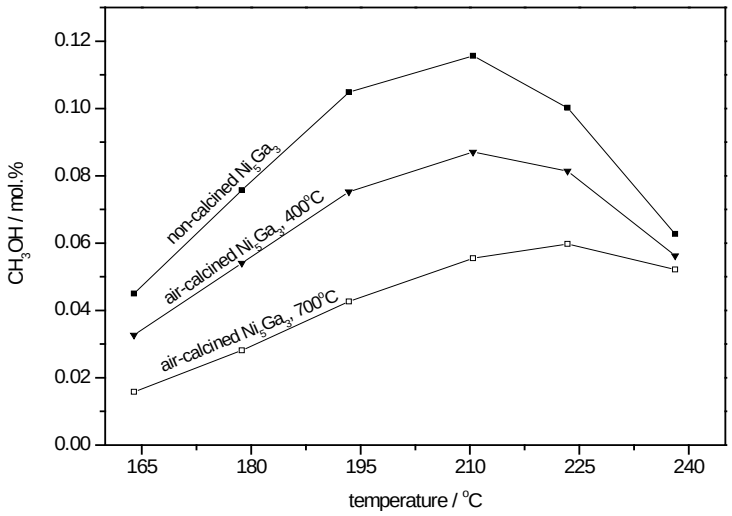

Figure 5.15. Activity dependence of a Ni_5Ga_3/SiO_2 catalyst on calcination temperature. P = 1 bar, CO_2 (75%)/ H_2 (25%) mixture.

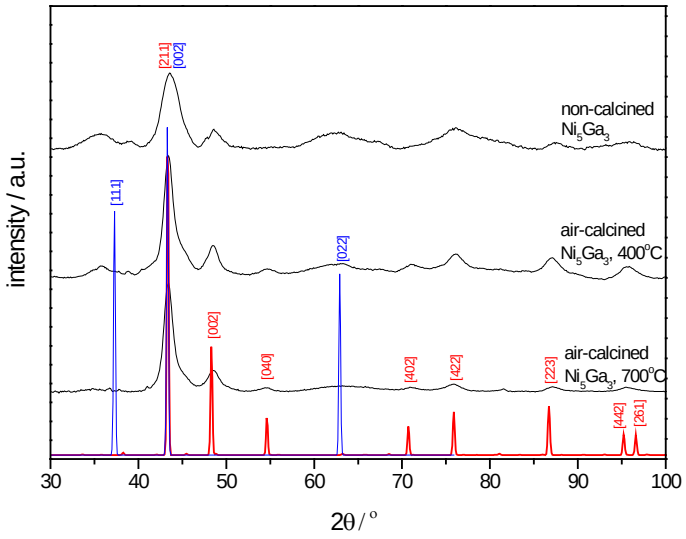

Figure 5.16. Ex-situ XRD patterns of the Ni_5Ga_3/SiO_2 catalysts.

Pre-treatment conditions have a remarkable influence on the final state of the catalytic system (figure 5.16): the catalyst calcined at 700°C exhibits the lowest activity and the largest Ni_5Ga_3

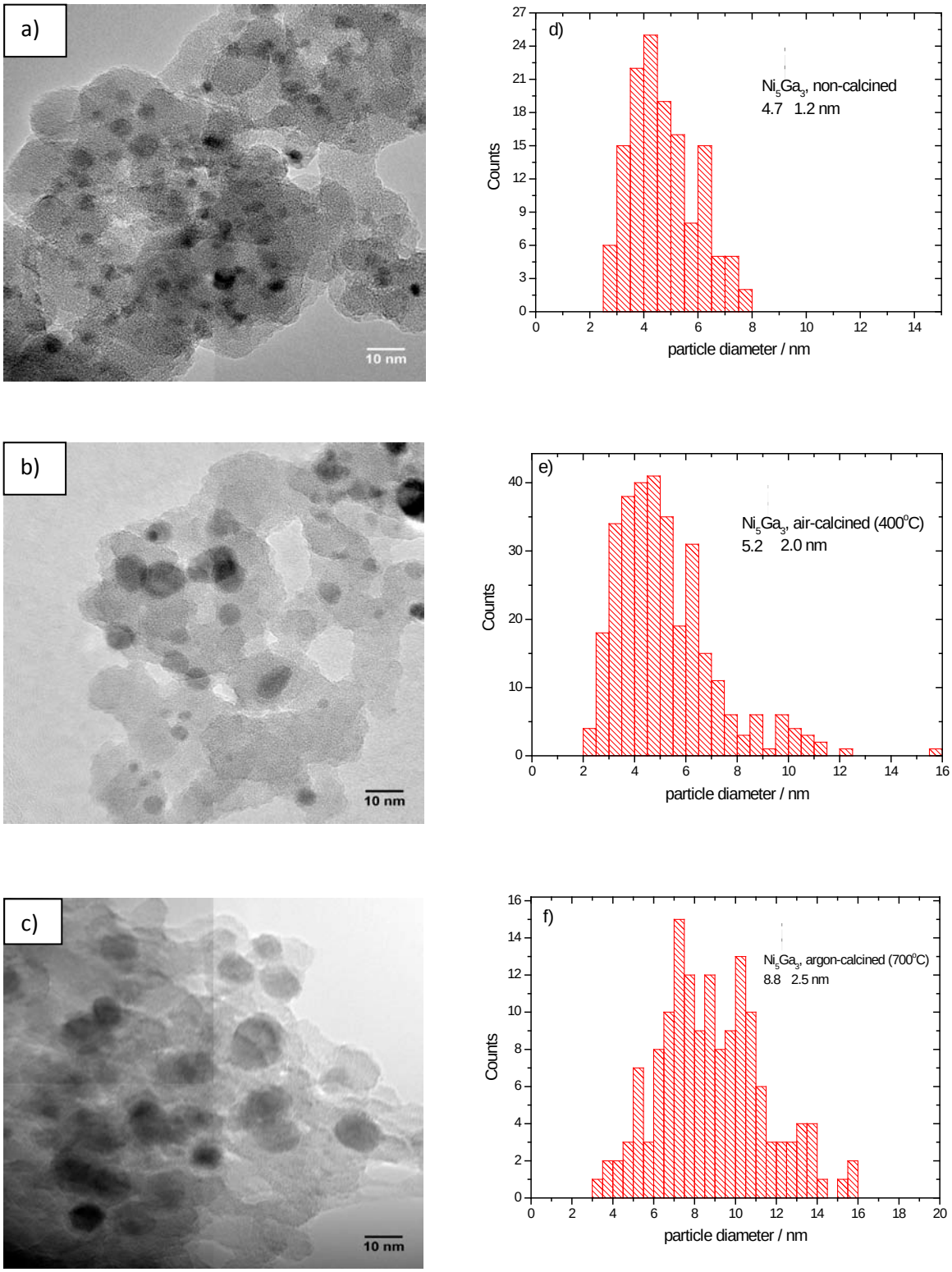

Figure 5.17. (a, b, c) post-run TEM images and (d, e, f) size distributions of non-calcined, 400°C-calcined and , 700°C-calcined Ni_5Ga_3 catalysts, respectively. Calcination was done in static air.

crystallites, as confirmed by the XRD analysis. Catalyst calcined at 400°C has an intermediate activity and particle size, while non-calcined Ni_5Ga_3 possesses the highest CH_3OH activity and consists of the smallest nanoparticles. Average particle sizes were calculated by Scherer broadening analysis of the main reflection ($2\theta = 43^o$), [211] reflection, and the data is summarized in table 5.5.

calcination temperature, °C	particle diameter, nm			
	TEM (size distribution)	TEM (surface weighted)	TEM (volume weighted)	XRD (FWHM)
N/A	4.7 ± 1.2	5.3	5.6	5.4
400	5.2 ± 2.0	6.8	7.9	5.6
700	8.8 ± 2.5	10.3	10.9	8.5

Table 5.5. Comparison of the average size of the Ni_5Ga_3 nanoparticles estimated from XRD and TEM analysis

Figure 5.17 summarizes the size distribution results obtained by TEM investigation of the catalysts, and supports the results of XRD analysis discussed earlier: pre-treatment by calcination leads to bigger Ni_5Ga_3 crystallites with broader size distribution. The average crystal size values found by XRD analysis are slightly lower, which is indicative of sintering that was apparently not taken into account appropriately by the Sherrer equation. In order to correlate the particle size with the resulting methanol yield, the specific activity of the catalyst was calculated. Activities were compared at 165°C and 180°C where the conversion is sufficiently far from equilibrium. The specific activity is defined as activity per geometric area, derived from the value of a surface weighted average diameter (63), as found by statistical analysis of TEM images according to the equation 5.2.

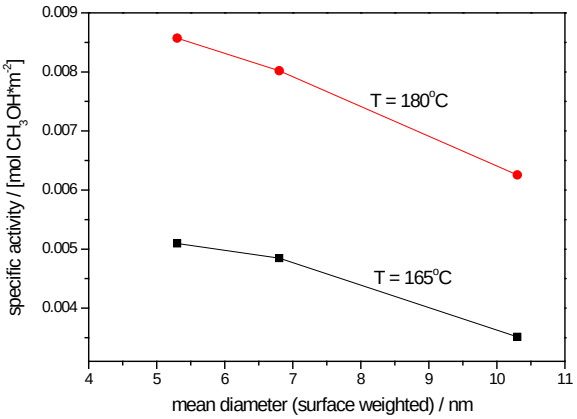

Figure 5.18. Catalytic activity towards CO_2 hydrogenation to methanol: influence of pre-treatment conditions. Feed composition: 25% CO_2 and 75% H_2; pressure: 1bar.

Figure 5.18 shows that smaller particles are more active per unit area, in accordance with the trend in activity per unit mass of Ni_5Ga_3 intermetallic nanoparticles. Here it is assumed that the

particle morphology does not change as a function of calcination temperature. In general, the fraction of undercoordinated sites (corners, kinks and step sites) on the surface is enhanced as the dimensions of the nanoparticles decrease, while the fraction of flat terraces is higher for larger particles. Previously it was suggested that methanol synthesis reaction occurs at the Ni-Ga step sites (27), which implies that the activity should increase when the particle size is scaled down.

The reason for detrimental effect of calcination on particle size and, consequently, catalytic activity is likely due to high mobility of Ni during calcination step. Previously it was shown (79) that, calcination of nickel in air leads to formation of larger NiO crystallites. Assuming that NiO crystallites serve as nucleation centers for the formation of Ni-Ga nanoparticles, avoiding the calcination step decreases the average particle size significantly and thus increases the activity

6. Deactivation of the Ni-Ga catalysts

The loss of activity over time is a common phenomenon for many reactions involving heterogeneous catalysts. Sintering, poisoning, thermal degradation, fouling, mechanical instability are only a few possible reasons causing degradation of a catalyst. In order to minimize these effects, an in-depth understanding of the processes leading to activity loss should be achieved (80). For example, the problem of severe deactivation of Pd/Al_2O_3 catalyst due to carbon deposition during selective hydrogenation of acetylene was addressed by "breaking down" the surface of palladium nanoparticles into smaller islands by adding silver (52). For group 8 transition metal catalysts, sulfur is known to be a major poison in steam reforming (81), hydrogenation (82) and Fischer-Tropsch (83) applications. For instance, blockage of the active sites of nickel catalysts leads to reduction of the activity by 3-4 orders of magnitude even at ppb levels (84). However, addition of small quantities of molybdenum and boron was shown to significantly increase the poisoning threshold (85).

Deactivation is also an issue when it comes to catalysts based on intermetallic compounds: although such catalysts were shown to be beneficial compared to conventional catalysts in a number of applications (13), (47), many of them suffer from activity loss with time. Intermetallic compounds are thought to generally possess high intrinsic stability towards sintering and decomposition due to covalent nature of binding between the metals (15); however, it is either complete dealloying (86) or alternation of surface composition (87) under reaction conditions that often causes the deactivation. A recently proposed PdGa catalyst for methanol steam reforming, was reported to lose activity due to surface dealloying and oxidation of gallium (88). Another intermetallic MSR catalyst, NiZn, is converted into a complex mixture of initial compound and metal oxides under reaction conditions (86).

In general, when it comes to intermetallic catalysts, there is always a potential for additional source of deactivation compared to monometallic catalysts – structural disintegration of the active phase. From the examples described above it is clear that many intermetallic phase are prone to decomposition under reaction conditions. Therefore, it is important to study the deactivation of the Ni_5Ga_3/SiO_2 catalyst during methanol synthesis from carbon dioxide and hydrogen. Understanding the mechanism behind activity loss is a key step to suppressing the undesired processes leading to catalyst degradataion.

The following 2 sub-chapters provide insights into the deactivation of the Ni_5Ga_3/SiO_2 catalyst in two temperature regimes; the low temperature (LTD) and high temperature deactivation (HTD). This classification is arbitrary; it is proposed with respect to the processes leading to catalysts degradation. In the LTD regime, the loss of activity seems to mainly stem from surface phenomena while in the HTD regime bulk effects such as dealloying are observed. The main

tools used to investigate the deactivation were gas chromatography, mass spectroscopy, in-situ XRD, in-situ XAS and TEM.

6.1. High temperature deactivation

6.1.1. Catalytic and XRD studies

To draw a full picture of deactivation behaviour of a catalyst, a long-term tests is always required, despite the high investments in terms of price and time (89) . In this work, due to time and equipment constrains, a different “deactivation screening” concept has been chosen. The catalysts were subjected to the so-called “accelerated ageing” test procedure, which has been adopted from (90) with some modifications. The main idea behind such tests is to facilitate the deactivation kinetics, usually by increasing the temperature. One could argue that such procedures do not truly represent the “accelerated” version of the real phenomena occurring during long-term exposure of a catalyst to reaction conditions; however, they at least provide insights into how the catalysts performance might change when it is subjected to extreme reaction conditions.

The experimental procedure consisted of several “activity testing - aging cycles”, where activity was always measured at 180°C. This temperature was chosen since methanol yield is far from equilibrium at such conditions. During the aging cycle, the catalyst was treated in the reaction mixture at temperatures higher than normal. These aging - testing cycles were repeated with increasing aging temperature from 300°C to 450°C in step of 50°C. The total flowrate was decreased by a factor of five (down to 20 ml/min) during aging, while keeping the gas composition constant. The gas mixture employed was 25% CO_2 in H_2. The graphical representation of the test is shown on figure 6.1a.

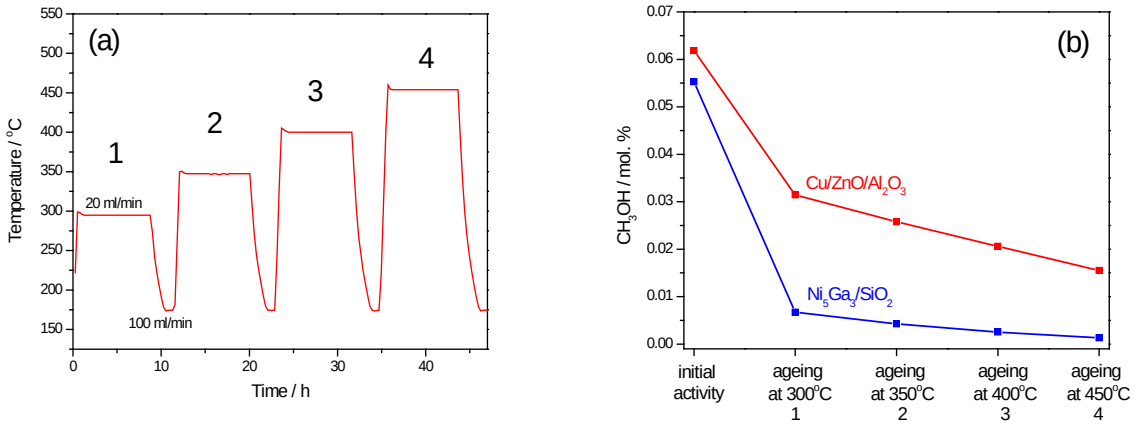

Figure 6.1. (a) Graphical representation of the accelerated ageing experiment design and (b) deactivation of $Cu/ZnO/Al_2O_3$ and Ni_5Ga_3/SiO_2 catalysts during accelerated ageing.

The detrimental effect of ageing is apparent already after the very first step (figure 6.1b). Upon keeping the catalysts in the CO_2/H_2 flow at 300C, the methanol activity of the $Cu/ZnO/Al_2O_3$ catalyst has decreased twice, while the activity of the Ni_5Ga_3/SiO_2 has dropped by an order of magnitude. Further ageing steps suggest that there is a linear deactivation behavior exhibited by both catalysts. For the $Cu/ZnO/Al_2O_3$, the reason for deactivation is most probably sintering, as suggested in (90). High mobility of copper nanoparticles at elevated temperatures leading to the loss of active surface area is a well known phenomenon. However, the stability of Ni_5Ga_3/SiO_2 catalyst under such conditions appears to be even worse. This was a rather disappointing surprise as the initial hope was that the intermetallic phase could be more stable due to slower sintering kinetics. The slow rate of agglomeration of Ni_5Ga_3 can be expected because these nanoparticles are formed at 700°C with a relatively narrow size distribution (see figure 5.17a,d)

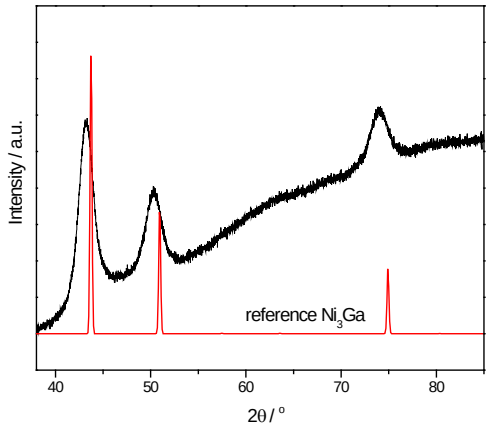

Figure 6.2. Ex-situ XRD test of the Ni_5Ga_3/SiO_2 catalyst after the accelerated ageing test.

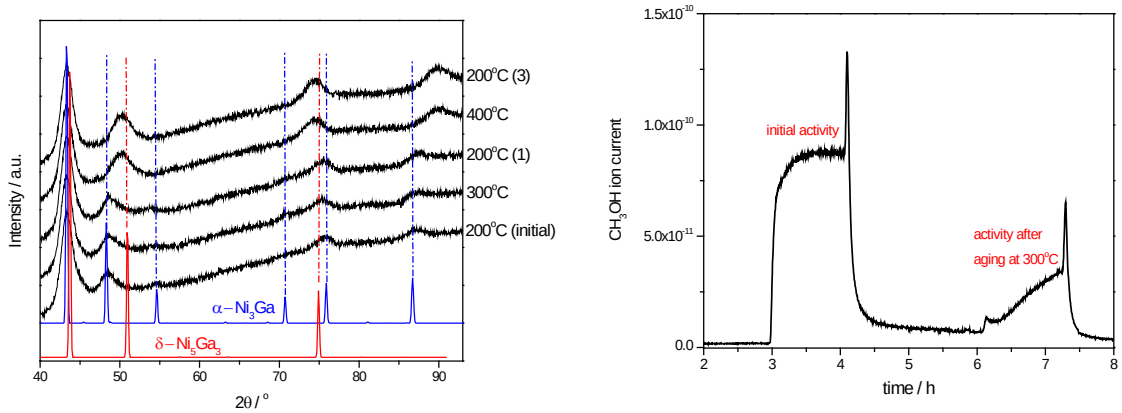

Figure 6.3. Accelerated ageing of the Ni_5Ga_3/SiO_2 catalyst in the in-situ XRD cell: (a) evolution of phases with temperature and (b) methanol production after different ageing steps.

The Ni-Ga catalyst was analyzed with the aid of XRD after the ageing experiment. From figure 6.2, dealloying of the active phase to form α`-Ni_3Ga looks like a straightforward interpretation of the catalyst deactivation. However, the onset temperature of dealloying cannot be derived from post-run XRD analysis, and therefore other mechanisms could cause the activity loss.

In order to investigate the ageing process in more detail, in-situ XRD experiments were carried out according to a protocol similar to that described above. For the sake of a more efficient utilization of the XRD time, the duration of both ageing and reaction steps were decreased to 2 hours, and the flowrate of reaction mixture was kept constant throughout the experiment. Moreover, only 2 ageing steps: at 300°C and 400°C were employed. At each step, both short (2x20 min.) and long (2x40 min) diffraction patterns were acquired. The initial diffractogram in figure 6.3a exhibits a clear pattern of a δ-Ni_5Ga_3 phase, which is actually not affected by the first ageing step, neither in terms of crystallographic phase nor particle size. At the higher temperatures, the initial phase is transformed into the more Ni-rich α`-Ni_3Ga phase, in accordance to the previous ex-situ investigations. In line with the steady state activity results presented in figure 6.1, the methanol signal followed by the mass spectroscopy (M/Z = 31) drops as a function of ageing temperature (figure 6.3b). The activity test followed by a 400°C ageing step is not shown here as the methanol signal was undetectable.

Comparison of the in-situ XRD and steady-state ageing results point towards a very interesting conclusion. Deactivation of a Ni_5Ga_3 catalyst at 300°C is very dramatic, but this is not due to bulk dealloying or sintering. The explanation could be surface phenomena, for example poisoning of the surface by the impurities in the feed, carbon (or carbonaceous species) deposition, dealloying of the surface or/and sub-surface, partial segregation of one of the components which is not detected by the XRD, etc.

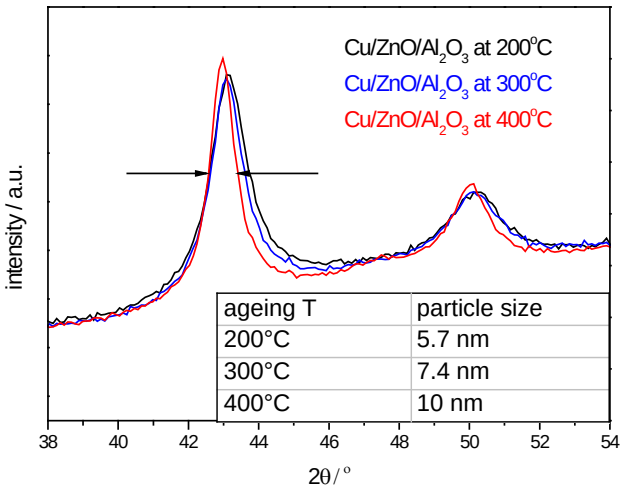

Figure 6.4. Accelerated ageing of the $Cu/ZnO/Al_2O_3$ catalysts investigated by in-situ XRD.

The main reason for deactivation in the case of $Cu/ZnO/Al_2O_3$ catalyst was, as expected, sintering of metallic copper. The corresponding in-situ XRD experiment is presented in the figure 6.4. Notice how the width of the peak at $2\theta = 43°$ is decreasing with time: the average copper particle size calculated from the Scherrer equation is estimated to increase from 5.7 nm for the fresh to 10.0 nm for the aged catalyst. In principle the more thorough analysis of the copper sintering dynamics could give a correlation between the particle size (or surface area) and methanol production, but that was beyond the scope of this study. The main conclusion at this point is that the nature of deactivation in the case of Ni_5Ga_3/SiO_2 and $Cu/ZnO/Al_2O_3$ is different.

6.1.2. Deactivation of Ni_5Ga_3/SiO_2 studied by synchrotron facilities

As pointed out above, the process of de-alloying is accomplished by formation of the Ni_3Ga phase as in-situ XRD results indicate, meaning that a certain amount of "unalloyed gallium" should be released according to the following reaction:

$$3Ni_5Ga_3 \text{ —> } 5Ni_3Ga + 4\text{"Ga"}$$

Moreover, one can not a-priori exclude that a certain fraction of nickel could be released in the unalloyed form as well. To look into the influence of accelerated ageing on the local atomic structure, similar studies were carried out by means of XAS technique. The main purpose of employing XAS method was to investigate the changes in the oxidation states of both nickel and gallium, as well as to study the dynamics of dealloying process. The observed collapse of the δ-Ni_5Ga_3 phase is most probably related to the presence of CO_2, as in pure H_2 the catalyst is very stable.

The ageing studies were performed at the SNBL (Swiss-Norwegian BeamLine) in Grenoble, which was capable of doing in-situ XRD in parallel with in-situ XAS. The wavelength of the x-ray radiation was 0.503357Å. 20 ml/min of gas was flown through the capillary filled with the catalyst.

Formation of the Ni_5Ga_3 phase followed by in-situ XAS is discussed in the previous chapter. The ageing protocol adopted here is exactly the same as the one used for the in-situ XRD studies. Figure 6.5 demonstrates how the intensities of the whitelines at the Ni and Ga K-edges respond to the changing atmosphere and temperature. Apparently, a certain fraction of gallium is getting oxidized already at 200°C, as soon as the feed gas composition is changed from pure H_2 to H_2/CO_2 mixture; this is concluded from the increased whiteline intensity. This could be the reason for the rather significant deactivation of the catalyst at 200°C (see figure 4.3). Interestingly, the whiteline intensity is almost constant upon ageing at 300^oC. Another significant jump of the whiteline is seen as a result of the ageing at 400°C, which should be interpreted as further oxidation of gallium.

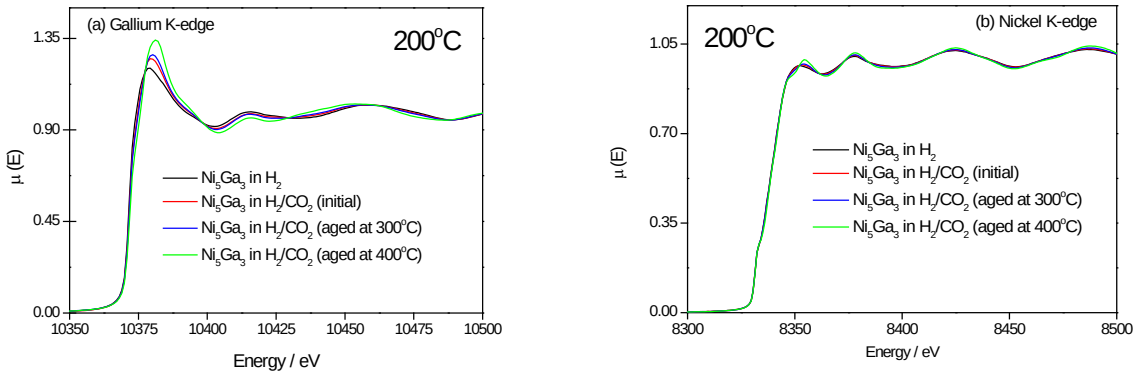

Figure 6.5. Noramlized XAS spectra recorded at the (a) gallium and (b) nickel K-edges as during accelerated ageing test.

Conversely, no remarkable changes in the normalized spectra recorded at the Ni K-edge are observed as a function of ageing temperature, implying that the oxidation state of nickel is not affected by ageing. Only at the highest temperature, a minor increase in the whiteline intensity could indicate that nickel becomes slightly oxidized.

It is more convenient to compare the Fourier transformed spectra at various ageing steps, since it helps to appreciate how the average local chemical environment around a particular absorber is changing. These data are presented on figure 6.6. Upon introducing CO_2/H_2 reaction mixture, the formation of gallium oxide is apparent form the backscattering contribution at 1.6Å (figure 6.6a): this has been earlier shown to stem from Ga-O distance in the Ga_2O_3 and $Ga(NO_3)_3$ (the presence of the nitrate can be safely excluded). Again it is clear that some oxide is formed already at 200°C, and at higher temperatures its amount is increased. At the Ni K-edge, no signs of structural changes are apparent before the last ageing step, where some indications of the long-range order occur as indicated by peaks at 3.4Å and 4.2Å.

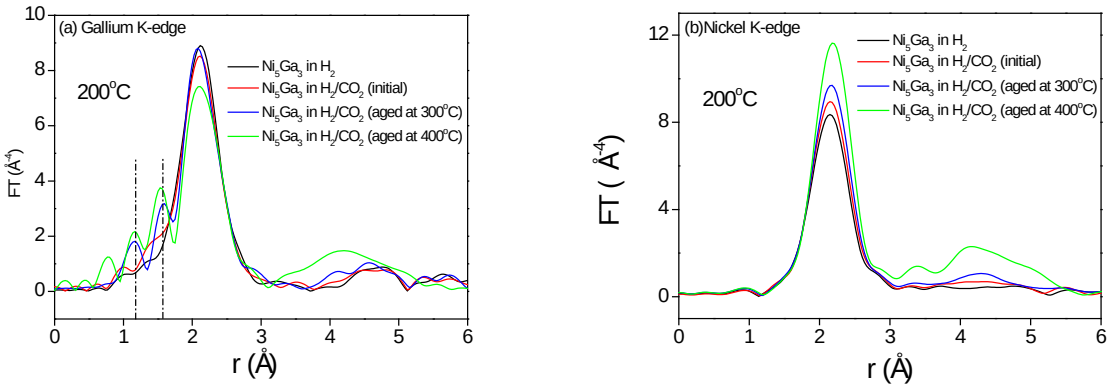

Figure 6.6. Fourier transformed EXAFS spectra recorded at the (a) gallium and (b) nickel K-edges as during accelerated ageing test.

A careful comparative look into the figure 6.6a and 6.6b reveals an interesting trend: the intensity of the main backscattering contribution at both K-edges is changing as a function of temperature. In the case of Ga, the main peak gets lower, while that of the Ni increases (green lines on both spectra). This is nicely in line with the hypothesis that gallium is being pulled out for the bulk and oxidized to gallium oxide, leaving Ni in the form of Ni_3Ga. First of all, when gallium oxide is formed (figure 6.6a), the average number of gallium atoms in the intermetallic state is diminished, causing the observed decrease of intensity. At the same time, Ni_5Ga_3 is transformed into Ni_3Ga. The later compound has a more ordered structure, as can be judged from figure 6.7, and this could explain why the intensity of the main backscattering contribution is enhanced.

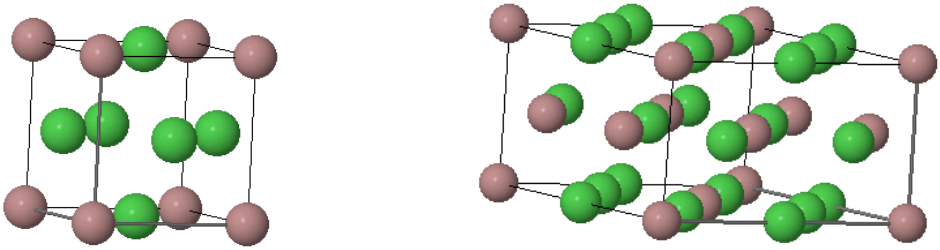

Figure 6.7. An *fcc* structure of the Ni_3Ga phase (left) and a more complex *orthorhombic* structure of the Ni_5Ga_3 phase (right) (40). Green spheres – nickel atoms, grey spheres – gallium atoms.

Unfortunately, Quick EXAFS spectra were not acquired during the heating and cooling steps in between long EXAFS acquisitions at the isothermal conditions. Although it was possible to do both in-situ XRD and in-situ XAS in parallel, only one of the two had to be selected during heating/cooling cycles due to technical limitations. It was decided to try in-situ XRD which turned out to produce diffractograms of rather low resolution that could not be further used. Otherwise, it would be interesting to look at the changes (especially at the Ga K-edge) of the normalized and FT EXAFS spectra as a function of time. This might for instance have provided a correlation between the catalyst deactivation at 200°C and the extent of Ga oxidation.

The positive thing is that at the isothermal conditions, both in-situ XRD and in-situ XAS data were collected. This time the signal to noise ratio of the diffractograms was enhanced due to longer acquisition times. In this way, a deactivation model derived from XAS data could be directly validated with the diffraction data. Figure 6.8 shows the complementary in-situ XRD patterns. The 2θ values were re-calculated using Bragg equation, for the sake of easier comparison with the data collected using Cu K-alpha radiation. The results are very consistent with those presented in figure 6.3a: ageing at 300°C does not have any detectable effect on the bulk crystal structure while ageing at 400°C leads to phase transformation.

Gallium oxide has never been detected with the XRD, implying that it has an amorphous nature. An attempt has been once made to force the crystallization of Ga_2O_3 after the total deactivation of the catalyst. For this, the spent catalyst was calcined in argon flow at 700°C during 12 hours;

however, the oxide phase did not show up. The only technique used in this work that provided evidence of Ga_2O_3 formation was therefore EXAFS.

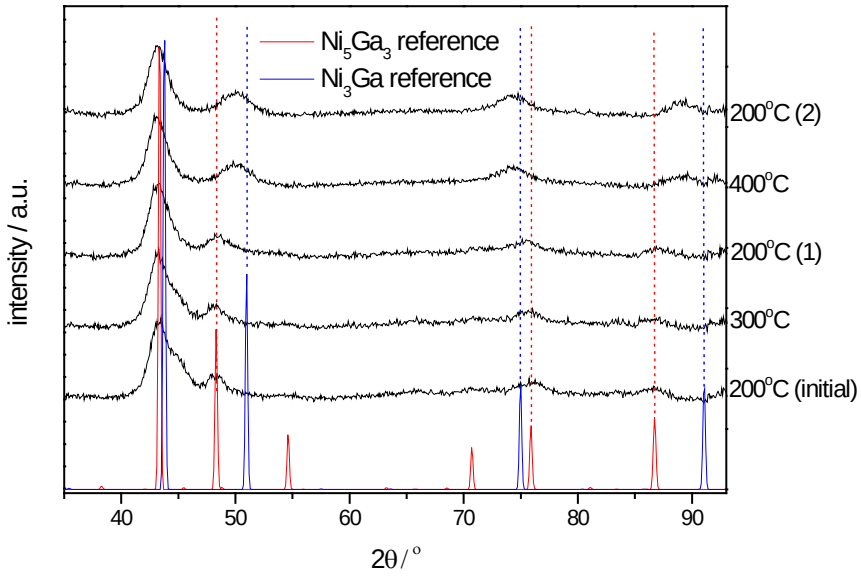

Figure 6.8. Accelerated ageing of the Ni_5Ga_3/SiO_2 catalyst investigated by the synchrotron X-ray radiation (SNBL, Grenoble).

6.1.3. Reactivation of the aged catalyst

When a substantial amount of data had been collected on deactivation of the Ni_5Ga_3 catalyst, the obvious question arose whether it was possible to regenerate the catalyst after ageing. If the dealloying is promoted by high temperatures in the CO_2/H_2 feed gas (400°C), is it then a reversible process? To answer this question another experiment was designed, which was basically a modified and extended version of an accelerated ageing test. The experiment consisted of four steps (I, II, III and IV), and each step was made of an "ageing (1)-testing (2)-regeneration (3)-testing (4)" cycle, as shown in figure 6.9. A constant flow of 100 ml/min of a stoichiometric CO_2/H_2 mixture was used for ageing and testing, while regeneration was accomplished in a pure H_2 flow. Compared to the rapid ageing test described in chapter 6.1.1, the duration of ageing steps were decreased from 8 to 2 hours. But the main difference is the regeneration (3) procedure that was introduced in the current version of the experiment, which was followed by another activity test (4). The regeneration temperature was always the same as that of the ageing, in order to investigate the reversibility of the processes leading to loss of activity.

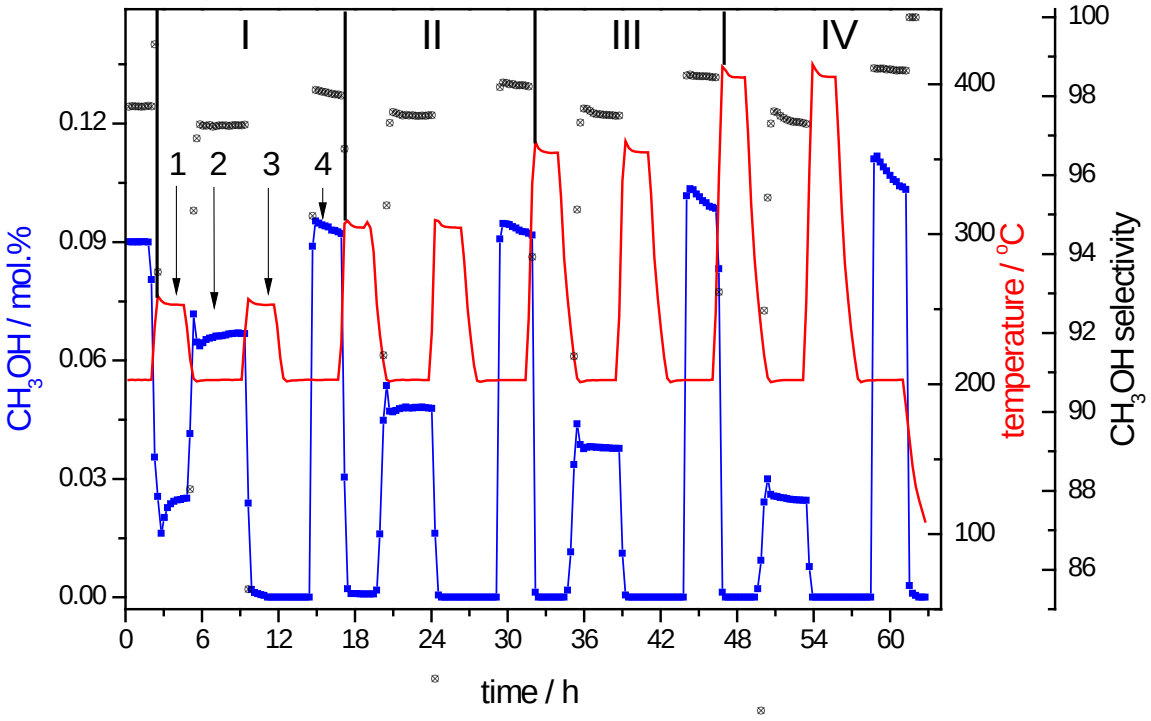

Figure 6.9. Extended accelerated ageing experiment. Reaction mixture: CO_2 (25%) and H_2 (25%)

The very first 2 hours of the experiment are carried out on a catalyst that had been already tested for 20 hours, which explains a very stable reading of the methanol signal. In the present case, this will be regarded as a measure of the initial methanol production rate (although in some of the later tests the concept of initial activity is different: it refers to the methanol production rate in the first hour after catalyst preparation). After ageing at 250°C, roughly one third of the initial activity was lost; however, regeneration enabled to bring the methanol production rate fully back to initial level. Ageing at 300°C diminishes half of the methanol, but again regeneration successfully restored the catalyst. A similar behaviour is observed at the steps III and IV.

Interestingly, there seems to be a linear correlation between the ageing temperature and the level of activity loss. However, the decrease of the rate of methanol production after ageing is significantly lower than that observed in the figure 6.1b (compare for instance the 7-fold activity loss at 300°C and only a 2-fold drop observed here). This should be due to shorter ageing time, which probably also correlates with the level of deactivation (although not necessarily in a linear fashion). It should also be noted that the methanol production rate immediately after the regeneration is slightly higher than the initial. It actually has a positive correlation with the regeneration temperature, since the activity after 400°C regeneration is the highest.

The behaviour of the catalyst in terms of selectivity deserves a separate discussion. First of all, the selectivity is roughly the same irrespective of which testing step is considered, suggesting

that the structure of the surface is more or less similar throughout the experiment. This is to a certain extent counterintuitive, as it has earlier been shown with the aid of in-situ XRD and in-situ XAS techniques that the Ni_5Ga_3 phase is disintegrated and converted to Ni_3Ga. The later one, when synthesised directly from metal nitrates as a Ni_3Ga/SiO_2 catalyst, bears a lot of similarities with metallic nickel in terms of syngas conversion: figure 4.4 shows that it is highly selective towards methane from CO_2/H_2 feed and rather poor for methanol production. This implies that after ageing at 400°C, the catalyst should be expected to lose its selectivity to methanol, but apparently it *does not*. The explanation could be that the surface structures of a directly prepared Ni_3Ga/SiO_2 catalyst, and the one formed due to ageing are grossly different. Gallium oxide has a very negative $dG_f°$ value, -998.3 kJ/mol (64); this could suggest segregation and at least partial oxidation of gallium upon dealloying. Segregated gallium might cover the surface of the nanoparticles, thus blocking the sites that would otherwise be very active towards methanation. The reversibility of the deactivation process is another indication that the oxidized gallium is preserved in the close vicinity to the nanoparticles, most probably covering them. Nickel oxide has a significantly less negative $dG_f°$ value, -211.7 kJ/mol (64), and therefore the oxidation potential of CO_2 at elevated temperatures might not be enough to pull out Ni from the Ni-Ga intermetallic phases. Although in-situ XRD suggests that the Ni_5Ga_3 phase is dealloyed, there could still be a certain fraction methanol-active sites on the surface that survive ageing. However, the catalyst has to be investigated using *in-situ* surface sensitive techniques in order to shed more light into this interesting phenomenon.

The selectivity variations under test conditions will be discussed in more details in the following sub-chapter. The by-products detected by the GC are carbon monoxide, dimethyl ether and methane. The relative amount of these substances is rather constant between various testing steps, which is another strong evidence that the same active sites are present irrespective of the state of the catalyst: it looks like only the amount of these sites is affected as the temperature is increased.

6.2. Low temperature deactivation

6.2.1. Long term stability

With the experiment described above, one can most certainly exclude that deactivation mechanism is irreversible. Since it is more interesting from practical point of view to look into the deactivation under normal operating conditions rather than extreme, another test was performed as demonstrated in the figure 6.10. Here, methanol is synthesised at 200°C for 20 hours, then the catalyst is flushed with argon during 8 hours and finally regenerated at 250°C. This procedure is repeated once again to see if the catalysts performance has changed with time. Thus, the catalyst was exposed to reaction conditions three times. Trace amounts of the products

observed during flushing steps are not shown here in order to keep the figure "cleaner". The idea behind introducing the flushing step was to remove all traces of reaction products and feed gas components before the regeneration experiment. This would enable one to see if carbonaceous species (possibly present) on the catalysts surface are converted to methane during the regeneration in H_2 flow, without risking that the gaseous residuals are hydrogenated. Unfortunately, in this particular experiment the quantification of the amount of CH_4 produced during regeneration was not possible, so this question was addressed in a separate experiment discussed further in this chapter.

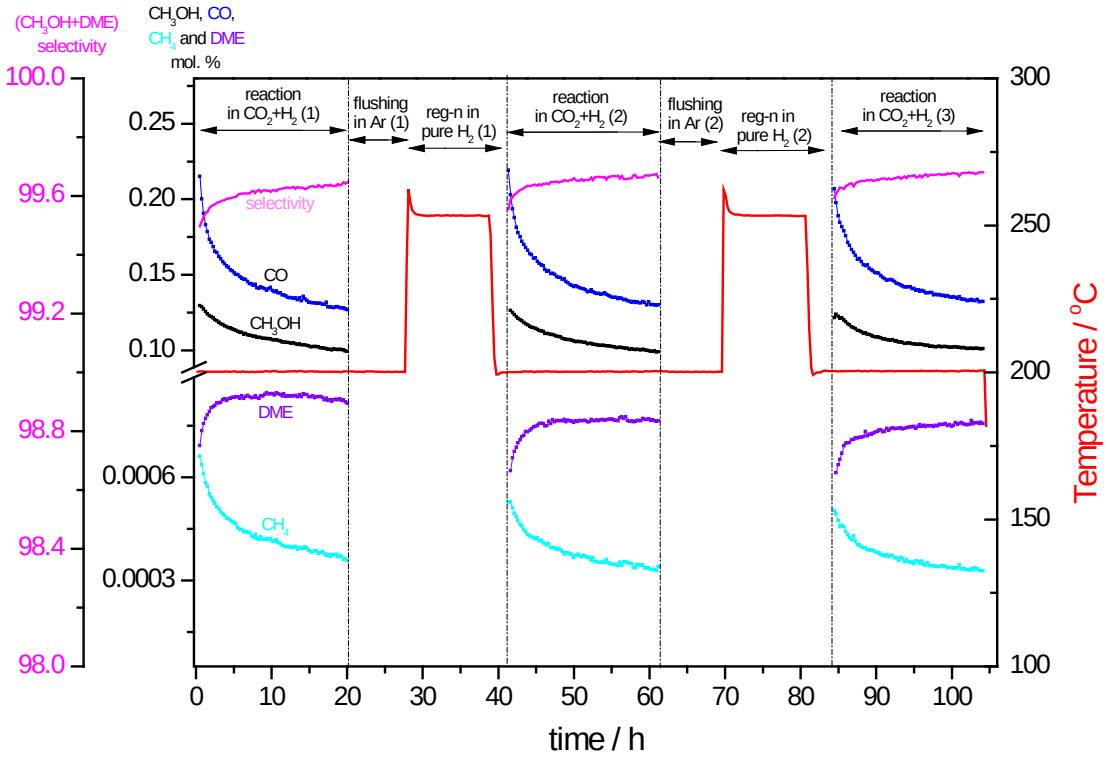

Figure 6.10. Methanol synthesis experiment followed by flushing and further regeneration of the catalyst. Reaction conditions: 25% CO_2 in H_2, atmospheric pressure.

First of all, the rate of methanol production is decreasing rapidly within several hours. The rate of deactivation is slowing down with time, and within 20 hours the level of CH_3OH is almost stabilized accomplished by the loss of approx. 25% of the initial activity. However, regeneration at 250°C leads to complete reactivation of the catalyst: almost exactly the same initial activity and deactivation trend are observed as for the fresh catalyst. This procedure was repeated for the 3rd time to get an even stronger evidence that deactivation phenomenon was fully reversible. Notably, not only methanol activity but the levels of CO, CH_4 and DME production were restored after hydrogen treatment of the catalyst. Moreover, the activity of the Ni_5Ga_3/SiO_2 catalyst towards these by-products as a function of time is also very similar after the

regeneration. The minor difference between the reaction steps is that the amounts of methane and dimethyl ether are slightly lowered.

It should be noted that deactivation profiles of CO and CH_4 follow that of methanol, while the rate of DME production approaches a constant level with time after the initial activation period. This could suggest that CH_3OH, CO and CH_4 are produced on either the same or similar catalytic sites. DME is most probably synthesised from methanol on the surface of SiO_2, as this reaction is known to take place on the acidic sites; these sites could be present on the surface of SiO_2 as well (91). Assuming that catalytic properties of SiO_2 are not affected by the reaction time, the rate of DME production should be stable as long as sufficient amount of CO_2 is converted to methanol. This is what figure 6.10 clearly illustrates.

But is there a quantitative interplay between the amounts of CH_3OH, CO and CH_4 produced? To answer this question, the ratios between these components as a function of time on stream were plotted in the figure 6.11. Such analysis reveals a few interesting trends. The ratio between CO and methanol is stabilized within 2-3 hours, indicating that the surface of Ni-Ga nanoparticles reaches a steady state. Apparently, the amount of rWGS active sites on the surface of the fresh catalyst is greater than the number of methanol-active sites. Another interpretation could be that the same sites are active towards methanol and CO synthesis from CO_2 and H_2; however, the surface gets modified in a way that rWGS activity is decreased with time.

On the other hand, the ratio between CO and CH_4 is constant from the very beginning of the experiment, especially when the 2^{nd} and the 3^{rd} reaction cycles are considered (dashed and dotted blue lines, figure 6.11). This implies that methane production rate directly follows the rate of rWGS reaction. The later argument is supported by (38), where it is proposed that the presence of H_2 facilitates the formation of CO on a Ni/SiO_2 catalyst, followed by dissociation of carbon monoxide into atomic carbon and oxygen. Carbon, in turn, is further hydrogenated to form methane. However, in the present case the amount of CO is 400 times greater than the amount of CH_4, which is a consequence (and at the same time yet another evidence) of the huge difference between pure metallic nickel and Ni-Ga surface from catalytic point of view. Otherwise, for a Ni/SiO_2 catalyst, a much higher conversion of CO into methane would be expected at this temperature (37).

Atomic oxygen from CO dissociation, as well as water produced in rWGS reaction, could both contribute to the partial oxidation (or even segregation) of gallium. The later phenomenon has been proposed analysing the x-ray absorption data (figure 6.5, section 6.1.2). However, XAS is a bulk technique and therefore one cannot exclude that catalytically inactive gallium atoms (the so-called “spectators”) are primarily oxidized.

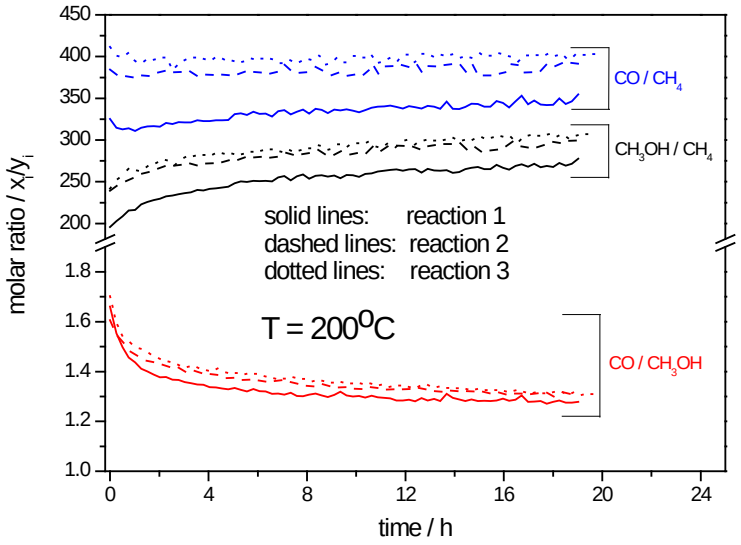

Figure 6.11. The ratios between the reaction products as a function of time during a 20hour test. Reaction conditions: 25% CO_2 in H_2, atmospheric pressure.

6.2.2. Effect of CO

Initially, DFT calculations were made for CO hydrogenation, but apparently carbon monoxide is a really unwanted compound in this reaction. The effect of addition of 5% CO into a CO_2/H_2 mixture is illustrated in two separate experiments, presented in the figure 6.12. In the first experiment, the partial pressure of CO_2 was varied by blending the CO_2/H_2 mixture with a subsequently decreasing amount of argon, keeping the flowrate of H_2 (50ml/min) and the total flow (100ml/min) constant (red points, figure 6.11) until a 50%CO_2/50%H_2 composition was achieved. Afterwards, the CO_2 partial pressure was decreased back to the initial level of 0.35bar by diluting the CO_2/H_2 mixture with carbon monoxide.

It is remarkable that for a wide range of CO_2 partial pressures the rate of methanol production is constant; so is the rate of the rWGS reaction. This implies that the total flowrate of the gas mixture could be decreased, without compromising the amount of methanol synthesized. On the other hand, the detrimental effect of CO is very pronounced: introducing 2% of CO kills approx. 35% of the activity. Increasing the concentration of CO further deteriorates the catalysts performance until almost no methanol is observed at 15% of CO. This is a very strong indication of the CO poisoning of the catalysts surface.

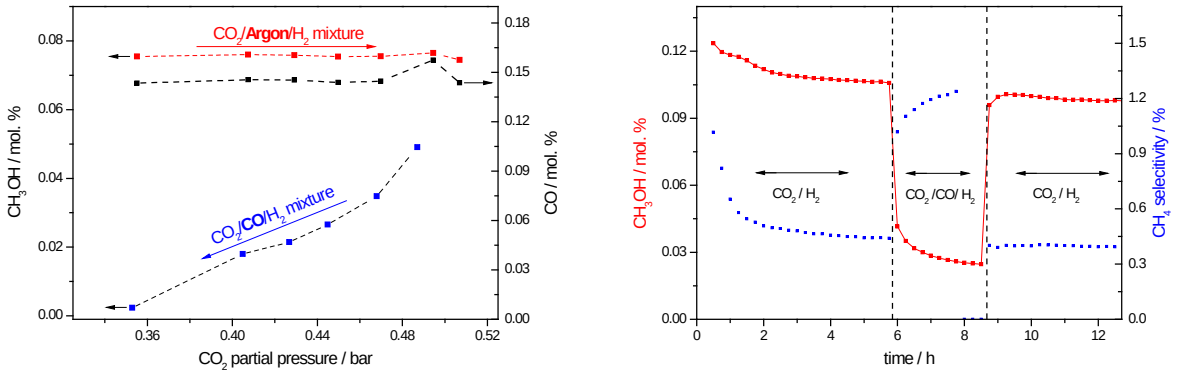

Figure 6.12. (a) Methanol production as a function of CO_2 partial pressure and reaction mixture composition. Total flowrate: 100 ml/min, T = 200°C, atmospheric pressure. (b) Methanol activity and methane selectivity of Ni_5Ga_3/SiO_2 catalyst as a function of reaction mixture composition.

In another test, a long experiment was intentionally ”interrupted” by co-feeding of 5% CO into a stoichiometric CO_2/H_2 mixture. This was immediately followed by a sharp drop of the methanol signal, and an increase of CH_4 production. As soon co-feeding of CO was stopped, the ”normal” rate of CH_3OH synthesis as well as methane selectivity was restored. The direct correlation between the presence of CO and the CH_4 production rate is yet another evidence that methanation reaction is followed by rWGS during the CO_2 hydrogentation to methanol.

6.2.3. Carbon formation under normal operation conditions

Just a reminder: under normal operation conditions, a CO_2 hydrogenation test utilizing a ($25\%CO_2$ + $75\%H_2$) mixture at atmospheric pressure and 200°C and a total flowrate of 100ml/min should be understood. As discussed above, a significant amount of CO and CH_4 is produced within 20 hours. It was argued that CO is partially split into atomic oxygen and carbon, and the later is hydrogenated to methane. But until now, it was not possible to tell if all atomic carbon is converted to CH_4 under reaction conditions: one could speculate that there could be a carbon built-up responsible for the observed deactivation of the catalyst. Earlier it has been observed for supported nickel catalysts, that surface carbide was formed under reaction conditions similar to those discussed here (80)

To check if this was the case, an experiment comprising of 20-hour methanol synthesis, 10 hour argon flushing and finally regeneration in H_2 was performed (until methane level went below the detection limit of the GC). The regeneration process was performed at 300°C to facilitate the process. Figure 6.13 shows the methane evolution profile: upon regeneration, a significant amount of methane is released and its level exponentially drops with time. Integrating the area under the methane evolution curve show that 0.526 ml of CH_4 are formed. This number allows calculating the carbon coverage under the following assumptions:

- catalyst consists of spherical Ni_5Ga_3 nanoparticles with the diameter of 5.5nm (this is consistent with XRD and TEM data)
- carbon is adsorbed in an atomic sp^2 state (atomic radius 73 pm)
- all carbon is hydrogenated off the surface to form methane during regeneration
- the stoichiometry of the surface is similar to that of the bulk at 200°C

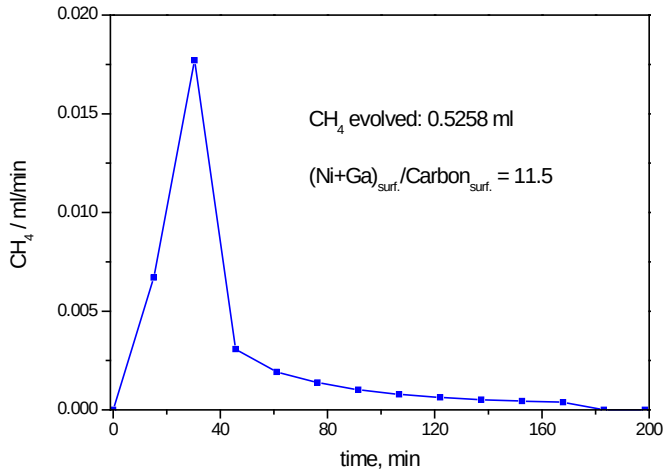

Figure 6.13. Methane evolution upon regeneration of the Ni_5Ga_3/SiO_2 catalyst. T = 300°C, pure H_2 flow.

Provided that these assumptions hold, an atomic coverage of 8.7% is calculated. Assuming that in the present case the active sites are preferentially blocked by carbon, the accumulation of carbon could account for the catalyst deactivation.

In an attempt to see if an appreciable amount of carbon is formed on the surface, a model Ni_5Ga_3 catalyst supported on 200 nm SiO_2 nanospheres was prepared (the so-called Stoeber silica). The nanospheres with a controlled size were synthesised following a simple sol-gel process, described in (92). The idea was to have the Ni_5Ga_3 nanoparticles on a low surface area support, which would be more suitable for electron microscopy investigations, especially high resolution TEM. In this way, the chance of observing surface carbon would be higher.

The $Ni_5Ga_3/SiO_2^{(200nm)}$ catalyst was prepared according to a conventional incipient wetness impregnation protocol, followed by drying and reduction in the flow of pure hydrogen. After that, the catalyst was subjected to CO_2/H_2 mixture for 20 hours, which was supposed to leave a substantial amount of carbon on the surface. Finally, the system was cooled down to RT and passivated in a 1% O_2/Argon flow before TEM analysis. The new catalyst contained the same amount of metals as the one prepared using high surface area SiO_2. Figure 6.14 confirms that utilizing a low surface area SiO_2 support does not change the catalysts behavior in terms of deactivation: the activity is decreased continuously as a function of time. Only the overall

methanol production rate is lower than usual, which is explained by the relatively bad dispersion as judged from statistical TEM analysis (figure 6.15a).

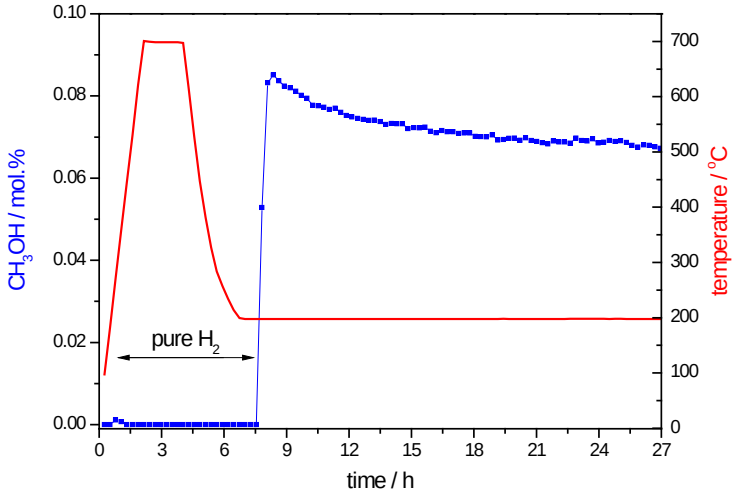

Figure 6.15. Catalytic activity of the Ni_5Ga_3 catalyst supported on SiO_2 nanospheres.

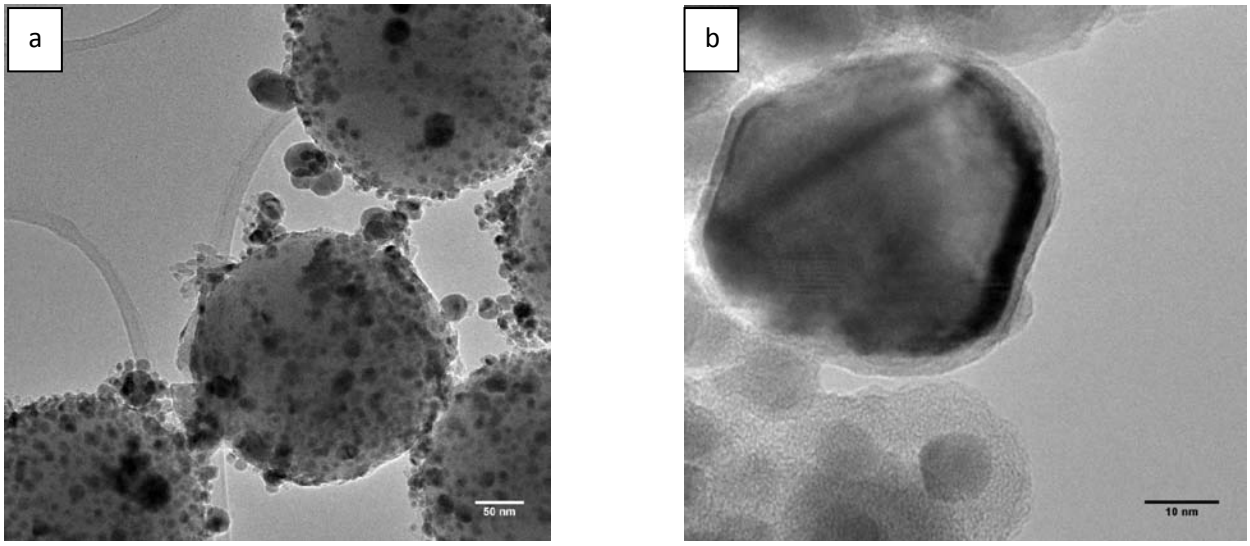

Figure 6.15. (a) TEM and (b) HRTEM images of the Ni_5Ga_3 catalyst supported on SiO_2 nanospheres.

A few HRTEM images were acquired along with conventional ones. A representative nanoparticle is shown in figure 6.15b. First, lattice fringes are seen, proving that the material under investigation is crystalline. Second, the determined distance between the lattice fringes, which is approx. 2.5A, correlates well with the [021] and [220] planes of the δ-Ni_5Ga_3 phase. However, the presence of deposited carbon - the main target of the investigation - is not directly evident. An amorphous, 1-2 nm thick layer covering the nanoparticle could easily be an oxide, formed during passivation. On the other hand, the amount of deposited carbon is way below a

monolayer (remember the 8,7% coverage calculated above), therefore it is probably not surprising why TEM could not unambiguously reveal its presence.

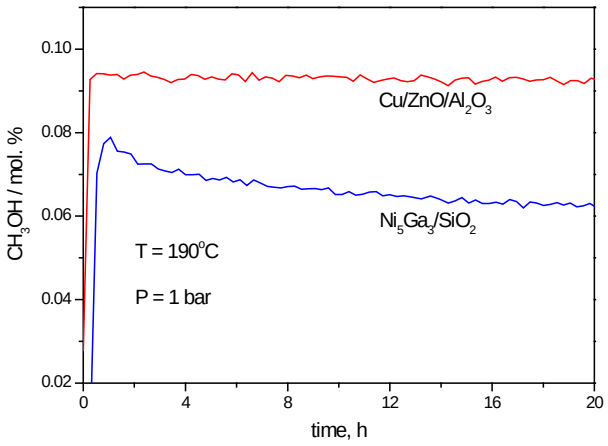

Figure 6.16. Deactivation behavior of Ni_5Ga_3/SiO_2 and $Cu/ZnO/Al_2O_3$ catalysts.

It is always nice to compare a new catalyst with the one that is well studied. In the present case, the long-term stability of the Ni-Ga catalyst is compared to that of the $Cu/ZnO/Al_2O_3$, as demonstrated in figure 6.16. Both tests were performed at 190°C which is not completely consistent with the temperature employed in the previous tests (200°C). Nevertheless, this does not change the overall discussions. The main conclusion is a high stability of the copper based catalyst, which is not prone to either carbon deposition.

6.2.4. Proposed mechanism of a low temperature deactivation

To sum up the picture of low temperature deactivation, the following schematic illustration of the various processes occurring under reaction conditions is given in the figure 6.17:

CO_2 is converted either to methanol due to direct hydrogenation or CO in a reverse water gas shift reaction; CO is mainly released as a gas-phase product but partly dissociated to C and O. Most probably, the rWGS reaction takes place on certain Ni-Ga surface sites: if it was produced on pure Ni then the rate of CH_4 formation would be much higher (37). However, the Ni-Ga surface is apparently not completely inactive for the cleavage of C-O bond.

It is well known that Cu catalyst is highly selective to methanol (>99.9%) (12). The high selectivity has been explained with the aid of DFT calculations in terms of optimal binding energy of reaction intermediates: the cleavage of C-O bond is energetically unfavourable reaction on the Cu surface (93). Nevertheless, certain amount of hydrocarbons is present in the reaction mixture under industrial reaction conditions (2). In the case of Ni-Ga, the energy

pathway for CO_2 hydrogenation to methanol is still favourable, but the dissociation pathway leading to CO and then CH_4 formation is apparently more probable compared to copper.

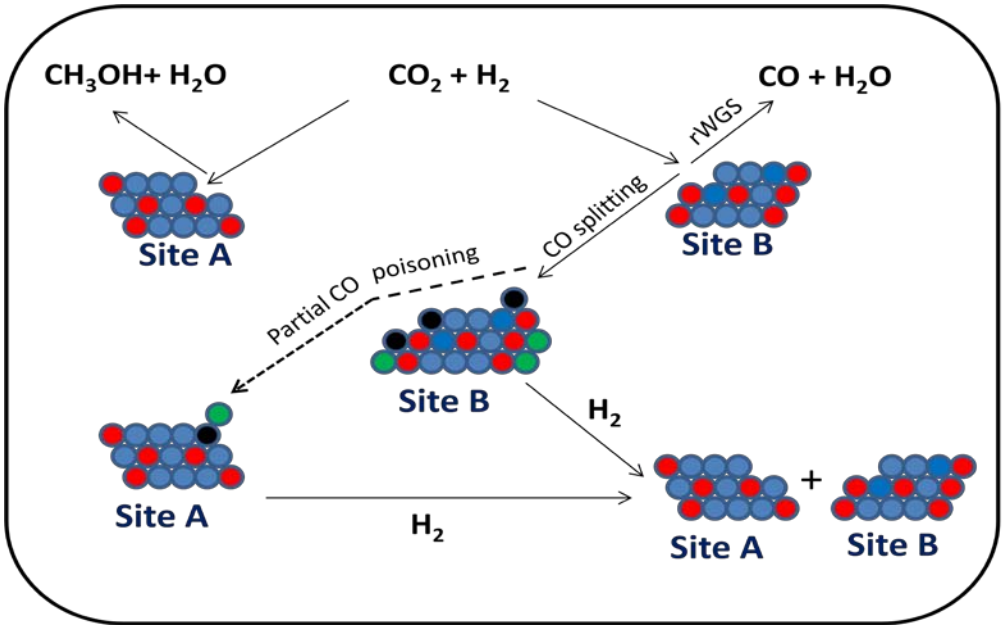

Figure 6.17. Proposed mechanism of the low temperature deactivation of the Ni-Ga catalysts. Red spheres – gallium atoms, blue spheres – nickel atoms, black spheres – carbon atoms, green spheres – oxygen atoms.

7. Conclusions, summary and outlook

The central topic of this work has been synthesis, characterization and optimization of novel Ni-Ga based catalysts for hydrogenation of CO_2 to methanol. The overall goal was to find a material that could be used as a low temperature (and low pressure) methanol synthesis catalyst. This is required for small scale delocalized methanol production sites, where one cannot afford to install expensive and energy demanding compression units.

The work was initialized by theoretical screening of a large set of binary metallic compounds, or, to be more precise, their surface geometries. The screening was performed using DFT calculations according to the algorithm briefly described in chapter 1.3, and suggested that certain bimetallic systems were promising catalysts for the methanol synthesis reaction. DFT calculations, in general, rely on several simplifying assumption, such as ignoring metal-support interactions or modelling extended surfaces which might look different from the real ones (94). These assumptions may or may not be applicable to a particular system, and experimental work involving model and real catalysts is always needed to see how far is the theory from reality. Therefore, the absolute values obtained from DFT calculations should be considered rather critically. However, DFT has been shown to be good in predicting the *trends* in reactivity, and pinpointing the catalyst that have the highest chance of being optimal for a particular reaction. And this is exactly how Ni-Ga has come into scene.

Although initial calculations were made assuming hydrogenation of CO into methanol, it has been experimentally observed that the catalyst is much more active towards hydrogenation of CO_2. Co-feeding of even small amounts of CO has a deteriorate influence on activity, which is restored after CO is removed from the feed. This suggests that the surface gets reversibly poisoned by CO: carbon monoxide bind relatively strongly, and at the same time the activation barrier required for hydrogenation of adsorbed CO is too high on the Ni-Ga surface. On the other hand, the binding energy of CO_2 is apparently lower and therefore poisoning of the active sites by carbon dioxide is not observed. These early finding served as an input for an improved DFT model that was utilized to describe conversion of CO_2 to methanol. The new calculations resulted in a volcano plot shown in the figure 1.1. The real TOF values were calculated based on the knowledge of the average sizes of copper and Ni-Ga nanoparticles in the corresponding catalysts. The calculations were performed assuming that:

- Nanoparticles are spherical
- All surface atoms are catalytically active, i.e. turnover numbers per surface atom are estimated

The resulting plot for the $Cu/ZnO/Al_2O_3$, $NiGa/SiO_2$ and Ni_5Ga_3/SiO_2 are presented in figure 7.1:

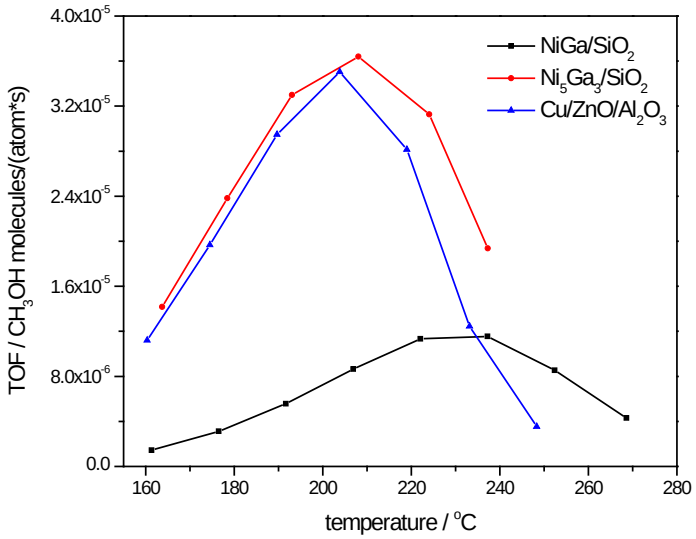

Figure 7.1. TOF values estimated from experimental methanol production rates and average sizes of Ni-Ga and Cu crystallites.

One can immediately see that the discrepancy between the DFT calculated and real TOF values is very significant (approximately four orders of magnitude). This cannot be accounted for by an intrinsic error of DFT calculations, which is close to 20-30 eV when estimating the adsorption and transition state energies (95). At this point, additional calculations are being performed assuming different geometries of the active sites.

But even though the theory predictions were not completely correct at the first place, they enabled to choose the right candidate for investigations. Indeed, for an optimal catalyst, which is a SiO_2 supported Ni-Ga intermetallic compound prepared from a solution of nitrates containing 5:3 molar ratio of Ni:Ga, the intrinsic activity (methanol production rate per active surface area) is comparable to that of highly optimised $Cu/ZnO/Al_2O_3$. Even more remarkably, CO-free selectivity of the catalyst is very high: the total selectivity towards methanol and dimethyl ether (both resulting from hydrogenation of CO_2) is higher than 99% at the conditions close to thermodynamic equilibrium (figure 5.2), implying that the selectivity to methane (due to splitting of CO molecules) is less than 1%. This is rather counterintuitive for a bimetallic compound containing up to two thirds of nickel (in moles), as nickel is a famous for its methanation activity (see figure 4.4**)**. Clearly, alloying with gallium changes the catalytic behaviour of nickel dramatically.

As a result of initial optimization work, a Ni_5Ga_3/SiO_2 catalyst was chosen as a subject for further investigations. In-situ XAS and in-situ XRD studies provided a strong evidence that formation of the desired phase goes through decomposition of metal nitrates to oxides, followed by further reduction of oxides accomplished by alloying. In fact, nickel oxide species seem to act as “immobile” centres where alloying takes place: gallium oxide only starts to reduce after a

certain amount of metallic nickel is formed. Reduction of Ga_2O_3, in other words, is triggered by the reduction of NiO, probably thanks to formation of a very active nickel hydride that has a reduction potential high enough to convert gallium oxide into gallium. Indeed, it has been shown that reducibility of silica supported Ga_2O_3 is limited at the temperatures as high as 500°C, leading to only partial reduction of gallium ($Ga^{\delta+}$ formed, $\delta<2$) (96). In the present case, however, most of the gallium is already alloyed at 500°C (see Rietveld refinement, figure 5.7).

The results of the Rietveld refinement suggest that when a 1:1 molar ratio of the metals impregnated on SiO_2 is reduced in H_2 flow, a clear pattern of the β-NiGa intermetallic nanoparticles is observed, with no observable trace of other crystalline phases. However, as a 5:3 ratio of nitrates is reduced, the resulting diffractogram does not fit to a reference δ-Ni_5Ga_3 pattern (figure 5.5b), although the catalyst prepared in exactly the same way earlier represents a clear δ-Ni_5Ga_3 diffractogram (figure 5.3). The only difference between these two samples is the SiO_2 support: two different SiO_2 batches were used in the two cases. Although in both cases the support was provided by the same company (Saint Gobain), there could be slight differences in the SiO_2 preparation conditions. These variations might result in alternation of the way in which the surface of silica interacts with the metals/oxides/intermediates during reduction. On the other hand, the Ni_5Ga_3 catalysts prepared in the fixed-bed setup using the second SiO_2 batch show a more clear pattern of the δ-Ni_5Ga_3 phase, when investigated with the aid of ex-situ XRD (figure 5.16). Below (figure 7.2) the 3 diffractograms are presented: two of them were recorded after in-situ reduction and subsequent cooling to room temperature, while the third one is measured ex-situ.

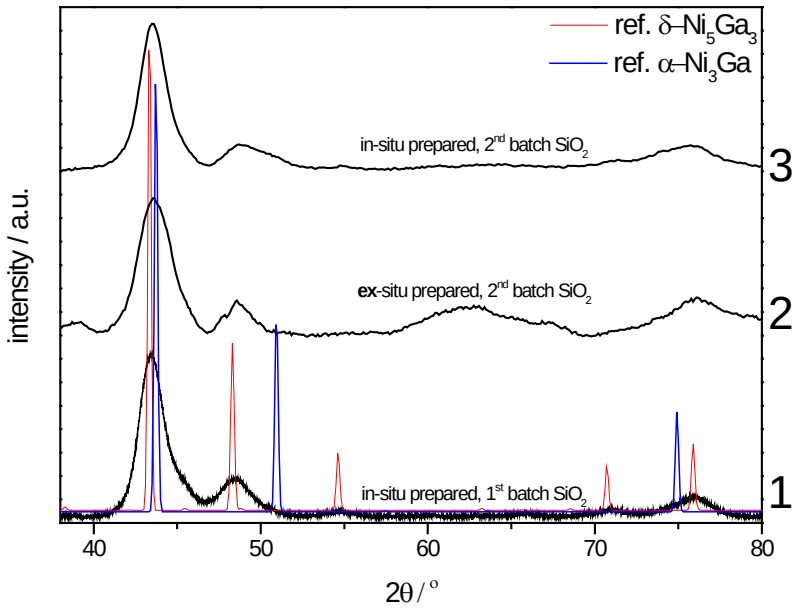

Figure 7.2. Ni_5Ga_3/SiO_2 diffractograms collected at room temperature after TPR.

Batch number	Surface area, m^2/g	Crush strength, kg	Packing density, kg/m^3	Total pore volume, Hg, cc/g	Median pore diameter, Å
1	257	5.6	424.5	1	111
2	241	5.5	420.8	1.04	112

Table 7.1. A table summarizing the characteristics of the two SiO_2 batches.

Comparison of the lower and upper diffractograms shows that in the later case, there is a significant shoulder on the right side of the reflection at $2\theta = 48°$. This shoulder can be attributed to the presence of the α`-Ni_3Ga phase, which was not completely converted to Ni_5Ga_3. The shoulder is, however, not so pronounced in the case of median diffractogram. This could be due to oxidation of the very small Ni_3Ga crystallites when a sample is exposed to air or as a result of passivation in 1% O_2 flow (remember that this was acquired ex-situ).

Another difference between the catalysts prepared from the two SiO_2 batches is the average particle size, which is slightly bigger for the first batch. The difference is reflected both in the XRD- and TEM-derived particle sizes (compare tables 5.1 and 5.5), which can be noticed from the comparison of the main peak broadening (figure 7.2).

In fact, the different SiO_2 supported Ni-Ga intermetallic phases were thoroughly investigated by means of STEM-EELS (scanning transmission electron microscopy – electron energy loss spectroscopy) and EDS (energy dispersive spectroscopy), in a separate project dedicated to quantification of the composition of individual nanoparticles (97). It was shown that, the Ni/Ga ratio of the NiGa and Ni_3Ga nanoparticles always corresponded to the targeted values of 1:1 and 3:1, respectively. However, the Ni_5Ga_3/SiO_2 catalyst was found to contain a certain fraction of Ni_3Ga nanoparticles as well.

What is peculiar is that the catalytic properties are not different between the catalysts represented by the diffractograms No1 and No3: both activity per molar loading of metals and the product distribution (selectivity) are very similar. This could mean that the incomplete alloying is compensated by formation of smaller particles. Another explanation could be that the surface of the Ni_3Ga, when formed together with the Ni_5Ga_3 phase, is different to the intentionally prepared $Ni_3Ga/SiO2$ catalyst. In the later case, the catalysts behavior is similar to that of pure nickel (i.e. methane is the main product), while in the former case the apparent presence of the Ni_3Ga does not worsen the selectivity. This could be explained by the presence of the unalloyed gallium, decorating/blocking the methanation sites. The influence of gallium decorating the surface of Ni_3Ga could either be in killing the activity of these nanoparticles, or in a lucky situation even making them active towards CO_2 hydrogenation. The loss of gallium during reduction can be excluded, as confirmed by the XRF investigations (figure 5.14)

A correlation between the bulk and the surface composition could present itself in a way that the surface is always enriched with nickel. To explain the huge difference in the catalytic behaviour of Ni_5Ga_3/SiO_2 and Ni_3Ga/SiO_2 it could be proposed that for the later catalysts, the surface comprises almost exclusively of nickel, with very minor amount of gallium that is responsible for tuning the catalysts behaviour. For the Ni_5Ga_3 phase, the surface composition is close to Ni_3Ga as calculated by the DFT (modelled Ni_3Ga surface is very close to the top of the volcano as seen in figure 1.1). This idea is supported by the results presented in the figure 5.13: the more Ni-rich phase is synthesised, the larger number of the active (presumably Ni_3Ga) surface sites are formed until a $Ni_{67.5}Ga_{32.5}$ composition is achieved, which is the border of the δ-phases. Beyond the $Ni_{67.5}Ga_{32.5}$ composition, the concentration of pure Ni on the surface is growing very fast, leading to a pure Ni like behaviour at the 75% Ni in the bulk.

Comparison of the two SiO_2 batches does not reveal any significant differences in material properties; therefore the reason behind variations in the crystallographic patterns described above is not completely clear. The absence of certain reflection (for example form [040] plane at $2\theta = 55°$) can be attributed to very small size of the crystal, which makes these reflection look amorphous at the XRD. The later argument is supported by the XRD patterns presented in the figure 5.16: pre-treatment of the catalyst precursor by calcination leads to larger Ni_5Ga_3 crystals formation, with all reflections in the right place.

In-situ x-ray absorption spectroscopy has provided additional insights into the formation of the Ni_5Ga_3/SiO_2 catalysts. Currently, a publication is being prepared (72), where the crystal structure of the catalyst is successfully fit to the reference Ni_5Ga_3. However, mathematical treatment of the EXAFS data does not reveal if other nickel containing species are present after reduction or not.

In terms of deactivation, the Ni-Ga catalysts suffer from loss of activity both under normal working and accelerated ageing conditions. After a 20 hour methanol synthesis test, a catalyst looses approximately 25% of its initial activity. Analysis of how the activity and product distribution changes with time, the results of the experiment involving regeneration and XAS data suggest the following scenario of activity loss:

1. Deactivation through blocking of the active sites with carbon. The later is formed as a result of CO dissociation. Carbon monoxide stems from reverse water gas shift reaction (the "CO_2 – CO – C" route). In this case, the catalyst is presumably modified to a certain degree to form surface nickel carbide, as suggested in (80). Formation of carbon is confirmed by the evolution of methane during the regeneration of the catalyst
2. Deactivation through partial oxidation of the surface and/or segregation of gallium. This is concluded from analysis of the normalized XAS spectra upon exposure of the catalyst to reaction condition: the whiteline at the Ga-edge is increased (figure 6.5)
3. A combination of the two above mentioned scenario

At this stage, it is not completely clear whether methanol synthesis and rWGS reaction are occurring on the similar sites or not. It has been proposed (figure 6.16) that these reaction are

parallel, since the CO/CH_3OH ratio is not constant over time. The continuous drop of the ratio could imply that the rWGS-active sites are deactivated faster than those responsible for methanol synthesis. At the same time, the CO/CH_4 ratio is constant from the beginning, indicating that CO and methane are formed at the same site.

Both CO and CH_4 are undesired products from the point of view of conversion of H_2 into liquid fuels. One could argue that catalytic conversion of CO_2 into CO is an interesting reaction, but this should then be a separate process with a much higher selectivity. From engineering point of view, it would be desirable to block the rWGS pathway without compromising methanol production rate. Provided that the mechanism proposed in the figure 6.16 is adequate, this would simultaneously address the other two problems: methane formation and deactivation by carbon formation. Moreover, thermodynamic analysis shown that the equilibrium methanol production would be then significantly improved, as evident from the figure 7.3.

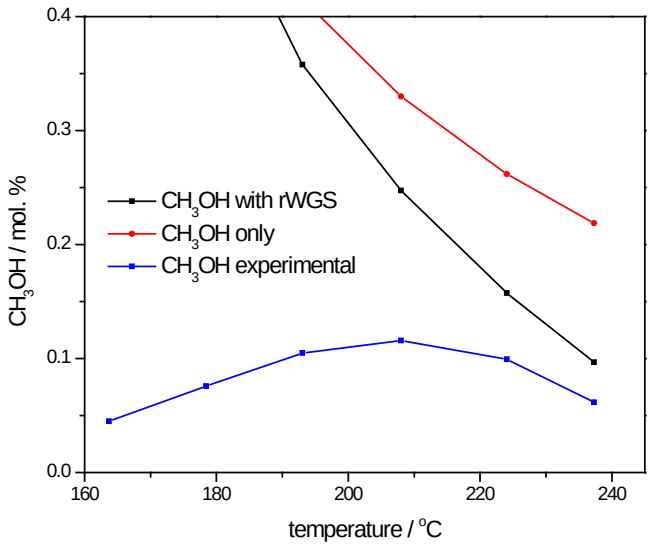

Figure 7.3. Experimental vs equilibrium methanol production, assuming observed and completely suppressed CO concentration.

The CO-free equilibrium conversion is calculated according to the following equation:

$$P(CH3OH) = \sqrt{Pco2 \times (PH2)^3 \times e^{-\frac{\Delta H - T \times \Delta S}{RT}}} \qquad (7.1)$$

which is a way of re-writing the equation 2.10 when methanol is the only reaction product. Figure 7.1 shows that there is indeed a potential for improving the methanol yield if the reverse water gas shift reaction is suppressed. Also note that experimental methanol production curve starts bending already at 200°C, leaving the gap between the equilibrium line. The gap remains even at higher temperatures where the two lines are expected to converge, indicating that the

methanol active sites are poisoned, presumably by carbon monoxide. This is yet another motivation for “killing” the rWGS-active sites.

The later task does not seem to be trivial. But under the assumption that methanol and CO are produced by different surface sites, there should be a chance to preferentially poison one before the other. For example, nickel is known to be sensitive to sulfur (80); if there is a variation in sulfur binding energy of the two nickel-containing sites, then a careful dosing of H_2S might do the job. This is something that will be tried in the nearest future.

Indeed, if the CO and carbon formation could be suppressed, then the Ni-Ga catalyst might be considered even as a higher temperature (and higher pressure) methanol synthesis catalyst. The Ni-Ga nanoparticle do not suffer from sintering or dealloying at the temperatures at least as high as 300°C (see figure 6.3 and 6.7). Copper, on the contrary, loses its surface area irreversibly due to sintering (figure 6.4). The rate of sintering is often correlated with the so-called Tamman temperature, which is approximately half of the materials melting point. For copper, $T_{Tamman} \approx$ 400°C (98). The melting point (and consequently the Tamman temperature) of intermetallic compounds is, in general, higher than those of the individual metals due to high degree of covalency of the metal-metal bond (15). This could be the reason for higher sintering resistance of the Ni-Ga catalysts (remember that these catalysts are prepared at 700°C)

To sum up, it should be confessed that the Ni-Ga catalysts for methanol synthesis cannot be considered for practical applications at this stage. Likewise, they cannot compete with commercially used $Cu/ZnO/Al_2O_3$ catalysts when considerer for high pressure applications. The later one has been optimized for many decades by numerous research groups and companies all around the world, whereas the history of Ni-Ga catalysts for CO_2 hydrogenation has started in December 2010. But given that certain limitations of these intermetallic catalysts are surmounted, they might form a separate class of methanol synthesis catalysts in the future.

8. Bibliography

1. **Masih A.M., Albinali K., DeMello L.** Price dynamics of natural gas and the regional methanol markets. *Energy Policy.* 2010, Vol. 38, 3, pp. 1372-1378.

2. **Chinchen G.C., Denny P.J., Jennings J.R.** Synthesis of methanol - part 1. Catalysis and kinetics. *Applied Catalysis.* 1988, Vol. 36, pp. 1-36.

3. **Apanel G., Johnson E.** Direct methanol fuel cells - ready to go commercial? *Fuel Cells Bulletin.* 2004, Vol. 11, pp. 12-17.

4. **Olah G.A.** Beyond oil and gas. *Ang. Chem Int. Ed.* 2005, Vol. 44, pp. 2636-2639.

5. **Ma J., Sun N., Zhang X.** A short review of catalysts for CO_2 conversion. *Catalysis Today.* 2009, Vol. 148, 3-4, pp. 221-231.

6. **Saito M., Takuechi M., Watanabe T.** Methanol synthesis from CO_2 and H_2 over a Cu/ZnO multicomponent catalyst. *Energy Conversion and Management.* 1997, Vol. 38, pp. 403-408.

7. **Rasmussen P.B., Holmblad P.M., Askgaard T.** Methanol synthesis over Cu (100) from binary reaction mixture of CO_2 and H_2. *Catalysis Letters.* 1994, Vol. 26, pp. 373-381.

8. **Toyir J., Miloua R., Elkadri N.E.** Sustainable process for the production of methanol from CO_2 and H_2 using Cu/ZnO-based multicomponent catalyst. *Physics Procedia.* 2009, Vol. 2, pp. 1075-1079.

9. **Waugh K.C.** Methanol Synthesis. *Catalysis Today.* 1992, Vol. 15, 1, pp. 51-75.

10. **Lormand C..** Industrial Production of Synthetic Methanol. *Ind. Eng. Chem.* 1925, Vol. 17, pp. 430-432.

11. **Spath P.L., Dayton D.C.** *www.nrel.gov/docs/fy04osti/34929.pdf.* [Online] 2003.

12. **Bart J.C.J., Sneeden R.P.A.** Copper - zinc oxide - alumina catalysts revised. *Catalysis Today.* 1987, Vol. 2, pp. 1-124.

13. **Kovnir K., Armbruster M., Teschner D.** A new approach to well-defined, stable and site-isolated catalysts. *Science and Technology of Advanced Materials.* 2007, Vol. 8 , pp. 420–427.

14. **Lambert R.M., Nix R.M.** Methanol synthesis catalysts derived from ternary rare earth, copper, zirconium and rare earth, copper, titanium intermetallic alloys. *Applied Catalysis .* 1990, Vol. 58, 1, pp. 69-81.

15. **Armbruster M., Kovnir K., Grin Y.** Complex metallic phases in catalysis. *Complex metallic alloys.* Weinheim : Willey-VCH, 2001.

16. **Wainright M.S., Trimm D.L.** Methanol synthesis and water-gas shift reactions on raney copper catalysts. *Catalysis Today.* 1995, Vol. 23, 1, pp. 29-42.

17. **Bridgewater A.J., Wainwright M.S., Young D.J.** A comparison of raney copper-zinc and coprecipitated copper-zinc-aluminium oxide methanol syntheses catalysts. *Applied Catalystis.* 1986, Vol. 28, pp. 241-253.

18. **Curry-Hyde H., Sizgek G.D., Wainright M.S.** Improvements to raney copper methanol synthesis catalysts through zinc impregnation - IV. pore structure and the influence on activity. *Applied Catalysis A: General.* 1993, Vol. 95, 1, pp. 65-74.

19. **Lambert R.M., Nix R.M.** Methanol synthesis catalysts from intermetallic precursors: Binary lanthanide-copper catalysts. *Applied Catalysis.* 1987, Vol. 33, 2, pp. 405-430.

20. **Owen G., Shannon M.D.** Intermetallic catalysts for methanol synthesis: Ternary alloys containing copper and cerium. *Applied Catalysis A: Genera.* 1992, Vol. 81, 2, pp. 257-272.

21. **Baglin E.G., Atkinson G.B., Nicks L.J.** Methanol synthesis catalyst from Thorium-Copper intermetallics. Preparation and evaluation. *Ind. Eng. Chem. Prod. Res. Dev.* 1981, Vol. 20, 1, pp. 87-90.

22. **Twigg M.V., Spencer M.S.** Deactivation of supported copper metal catalysts for hudrogenation reactions. *Applied Catalysis A: General.* 2001, Vol. 212, pp. 161–174.

23. **Andersson M.P., Bligaard T., Kustov A.** Toward computational screening in heterogeneous catalysis: Pareto-optimal methanation catalysts. *Journal of Catalysis.* 2006, Vol. 239, pp. 501-506.

24. **Jacobsen C.J.H., Dahl S.** Catalyst Design by Interpolation in the Periodic Table: Bimetallic Ammonia Synthesis Catalysts. *J.Am.Chem.Soc.* 2001, Vol. 123, pp. 8404-8405.

25. **Abild-Pedersen F., Greeley J., Studt F.** Scaling Properties of Adsorption Energies for Hydrogen-Containing Molecules on Transition-Metal Surfaces. *Physical Letters Review.* 2007, Vol. 99, pp. 016105 1-4.

26. **Nørskov J. K., Bligaard T., Logadottir A.** Universality in Heterogeneous Catalysis. *Journal of Catalysis.* 2002, Vol. 209, 2, pp. 275–278.

27. **Studt F., Sharafutdinov I., Abild-Pedersen F.** Novel alloy catalysts for CO_2 hydrogenation to methanol. *article in preparation.* 2012.

28. Standard thermodynamic properties of chemical substances. *http://www.update.uu.se/~jolkkonen/pdf/CRC_TD.pdf.* [Online] 2000.

29. **Holm T.** Aspects of the mechanism of the flame ionization detector. *Journal of Chromatography A.* 1999, Vol. 842, pp. 221-227.

30. **Scanion J.T., De Willis.** Calculation of the flame ionization detector relative response factors utilizing the effective carbon number concept. *Journal of Chromatographic Ccience.* 1985, Vol. 23, 8, pp. 333-340.

31. **Chorkendorff I., Niemantsverdriet J.W.** *Concepts of Modern Catalysis and Kinetics.* Weinheim : WILEY-VCH, 2003.

32. **Gerward L.** *X-Ray Analytical Methods.* Kgs. Lyngby : Technical University of Denmark, 2001.

33. **Rehr J.J., Albers R.C.** Theoretical approaches to x-ray absorption fine structure. *Reviews of Modern Physics.* 2000, Vol. 72, 3, pp. 621-654.

34. **Grunwaldt J-D., Vegten N., Baiker A.** Insight into the structure of supported palladium catalysts during the total oxidation of methane. *Chem. Commun.* 2007, pp. 4635–4637.

35. **Williams D.B., Barry C.C.** *Transmission Electron Microscopy.*: Springer, 2009. Vol. 1.

36. **Okamoto H.** Ga-Ni (Gallium-Nickel). *Journal of Phase Equilibria and Diffusion.* 2008, Vol. 29, 3.

37. **Weatherbee G.D., Bartholomew C.H.** Hydrogenation of CO, on Group VIII Metals. I. Specific Activity of Ni/SiO_2. *Journal of Catalysis.* 1981, Vol. 68, pp. 67-76.

38. **Fujita S., Terunuma H., Nakamura M.** Mechanisms of Methanation of CO and CO_2 over Ni. *Ind. Eng. Chem. Res.* 1991, Vol. 30, pp. 1146-1151.

39. **Peebles D.E., Goodman D.W., White J.M.** Methanation of Carbon Dioxide on Ni(100) and the Effects of Surface Modifiers. *J. Phys. Chem. .* 1983, Vol. 87, pp. 4378-4387.

40. http://icsd.fiz-karlsruhe.de/. [Online]

41. **Pernicone N., Triana F.** Catalyst activation by reduction. *Pure ad Applied Chemisty.* 1978, Vol. 50, pp. 1169—1191.

42. **Bems B., Schur M., Dassenoy A.** Relations between Synthesis and Microstructural Properties of Copper/Zinc Hydroxycarbonates. *Chem. Eur. J.* 2003, Vol. 9, pp. 2039 - 2052.

43. **Louis C., Cheng Z.X., Che M.** Characterization of Ni/SiO_2 Catalysts during Impregnation and Further Thermal Activation Treatment Leading to Metal Particles. *J. Phys. Chem.* 1993, Vol. 97, pp. 5703-5712.

44. **Cavani F., Trifiro F, Vaccari A.** Hydrotalcite-like anionic clays: preparation, properties and applications. *Catalysis Today.* 1991, Vol. 11, pp. 173-301.

45. **Sietsma J., Friedrich H., Broersma A.** How nitric oxide affects the decomposition of supported nickel nitrate to arrive at highly dispersed catalysts. *Journal of Catalysis.* 2008, Vol. 260, pp. 227-235.

46. **Shao L., Zhang W., Armbruster M.** Nanosizing Intermetallic Compounds Onto Carbon Nanotubes: Active and Selective Hydrogenation Catalysts. *Angew. Chem. Int. Ed.* 2011, Vol. 50, pp. 10231 –10235.

47. **Ji X., Lee K.T., Holden R.** Nanocrystalline intermetallics on mesoporous carbon for direct formic acid fuel cell anodes. *Nature Chemistry.* 2010, Vol. 2, pp. 286-293.

48. **Bauer J.C., Chen X., Liu Q.** Converting nanocrystalline metals into alloys and intermetallic compounds for applications in catalysis. *Journal of Material Chemistry.* 2008, Vol. 18, 3.

49. **Gasteiger H.A., Kocha S.S., Sompalli B.** Activity benchmarks and requirements for Pt, Pt-alloy, and non-Pt oxygen reduction catalysts for PEMFCs. *Applied Catalysis B: Environmental.* 2005, Vol. 56, pp. 9–35.

50. **Greeley J., Stephens I. E. L., Bondarenko A. S.** Alloys of platinum and early transition metals as oxygen reduction electrocatalysts. *Nature Chemistry.* 2009, Vol. 1, pp. 552-556.

51. **Thanh C. N., Didillon B., Sarrazin P.** *U.S. patent. 6,054,409* 2000.

52. **Jin Y., Datye A.K., Rightor E.** The Influence of Catalyst Restructuring on the Selective Hydrogenation of Acetylene to Ethylene. *Journal of Catalysis.* 2001, Vol. 203, pp. 292-306.

53. **Mei D., Neurock M., Smith C.M.** Hydrogenation of acetylene–ethylene mixtures over Pd and Pd–Ag alloys: First-principles-based kinetic Monte Carlo simulations. *Journal of Catalysis.* 2009, Vol. 268, pp. 181–195.

54. **Armbruster M., Kovnir K., Behrens M.** Pd-Ga Intermetallic Compounds as Highly Selective Semihydrogenation Catalysts. *JACS.* 2010, Vol. 132, pp. 14745–14747.

55. **Armbrüster M., Borrmann H., Wedel M.** Refinement of the crystal structure of palladium gallium (1:1), PdGa. *Z. Kristallogr.* 2010, Vol. 225, pp. 617-618.

56. **Armbrüster M., Kovnir K., Friedrich M.** Al13Fe4 as a low-cost alternative for palladium in heterogeneous hydrogenation. *Nature Materials.* 2012, Vol. 11, pp. 690-693.

57. **Park S., Xie Y., Weaver M.J.** Electrocatalytic Pathways on Carbon-Supported Platinum Nanoparticles: Comparison of Particle-Size-Dependent Rates of Methanol, Formic Acid, and Formaldehyde Electrooxidation. *Langmuir.* 2002, Vol. 18, pp. 5792-5798.

58. **Friedrich M., Teschner D., Knop-Gericke A.** Influence of bulk composition of the intermetallic compound ZnPd on surface composition and methanol steam reforming properties. *Journal of Catalysis.* 2012, Vol. 285, 1, pp. 41–47.

59. **Kovnir K., Osswald J., Armbraster M.** *PdGa and Pd_3Ga_7: Highly-Selective Catalysts for the Acetylene Partial Hydrogenation.* Louvain-la-Neuve : s.n., 2006. International symposium on the scientific bases for the preparation of heterogeneous catalysts. Vol. 162, pp. 481-488.

60. **Sachtler W.M.H.** Chemisorption Complexes on Alloy Surfaces. *Catal. Rev. Sci. Eng.* 1976, Vol. 14, 2, pp. 193-210.

61. **Ruban A., Hammer B., Stoltze P.** Surface electronic structure and reactivity of transition and noble metals. *Journal of Molecular Catalysis A: Chemical.* 1997, Vol. 115, pp. 421–429.

62. **Baltes C., Vukojevic S., Schüth F.** Correlations between synthesis, precursor, and catalyst structure and activity of a large set of $CuO/ZnO/Al_2O_3$ catalysts for methanol synthesis. *Journal of Catalysis.* 2008, Vol. 258, pp. 334–344.

63. **Bergeret G., Gallezot P.** Particle Size and Dispersion Measurements. *Handbook of Heterogeneous Catalysis.* s.l. : Wiley-VCH, 2008, pp. 738-765.

64. **Dean J.A.** *Langes Handbook of Chemistry.* 15th edition. s.l. : R. R. Donnelley & Sons, 1999.

65. **Duchstein, Linus Daniel Leonhard.** *PhD thesis. Environmental Transmission Electron Microscopy of catalysts for the methanol synthesis.* Center for Electron Nanoscopy, Technical University of Denmark : s.n., 2012.

66. http://www.ccp14.ac.uk/tutorial/lhpm-rietica/doc/manual.pdf. [Online]

67. **Ducher R., Kainuma R., Ishida K.** Phase equilibria in the Ni-rich portion of the NiGa binary system. *Intermetallics.* 2007, Vol. 15 , pp. 148-153.

68. **Yuan W.X., Qiao Z.Y., Ipser H.** Journal of Phase Equilibria and Diffusion. *Journal of Phase Equilibria and Diffusion.* 2004, Vol. 25, 1, pp. 68-74.

69. **Martosudirjo S., Pratt J.N.** Enthalpies of formation of solid nickel-gallium and nickel-germanuim alloys. *Thermochimia Acta.* 1976, Vol. 17, pp. 183-194.

70. **Ravel B., Newville M.** ATHENA, ARTEMIS, HEPHAESTUS: data analysis for X-ray absorption spectroscopy using IFEFFIT. *Journal of Synchrotron Radiation.* 2005, Vol. 12, pp. 537–541.

71. htpp://hyperphysics.phy-astr.gsu.edu/ hbase/tables/kxray.html. [Online]

72. **Sharafutdinov I., Elkjaer C., Hudson W.** Investigations into synthesis and optimization of supported intermetallic Ni-Ga catalysts using a combination of complementary characterization tools. *article in preparation.* 2013.

73. **Armbruster M., Wowsnick G., Friedrich M.** Synthesis and Catalytic Properties of Nanoparticulate Intermetallic Pd-Ga compounds. *J. Am. Chem. Soc.* 2011, Vol. 133, pp. 9112–9118.

74. **Chakraborty D., Kulkarni P.P., Kovalchuk V.** Dehalogenative oligomerization of dichlorodifluoromethane catalyzed by activated carbon-supported Pt–Cu catalysts: effect of Cu to Pt atomic ratio. *Catalysis Today.* 2004, Vol. 88, 3, pp. 169-181.

75. **Yamamoto Y., Nawa N., Nishimoto S.** Temperature dependence of hydrogen adsorption properties of nickel-doped mesoporous silica. *International Journal of Hydrogen Energy .* 2011, Vol. 36, pp. 5739-5743.

76. **Brockner W., Ehrhardt C., Gjikaj M.** Thermal decomposition of nickel nitrate hexahydrate, $Ni(NO_3)_2{\cdot}6H_2O$, in comparison to $Co(NO_3)_2{\cdot}6H_2O$ and $Ca(NO_3)_2{\cdot}4H_2O$. *Thermochimica Acta.* 2007, Vol. 456, pp. 64–68.

77. **Berbenni V., Milanese C., Bruni G.** Thermal decomposition of gallium nitrate hydrate $Ga(NO_3)_3*xH_2O$. *Journal of Thermal Analysis and Calorimetry.* 2005, Vol. 82, pp. 401–407.

78. **Bhan S., Schubert K.** Uber die struktur von phasen mit kupper unterstruktur in einigen T-B legierungen (T= Ni, Pd, Pt; B=Ga, In, Tl, Pb, Sb, Bi). *Journal of the Less-Common Metals.* Uber die struktur von phasen mit kupper unterstruktur in einigen T-B legierungen, 1968, Vol. 17, pp. 73-90.

79. **Toupance T., Kermarec M., Louis C.** Metal Particle Size in Silica-Supported Copper Catalysts. Influence of the Conditions of Preparation and of Thermal Pretreatments. *J. Phys. Chem. B.* 2000, Vol. 104, pp. 965-972.

80. **Bartholomew, C.H.** Mechanisms of catalyst deactivation. *Applied Catalysis A: General.* 2001, Vol. 212, pp. 17–60.

81. **Lakhapatri S.L., Abraham M.A.** Deactivation due to sulfur poisoning and carbon deposition on Rh-Ni/Al_2O_3 catalyst during steam reforming of sulfur-doped n-hexadecane. *Applied Catalysis A: General.* 2009, Vol. 364, pp. 113–121.

82. **Seoane X.L., L'Argentiere P.C., Figoli N.S.** On the deactivation of supported palladium hydrogenation catalysts by thiophene poisoning. *Catalysis Letters.* 1992, Vol. 16, pp. 137-148.

83. **Bartholomew C.H., Bowman R.M.** Sulfur poisoning of cobalt and iron Fischer-Tropsch catalysts. *Applied Catysis, 15.* 1985, Vol. 15, pp. 59-67.

84. **Bartholomew C.H., Agrawal P.K., Katzer J.R.** Sulfur poisoning of metals. *Advances in Catalysis.* 1982, Vol. 31, pp. 135-242.

85. **Hensen E.J.M, De Beer V.H.J., Van Veen J.A.R.** On the sulfur tolerance of supported Ni(Co)Mo sulfide hydrotreating catalysts. *Journal of Catalysis.* 2003, Vol. 215, pp. 353-357.

86. **Friedrich M., Teschner D., Knop-Gericke A.** Surface and Subsurface Dynamics of the Intermetallic Compound ZnNi in Methanol Steam Reforming. *Journal of Physical Chemistry.* 2012, Vol. 116, 28, pp. 14930-14935.

87. **Haghofer A., Föttinger K., Girgsdies F.** In situ study of the formation and stability of supported Pd_2Ga methanol steam reforming catalysts. *Journal of Catalysis.* 2012, Vol. 286, pp. 13–21.

88. **Ota A., Kunkes E.L., Kasatkin I.** Comparative study of hydrotalcite-derived supported Pd_2Ga and PdZn intermetallic nanoparticles as methanol synthesis and methanol steam reforming catalysts. *Journal of Catalysis.* 2012, Vol. 293, pp. 27–38.

89. kau.edu.sa/Files/0001216/files/4356 _Problems%20and%20Chalenges.pdf. [Online]

90. **Kurtz M., Wilmer H., Genger T.** Deactivation of supported copper catalysts for methanol synthesis. *Catalysis Letters.* 2003, Vol. 86, pp. 77-80.

91. **Jinhua H., Jixiang C.** Comparison of Ni2P/SiO2 and Ni/SiO2 for Hydrogenolysis of Glycerol: A Consideration of Factors Influencing Catalyst Activity and Product Selectivity. *Chinese journal of Catalysis.* 2012, Vol. 33, 5.

92. **Lindberg R., Sjoblom J., Sundholm G.** Preparation of silica particles utilizing the sol-gel and the emulsion-gel processes. *Colloids and Surfaces A: Physicochem. Eng. Aspects.* 1995, Vol. 99, pp. 79-88.

93. **Nørskov J.K., Abild-Pedersen F., Studt F.** Density functional theory in surface chemistry and catalysis. *PNAS.* 2011, Vol. 108, 3, pp. 937–943.

94. **Nørskov J. K., Bligaard T., Rossmeisl J.** Towards the computational design of solid catalysts. *Nature Chemistry.* 2009, Vol. 1, pp. 37-46.

95. **Honkala K., A. Hellman A., Remediakis I. N.** Ammonia Synthesis from First-Principles Calculations. *Science.* 2005, Vol. 307, pp. 555-558.

96. **Collins S.E., Baltanas M.A., Fierro J.L.** Gallium–Hydrogen Bond Formation on Gallium and Gallium–Palladium Silica-Supported Catalysts. *Journal of Catalysis.* 2002, Vol. 211, pp. 252–264.

97. **Gardini D.** Electron based spectrocopy and imaging of nanoparticels. *Master Thesis.* Center for Electron Nanoscopy, Technical University of Demnark, 2012.

98. **Moulijn J.A., Van Diepen A.E., Kapteijn F.** Catalyst deactivation: is it predictable? What to do? *Applied Catalysis A: General.* 2001, Vol. 212, pp. 3-16.